ADAPTIVE MIMO FREE SPACE OPTICAL COMMUNICATION SYSTEMS

A Dissertation

by

Hatef Nouri

Submitted to the
Graduate School of Sciences and Engineering
In Partial Fulfillment of the Requirements for
the Degree of

Doctor of Philosophy

in the
Department of Electrical and Electronics Engineering

Özyeğin University
May 2022

ADAPTIVE MIMO FREE SPACE OPTICAL COMMUNICATION SYSTEMS

Professor Murat Uysal, Advisor
Department of Electrical and Electronics Engineering
Özyeğin University

Associate Professor Tunçer Baykaş
Faculty of Engineering and Natural Sciences
Kadir Has University

Associate Professor Cenk Demiroğlu
Department of Electrical and Electronics Engineering
Özyeğin University

Associate Professor Tansal Güçlüoğlu
Department of Electronics And Communication Engineering
Yildiz Technical University

Date Approved: 12 May 2022

Assistant Professor Kadir Durak
Department of Electrical and Electronics Engineering
Özyeğin University

To my dear parents

ABSTRACT

Free space optical (FSO) enjoys the high data rate of optical spectrum and have also the flexibility of RF links. FSO systems provide many advantages to the line of sight wireless communication technology. With the recent increasing interest on this promising technology, there is a need for a comprehensive understanding of system limitations which is mainly due to atmospheric conditions.

In the first part of this research, we use our custom design atmospheric channel emulator for FSO system evaluations in a controlled environment and experimentally investigate the performance of FSO links. Specifically, we investigate the geometric loss, absorption loss, different weather conditions (like foggy and rainy), different beam shapes, and atmospheric turbulence using the atmospheric chamber. Atmospheric turbulence is a significant impairment in FSO channels which results in random fluctuations in the received signal level. By generating a desired level of atmospheric turbulence in the chamber, we investigate effect of wavelength and aperture averaging on the performance of FSO systems. Aperture averaging extracts inherent receive diversity gains and can be used as an effective fading mitigation technique.

Furthermore, multiple apertures systems are also adopted in practical FSO systems to mitigate the turbulence induced fading effects and offer dramatic performance improvements in terms of link reliability (via diversity gain) and data rates (via multiplexing gain). On the other hand, the turbulence induced fading is characterized as very slow-varying, hence reliable feedback would be possible and adaptive transmission can be implemented in practical FSO systems and brings a noticeable performance improvement. Although the literature for adaptive transmission of RF systems is mature, it has been recently applied to SISO FSO systems and its direct application to MIMO FSO systems is challenging. Aiming to

fill research gaps in this growing field, this work develops a framework for practical FSO systems with adaptive MIMO architectures. A MIMO system over a frequency-flat, log-normal or Gamma-Gamma slow-fading channel is considered in our work. In MIMO FSO systems, the space-time transmission strategy can also be adjusted, introducing a new dimension for adaptation. This means that practical MIMO link adaptation algorithms must also provide a dynamic adaptation between diversity and multiplexing modes of operation which needs a fundamental understanding of diversity-multiplexing tradeoff (DMT) under log-normal fading channels. Although there has been a growing interest on the study of DMT, the existing works are mostly restricted to the outcomes reported for Rayleigh, Rician, and Nakagami fading channels. In the next part of this research, we investigate the optimal tradeoff in the presence of log-normal fading channels. We derive the outage probability expression, and then present the asymptotical DMT expression. We further investigate DMT for finite SNRs and demonstrate convergence to the asymptotical case.

Next, we suggest a framework for practical MIMO FSO system with adaptive architectures and shows how to use this framework to increase either link reliability (via diversity gain) and or data rates (via multiplexing gain). To illustrate our approach, we consider three MIMO transmission mapping matrices which includes: Matrix A (multiplexing), employing only spatial multiplexing; Matrix B (diversity), exploiting only diversity; and Matrix C (hybrid), combining diversity and spatial multiplexing. We first obtain expressions for the outage capacity of these matrices as the metric to maximize the rate of system for a fix target outage probability. Limiting the adaptation modes to a small subset is the key of adaptive strategy. The spatial adaptation can be combined with conventional adaptive modulation and coding (AMC) to give the optimal system performance.

Particularly, we consider multiple-input single-output (MISO) and single-input multiple-output (SIMO) FSO systems with pulse position modulation (PPM) and pulse amplitude modulation (PAM). We propose three adaptive algorithms where the modulation size and/or transmit power are adjusted according to the channel conditions. We formulate the design of adaptive algorithms to maximize the spectral efficiency under peak and average power constraints while maintaining a targeted value of outage probability.

In conclusion, this work propose a promising progress to overcome the main impairments (fog attenuations and turbulence induced fading) of the FSO links in four ways: 1) by examining the channel and proposing novel models and characteristics for atmospheric attenuations 2) by taking advantage of aperture averaging and wavelength dependency trade-off 3) by investigating and proposing spatial adaptation in MIMO FSO links and 4) by employing adaptive modulation and power control scenarios and approving the promising performance of adaptive system.

ÖZETÇE

Serbest uzay optik haberleşme (FSO), optik spektrumun yüksek veri hızından yararlanır ve ayrıca RF bağlantılarının esnekliğine sahiptir. FSO sistemleri, görüş hattı kablosuz iletişim teknolojisine birçok avantaj sağlar. Bu vaat eden teknolojiye son zamanlarda artan ilgi ile birlikte, esas olarak atmosferik koşullardan kaynaklanan sistem sınırlamalarının kapsamlı bir şekilde anlaşılmasına ihtiyaç duyulmaktadır.

Bu araştırmanın ilk bölümünde, kontrollü bir ortamda FSO sistem değerlendirmeleri için özel tasarım atmosferik kanal emülatörümüzü kullanıyoruz ve FSO bağlantılarının performansını deneysel olarak araştırıyoruz. Spesifik olarak, atmosferik kanal emülatörünü kullanarak geometrik kaybı, absorpsiyon kaybını, farklı hava koşullarını (sisli ve yağmurlu gibi), farklı ışın şekillerini ve atmosferik türbülan- sı araştırıyoruz. Atmosferik türbülans, alınan sinyal seviyesinde rastgele dalgalanmalara neden olan FSO kanallarında önemli bir bozulmadır. emülatörda istenen seviyede atmosferik türbülans üreterek, dalga boyu ve delik ortalamasının FSO sistemlerinin performansı üzerindeki etkisini araştırıyoruz. delik ortalama özütleri, doğal olarak çeşitlilik kazanımlarını alır ve etkili bir sönümleme azaltma tekniği olarak kullanılabilir.

Ayrıca, türbülansın neden olduğu sönümleme etkilerini azaltmak ve bağlantı güvenilirliği (çeşitlilik kazancı yoluyla) ve veri hızları (çoklama kazancı aracılığıyla) açısından çarpıcı performans iyileştirmeleri sunmak için pratik FSO sistemlerinde çoklu delik sistemleri de benimsenmiştir. Öte yandan, türbülans kaynaklı sönümleme çok yavaş değişen olarak karakterize edilir, bu nedenle güvenilir geri besleme mümkün olur ve pratik FSO sistemlerinde uyarlamalı iletim uygulanabilir ve önemli bir performans artışı sağlar. RF sistemlerinin uyarlanabilir iletimi için

literatür olgun olmasına rağmen, son zamanlarda SISO FSO sistemlerine uygulanmıştır ve MIMO FSO sistemlerine doğrudan uygulanması zordur. Bu büyüyen alandaki araştırma boşluklarını doldurmayı amaçlayan bu çalışma, uyarlanabilir MIMO mimarileri ile pratik FSO sistemleri için bir çerçeve geliştiriyor. Çalışmamızda düz frekansli, log-normal veya Gamma-Gama yavaş sönümlü bir kanal üzerinde bir MIMO sistemi ele alınmıştır. MIMO FSO sistemlerinde, mekan-zaman iletim stratejisi de ayarlanabilir, bu da adaptasyon için yeni bir boyut sunar. Bu, pratik MIMO bağlantı uyarlama algoritmalarının, çeşitlilik ve çoğullama çalışma modları arasında dinamik bir uyarlama sağlaması gerektiği anlamına gelir. Bu, log-normal sönümleme kanalları altında temel bir çeşitlilik-çoğullama dengeleme (DMT) anlayışına ihtiyaç duyar. DMT çalışmasına artan bir ilgi olmasına rağmen, mevcut çalışmalar çoğunlukla Rayleigh, Rician ve Nakagami sönümleme kanalları için bildirilen sonuçlarla sınırlıdır. Bu araştırmanın bir sonraki bölümünde, log-normal sönümlü kanalların varlığında optimal dengeyi araştırıyoruz. Kesinti olasılığı ifadesini türetiyoruz ve ardından asimptotik DMT ifadesini sunuyoruz. Sonlu SNR'ler için DMT'yi daha da araştırıyoruz ve asimptotik duruma yakınsama gösteriyoruz.

Daha sonra, uyarlanabilir mimarilere sahip pratik MIMO FSO sistemi için bir çerçeve öneriyoruz ve bu çerçevenin bağlantı güvenilirliğini (çeşitlilik kazancı yoluyla) ve veya veri hızlarını (çoklama kazancı aracılığıyla) artırmak için nasıl kullanılacağını gösteriyoruz. Yaklaşımımızı göstermek için, aşağıdakileri içeren üç MIMO iletim eşleme matrisini ele alıyoruz: Matris A (çoğullama), Yalnızca mekansal çoğullamayı kullanan ; Matris B (çeşitlilik), yalnızca çeşitlilikten yararlanan; ve Matris C (hibrit), çeşitlilik ve mekansal çoğullamayı birleştiren. İlk önce, sabit bir kesinti olasılığı için sistemin oranını en üst düzeye çıkarmak için metrik olarak bu matrislerin kesinti kapasitesi için ifadeler elde ederiz.Uyarlama modlarını küçük bir alt kümeyle sınırlamak, uyarlanabilir stratejinin anahtarıdır. mekansal uyarlama, en uygun sistem performansını vermek için geleneksel uyarlamalı modülasyon ve kodlama (AMC) ile birleştirilebilir.

Özellikle, darbe konum modülasyonu (PPM) ve darbe genlik modülasyonu (PAM) ile çok girişli tek çıkışlı (MISO) ve tek girişli çok çıkışlı (SIMO) FSO sistemlerini düşünüyoruz. Modülasyon boyutunun ve/veya iletim gücünün kanal koşullarına göre ayarlandığı üç uyarlamalı algoritma öneriyoruz. Hedeflenen bir kesinti olasılığı değerini korurken, üst ve ortalama güç kısıtlamaları altında spektral verimliliği en üst düzeye çıkarmak için uyarlanabilir algoritmaların tasarımını formüle ediyoruz.

Sonuç olarak, bu çalışma, FSO bağlantılarının ana bozukluklarının (sis zayıflamaları ve türbülansın neden olduğu zayıflama) dört şekilde üstesinden gelmek için vaat eden bir ilerleme önermektedir: 1) kanalı inceleyerek ve atmosferik zayıflamalar için yeni modeller ve özellikler önererek, 2) delik ortalamasından ve dalga boyu bağımlılığı değiş tokuşundan yararlanarak, 3) MIMO FSO bağlantılarında mekansal uyarlamayı araştırarak ve önererek, ve 4) Uyarlanabilir modülasyon ve güç kontrol senaryolarını kullanarak ve uyarlanabilir sistemin gelecek vaat eden performansını onaylayarak.

ACKNOWLEDGEMENTS

I would like to express my special appreciation and thanks to my supervisor, Professor Murat Uysal, for his excellent guidance and motivations. This thesis would have not been possible without his consistence support throughout the course of my Ph.D. studies. I would like to express my gratitude, for being such a great man and source of constant support. Just recently, I noticed how self-confident I feel myself, for having this opportunity with you, and listening to you speaking wisely with vast amount of knowledge and understanding. I admire your complete dedication to your research. I hope, I am able to take some of that drive and commitment to excellence with me in my future endeavors.

I would like to express my appreciation to the members of my dissertation committee, Professors Kadir Durak, Tunçer Baykaş, Cenk Demiroğlu, and Tansal Güçlüoğlu for taking the time to carefully monitor my progress and read my thesis. Definitely, the guidance and support you have given me throughout my studies and this dissertation would be a treasure for the rest of my life.

This work was supported by the Turkish Scientific and Research Council (TUBITAK) under grant no. 215E311.

TABLE OF CONTENTS

LIST OF TABLES

LIST OF FIGURES

CHAPTER I

INTRODUCTION

Free space optical (FSO) communication systems have initially attracted attention as an efficient solution for the "last mile" problem to bridge the gap between the end user and the fiber optic infrastructure already in place. In recent years, there has been a growing interest on FSO systems with a well-established literature, see [1, 2] and the references therein. FSO communication systems provide point-to-point wireless connectivity via the use of infrared laser transmitters. Over their radio frequency (RF) counterparts, these systems bring several advantages such as high bandwidth capacity in unlicensed spectrum, robustness to electromagnetic interference, and inherent security among others [1, 3]. FSO communication systems can be used in a wide range of application areas including enterprise/campus connectivity, fiber back-up, backhauling for cellular networks, and airborne communications among others [3]. These systems offer a large bandwidth in unregulated spectrum. As a cost-effective and high-speed wireless solution, they can be deployed for a variety of applications such as cellular backhaul/fronthaul, temporary links for disaster recovery and emergency response, wireless video surveillance and monitoring, high definition television (HDTV) transmission, quantum key distribution among others [3].

1.1 FSO Channel Modeling

With the recent increasing interest on this promising technology, there is a need for a comprehensive understanding of system limitations in practical propagation settings. Optical signal propagation in free space is affected by geometric loss, atmospheric attenuation, turbulence, and pointing errors, which fade the signal at the receiver and deteriorate the link performance [1,4]. Atmospheric attenuation of FSO links is dependent on weather conditions such as fog, rain, dust, and various combinations of each. Furthermore, FSO links experience atmospheric turbulence induced fading as a result of the variations in the refractive index.

Due to the difficulty to predict the occurrence of specific atmospheric effects and to repeat the measurements under the same conditions, it is highly desirable to evaluate the FSO system performance in a controlled laboratory environment. Along this direction, several works have been recently reported in the literature [5–12] where various environmental effects (turbulence, fog, smoke, dust, ash, and sand) are investigated in custom design atmospheric chambers. Particularly, the effect of foggy weather conditions is studied in [10–12] based on measurements in an atmospheric chamber. The degrading effect of fog on the bit error rate (BER) performance of the FSO link is quantified in [10]. In [12], a wavelength-dependent model is proposed for fog and smoke channels valid within the visibility ranges of less than 1 km.

In Chapter 2, we present our own custom design atmospheric channel emulator for FSO system evaluations and experimentally investigate the performance of FSO links in fog conditions. First, we present a link budget and quantify the geometrical loss. Then we discuss atmospheric loss and its characterization. Next, we emulate foggy weather conditions inside the chamber and quantify the absorption loss for different wavelengths. Based on the experimental data, we also propose a new and accurate model for the prediction of fog attenuation coefficient.

A major performance impairment in FSO systems particularly for long link ranges is turbulence-induced fading as a result of the variations in the refractive index [1]. Log-normal (LN) and Gamma-Gamma (GG) statistical distributions are widely used to characterize weak and moderate/strong turbulence conditions, respectively [4]. The most common fading mitigation technique in the context of FSO systems is aperture averaging [4]. Based on the fact that the size of receive aperture is much larger than operation wavelength, this technique extracts inherent receive diversity gains.

In early experimental works [13–16], aperture averaging factor (AAF), defined as the ratio of scintillation index for a fixed aperture size to that of a point aperture, was commonly used as a simple performance metric to quantify the performance improvements. In [17–19], the effect of aperture averaging on the turbulence statistics was further studied. Specifically, in [17, 18], measurements were taken for a link length of 1500 m at three receivers with diameters 1, 5, and 13 mm. It was observed that GG probability density function (PDF) provided a good fit to the data collected by small size aperture. For larger apertures, due to the aperture averaging, LN PDF provided a better fit despite the moderate/strong turbulence conditions. Another similar experiment was conducted in [19] which compare LN and GG model for different aperture diameters of 1.5, 4, 7, 10, 20.6, 154 mm over a link distance of 1 km with a 532 nm solid-state laser. Similar conclusions as in [17,18] were reported. A summary of existing experimental works can be found in Table 1.

Table 1: Experimental Studies on Aperture Averaging

	Wavelength	**Link**	**Aperture Size**	**Metric**
[13]	633 nm	1 km	1, 2.25, 5, 10, 25, 50 mm	AAF
[14]	633 nm	863 m	Variable from 1 to 14 cm	AAF
[15]	780 μm CW	1.2 km	Pinhole, interchangeable	AAF
[16]	633 nm	50 cm	Variable from 1 to 6 mm	AAF
[17]	1550 nm	1 km	1, 5, 13 mm	PDF
[18]	1550 nm	1 km	1, 5, 13 mm	PDF
[19]	532 nm CW	1 km	1.5,4, 10, 20.6, 154 mm	PDF

In the last part of Chapter 2, we focus on three most common wavelengths used in telecommunications, namely 850 nm, 1310 nm, and 1550 nm and present a comparative performance evaluation of aperture averaging under the same emulated atmospheric conditions. The main motivation of our work is to investigate the trade-off between wavelength and aperture size in the context of aperture averaging. Our emulator is in the form of an atmospheric chamber equipped with adjustable heaters, coolers and fans to create the desired level of turbulence. Employing this atmospheric chamber, we conduct experiments over a link distance of

3 m. Plano convex lens is used to expand the laser beam to mimic the condition of outdoor transmission. At the receiver side, three aperture diameters of 1, 3.6, 8.7 mm are employed. For each of the wavelengths under consideration, received powers are recorded at high sampling rates to characterize the turbulence induced fluctuations. Based on these samples, the PDF of atmospheric turbulence channel fading coefficients are determined and compared for wavelengths of 850 nm, 1310 nm, and 1550 nm.

1.2 DMT Analysis under Log-normal Fading Channel

After characterizing the atmospheric dependency of FSO links, in Chapter 2, we dive into mitigation techniques for the major performance impairment of FSO links, i.e. turbulence induced fading. Generally speaking, multipath induced fading is a significant impairment in wireless channels which results in random fluctuations in the received signal level. Multiple-input multiple-output (MIMO) communication techniques are widely employed in major wireless standards to mitigate the fading effects and offer dramatic performance improvements in terms of link reliability (via diversity gain) and data rates (via multiplexing gain) [20–22]. However, reaping the dual benefits of MIMO systems needs some caution because maximizing one of the gains does not necessarily maximize the other one. In fact, it has been shown by Zheng and Tse [23] that there is a fundamental tradeoff between multiplexing and diversity gains. Under the assumption of high signal-to-noise ratios (SNRs), they obtain the asymptotical maximum achievable diversity gain for each multiplexing gain under the assumption of Rayleigh fading channels. In [24], Narasimhan extends it to a non-asymptotic framework and analyzes the tradeoff between diversity and multiplexing gains of a MIMO system at finite SNRs. These works have triggered other research efforts to obtain the optimal diversity-multiplexing tradeoff (DMT) for various channel and system models [25–33].

Despite the rich literature on DMT, existing works are mostly restricted to the outcomes reported for Rayleigh, Rician, and Nakagami fading channels. These models are found to be a better fit for outdoor wireless channels, on the other hand log-normal fading provides an accurate model for indoor radio propagation environments [34–36] and terrestrial optical wireless channels [37–39].

Existing works on log-normal fading channels: The existing works on log-normal fading channels mainly address either the channel capacity [40–44] or diversity gain [45–48]. Since a closed exact expression for the ergodic capacity of log-normal fading channels is mathematically intractable, [40] provides a tight approximation for the capacity of a single-input single-output (SISO) log-normal channel. Laourine et. al. in [41, 42] investigate the capacity of single-input multi-output (SIMO) system with Maximum Ratio Combining (MRC) and Equal Gain Combining (EGC) over log-normal fading channels. The work in [43] considers a correlated log-normal fading model and investigates the effect of correlation on the capacity. In [44], the capacity analysis for different adaptive transmission schemes is studied.

Error rate performance of SIMO systems over log-normal fading channels is presented in [45–48]. In [45], the average bit error probability of diversity combining with two correlated log-normal fading branches is presented and the effect of correlation is investigated. In [46], the distribution of the sum of independent and identically distributed (i.i.d.) lognormal random variables is approximated by an Erlang distribution and the diversity gain over correlated and uncorrelated lognormal fading channels is derived. In [47], a SIMO system with two antennas at the receiver is considered and the outage probability is derived for MRC, selection combining (SC), and switch-and-stay combining schemes. In [48], the outage probability of SC is derived for more than two antennas.

In [49], Safari et. al., study the diversity gain of cooperative communication systems over log-normal fading channels. They derive pairwise error probability and also quantify the advantages of diversity by defining the asymptotical relative diversity order (ARDO). Furthermore, [50,51] analyze the performance of amplify-and-forward multi-branch multi-hop wireless relay systems with MRC and SC schemes and investigate the diversity gains through the derivation of ARDO.

As summarized above, there has been a growing literature on the performance analysis of wireless systems over log-normal fading channels. However, there have been no previous results reported on the DMT analysis to the best of our knowledge. Aiming to fill this research gap, we analyze the DMT of MIMO systems over log-normal fading channels. We first derive the outage probability expressions and then derive asymptotical DMT (i.e., when SNR goes to infinity) and finite-SNR DMT expressions. It is observed that the asymptotical DMT shows quadratic behavior with infinite value at multiplexing gain $r = 0$, whereas, it shows common piecewise linear behavior as $(M - r)(N - r)$ for $r > 1$ where M and N denote respectively transmit and receive antennas. Through normalization with respect to SISO case, we obtain the *relative* asymptotical DMT and show that it is described by $MN(1 - r)^2$ for $0 \leq r \leq 1$. Furthermore, we investigate the outage formulation and DMT behavior at finite-SNRs. Our results demonstrate that as SNR increases and tends toward infinity, the finite-SNR DMT curve shifts up and finally converges to the asymptotical curve. Our results further point out that employing MIMO system in log-normal channels can be more beneficial when the fading is weaker.

1.3 Adaptive MIMO FSO System

The understanding of DMT under log-normal fading channels will allow us to investigate practical MIMO link adaptation algorithms for FSO links which provide a dynamic adaptation between diversity and multiplexing modes of operation. The turbulence induced fading is characterized as very slow-varying, hence reliable feedback would be possible and adaptive transmission can be implemented in practical FSO systems and brings a noticeable performance improvement. In chapter 4 and 5, we develop a framework for practical FSO systems with adaptive MIMO architectures. A MIMO system over a frequency-flat, log-normal or Gamma-Gamma slow-fading channel is considered in our work. In MIMO FSO systems, the space-time transmission strategy can also be adjusted, introducing a new dimension for adaptation. In the existing literature [1,2], typically open-loop system designs are investigated where the channel state information (CSI) is only available at the receiver. If CSI is available at the transmitter side via a proper feedback channel, this information can be used to adjust transmission parameters according to channel conditions. Such closed-loop systems might not be preferable for time-varying channels as the implementation of feedback channel is challenging. However, for quasi-static channels as experienced in FSO channels, the transmission of feedback information is relatively easier. This has triggered interest in the design of adaptive FSO systems to overcome signal degradations under adverse turbulence and weather conditions where several transmitter parameters can be adjusted according to the channel conditions.

In Chapter 4, we consider spatial dimension as an adaptation parameter in MIMO systems. Historically, the first adaptive FSO system was introduced by Levitt back in 1971 [52] where the period of the binary pulse position modulated (BPPM) symbol is varied according to channel turbulence conditions. In [53], Li and Uysal have investigated a turbo coded FSO system with on-off keying (OOK) where the code rate is adopted as an adjustable transmission parameter. In [54], an adaptive power control strategy is proposed for a satellite-to-ground FSO link aiming to reduce the average power consumption. In [55], Anguita et.al. have presented an experimental demonstration of a coded FSO system where the rates of underlying punctured low-density parity-check (LDPC) and Raptor codes are adjusted to accommodate the varying channel conditions. In [56], Djordjevic has investigated an adaptive modulation and coding (AMC) scheme with M-ary pulse amplitude modulation (M-PAM) and quasi-cyclic LDPC. He has proposed variable-rate variable-power adaptation, channel inversion, and truncated channel inversion schemes. Based on experiments conducted with a commercial FSO link and its scaled-down laboratory prototype, Barsimantov and Nikulin have studied a variable-rate and variable-power adaptation scheme in [57]. In [58], Karimi and Uysal have proposed an adaptive FSO system where transmit power and/or modulation size are varied according to the channel conditions. They have optimized spectral efficiency and average power consumption at a targeted value of outage probability under peak power constraints. The works in [59, 60] have considered the use of adaptive modulation and power control schemes to improve the achievable throughput. In [61], Liu et. al. have studied a coded FSO communication system which uses punctured LDPC codes in a rate-compatible fashion. In [62], an adaptive power control scheme is proposed to reduce the average power consumption of FSO system by regulating transmit amplifier gain. In [63], Mai and Pham have investigated cross-layer design of FSO systems in which automatic repeat request (ARQ) and adaptive-rate transmission are jointly considered to improve the overall system performance.

The aforementioned works on adaptive FSO systems in [52–63] are limited to single-input single-output (SISO) configurations. The design of adaptive FSO systems with multiple apertures either at transmitter and/or receiver side has attracted little attention so far [64–68]. In [64], coherent single-input multiple-output (SIMO) and multiple-input single-input (MISO) FSO systems have been considered. Specifically, the modulation size is adaptively changed based on the channel conditions to maximize the spectral efficiency under constraints on average and peak power. It has been shown that MISO/SIMO FSO systems outperform the SISO counterparts due to available spatial diversity gains. In [65,66], adaptive modulation has been investigated for MIMO FSO systems based on subcarrier intensity modulation. In [67,68], the effect of imperfect feedback channel has been studied for MISO FSO systems with adaptive beamforming.

In the MIMO FSO systems investigated in [64–66], adaptation is performed only through the change in modulation size. In MIMO systems, spatial dimension can be further considered as an adaptation parameter. To be more specific, it is preferable to employ robust diversity methods for channels with adverse turbulence conditions while spatial multiplexing methods can be used in channels with weak turbulence conditions. A judiciously designed switching mechanism makes it possible to extract either spatial diversity or multiplexing gains based on channel conditions. Such switching systems have been earlier studied in the context of MIMO radio frequency (RF) wireless systems [69–72]. For example, in [69], either diversity or multiplexing mode is chosen to minimize the bit error rate. In [70], a hybrid operation mode to extract partial diversity and multiplexing gains is considered. In [71], a combination of coding rate, modulation type, and spatial mode (i.e., either beamforming or spatial multiplexing) is chosen to maximize throughput for a fixed target error rate. Inspired by those works, we propose an adaptive MIMO FSO system with dynamic adaptation between diversity and multiplexing modes of operation. In contrast to coherent RF systems over Rayleigh fading channels studied in [69–72], we consider an FSO system with intensity modulation and direct detection (IM/DD) and assume turbulence-induced fading with log-normal distribution. Atmospheric turbulence channels with typical coherence times of 1-100 ms [73] experience quasi-static fading. Such channels are classified as non-ergodic and the outage probability is typically considered as a main performance metric [74]. For each operation mode, i.e., diversity, multiplexing and hybrid, we first derive the outage probability for MIMO FSO system over log-normal turbulence channels. Then, we formulate the design of adaptive FSO system as to select the MIMO mode that yields the highest throughput while satisfying a predefined target outage probability. Extensive numerical results are provided to demonstrate the performance of proposed adaptive scheme.

1.4 Adaptive Modulation and Power Control

The spatial adaptation can be combined with conventional adaptive modulation and coding (AMC) to give the optimal system performance. In Chapter 5, we formulate the design of adaptive modulation and power control algorithms for multiple aperture FSO systems. Adaptive transmission has been extensively studied in the context of radio communications [75]. In their seminal paper [76], Goldsmith and Varaiya showed that ergodic capacity can be achieved using adaptive transmission based on the availability of channel state information at transmitter side. The work in [76] is based on the assumption that the fading channel changes sufficiently fast during the duration of a codeword. In another seminal paper [77], Caire et. al. assumed a block fading channel and discussed optimal, i.e., capacity achieving, transmission strategies. A detailed survey on adaptive transmission can be found in [78] where guidelines for the design of adaptive coded modulation schemes are discussed including information-theoretic optimal power and rate allocation schemes. It should be however noted that these works typically employ phase shift keying (PSK) or quadrature amplitude modulation (QAM) as modulation types and use coherent detection. Furthermore, they assume Rayleigh, Rician or Nakagami fading channels which are usually employed to characterize multipath wireless channels. Therefore, these results are not directly applicable to FSO systems with IM/DD where typical choice of modulation is unipolar signaling such as on-off keying (OOK), pulse amplitude modulation (PAM), and pulse position modulation (PPM). In addition, FSO systems operate over atmospheric channels with log-normal or Gamma-Gamma turbulence statistics that differ from their RF counterparts.

Taking into account such design choices and channel characteristics, the concept of adaptive transmission has been applied to FSO systems [79–87]. For example, in [80], an experimental demonstration of a coded FSO system was presented where coding rates were chosen as adaptive parameters. In [81], the performance of an adaptive modulation and coding (AMC) scheme with M-ary PAM and low-density parity-check code (LDPC) was analyzed. In [82], the performance improvements through a variable-rate and variable-power adaptation scheme were documented. In [83], a variable-rate adaptation scheme with power control was proposed to optimize spectral efficiency and average power consumption considering constraints on peak power. The works in [84,85] investigated adaptive modulation with power control in an effort to improve the achievable throughput. In [86], the performance of a rate-adaptive FSO communication system with punctured LDPCs was demonstrated under different weather conditions. In [87], a cross-layer design of FSO system was explored where automatic repeat request (ARQ) and variable-rate transmission were jointly considered.

The above works in [79–87] are mainly limited to single-input single-output (SISO) FSO systems. Extension to multiple transmitters/receivers has received only some sporadic efforts. In [88], Chatzidamantis et. al. presented a study on an adaptive multiple-input multiple-output (MIMO) FSO system based on subcarrier intensity modulation with PSK. In their scheme, they used repetition coding to extract diversity gains while varying the modulation size to maximize the spectral efficiency for a pre-defined bit error rate (BER). The work in [88] was further extended in [89] to QAM. The adaptive MIMO FSO systems presented in [88, 89] are based on subcarrier intensity modulation with PSK and QAM. However, it is well known that most practical FSO systems, including the commercially available FSO links in the market, rely on IM/DD principle due to their simplicity and low cost. In a recent work [90], Nouri et. al. considered an adaptive MIMO FSO system with IM/DD and proposed MIMO mode switching to extract diversity or multiplexing gain according to channel conditions. The work in [90] considers only spatial mode as an adaptive parameter and works at a fixed power and for a given modulation type.

In Chapter 5, we consider multiple-input single-output (MISO) and single-input multiple-output (SIMO) IM/DD systems and formulate the design of adaptive modulation and power control algorithms to maximize the spectral efficiency while maintaining a targeted value of outage probability. Unlike the earlier works which consider BER [88, 89], we choose outage probability as a more proper performance metric since atmospheric turbulence channels have time scales ($\approx 10^{-3} - 10^{-2}$ see [91]) far larger than the bit interval and therefore satisfy block fading model. Our design is carried out under peak and average power constraints. While average power constraint determines the overall power consumption and lifetime of laser diodes, the peak power constraint is considered to comply with eye safety standards. Numerical results are provided to present the outage performance of proposed adaptive schemes and to verify their superiority over conventional schemes such as non-adaptive MISO/SIMO as well as adaptive SISO systems.

In conclusion, this thesis propose a promising progress to overcome the main impairments (fog attenuations and turbulence induced fading) of the FSO links in four ways: 1) by examining the channel and proposing novel models and characteristics for atmospheric attenuations 2) by taking advantage of aperture averaging and wavelength dependency 3) by investigating and proposing spatial adaptation in MIMO FSO links and 4) by employing adaptive modulation and power control scenarios and approving the promising performance of adaptive system.

The rest of the thesis is organized as follows: In Chapter II, we describe the FSO channel model under consideration including geometrical loss, atmospheric loss, fog Attenuations, turbulence induced fading and aperture averaging effects on FSO links. In Chapter III, we investigate the information theoretical analysis of DMT for log normal fading channels. In Chapter IV, we present adaptive MIMO FSO communication systems with spatial mode switching. In Chapter V, we propose adaptive modulation and power control for FSO communication systems with multiple apertures. Finally, we conclude in Chapter VI.

Notation: $(\ .\ )^T$ and $|\ .\ |$ denote transpose and determinant operations respectively. $(\ .\ )^\dagger$ and $\|\ .\ \|_F$ denote conjugate-transpose and Frobenius norm operations respectively. $\overline{f(t)}$ is the time average of the signal $f(t)$. Bold upper-case and lower-case letters denote matrices and column vectors respectively. The $(i,j)^{th}$ entry of a matrix $\mathbf{A}$ is denoted by a_{ij} or $[\mathbf{A}]_{ij}$. $E[\ .\ ]$ denotes statistical expectation. $(x)^+$ is equivalent to $\max\{0,x\}$. $\exp(x)$ is exponential function. $\mathbb{R}$ denotes the set of real numbers, $\mathbb{C}$ is set of complex numbers, $\mathbb{Z}_0$ is the set of integers ,and $\mathbb{Z}^+$ is the set of positive integers. $\mathbf{I}_N$ denotes $N \times N$ identity matrix. $X \sim \mathcal{N}(\mu,\sigma^2)$ denotes Gaussian random variable with mean μ and variance σ^2. $\mathbf{X} = diag\{x_1, x_2, ..., x_M\}$ is a $M \times M$ diagonal matrix with non-zero elements denoted by x_i's $i \in \{1, 2, ..., M\}$. The Q-function is defined as $Q(x) = \sqrt{1/2\pi}\int_x^\infty \exp(-u^2/2)\,du$.

CHAPTER II

FSO SYSTEM MODEL AND CHANNEL MODEL

In this section, while we discuss on the analytical models which is proposed for specific atmospheric effects on the propagation of optical signal in free space environment, we explain our measurement methodologies and experimental results which is carried out using our custom designed atmospheric chamber. Commonly, in a simple point-to-point FSO link the received signal $y(t)$ can be expressed as

$$y(t) = RGh_g h_a h_t(t)\left[x(t) * h_{Tx}(t) * h_{Rx}(t)\right] + w(t) \tag{1}$$

where $x(t)$ is the transmitted signal, R is the photodetector responsivity, G is the transimpedance amplifier gain (after photodetector), h_g is the geometrical loss, h_a is the average atmospheric loss, $h_t(t)$ is the scintillation (turbulence), $h_{Rx}(t)$ and $h_{Tx}(t)$ are the impulse response of receiver and transmitter, and $w(t)$ is noise of the system.

We consider intensity modulated direct detection (IM/DD), which is widely employed in practical systems. The electro-optical conversion constant is denoted by $\eta = RG$. In vector domain representation, the received signal, y, suffers from intensity fluctuations due to atmospheric turbulence and losses due to geometrical and absorption, as well as additive noise, and can be well modeled as [92]

$$y = \eta h x + w \tag{2}$$

where x is the transmitted intensity, h is the channel state, y is the resulting electrical signal, and w is signal-independent additive white Gaussian noise (AWGN) with zero mean and variance of σ_w^2.

The channel state, h, models the random attenuation of the propagation channel. In our model, h arises due to three factors: geometrical loss h_g, atmospheric loss h_a, and atmospheric turbulence h_t. The channel state can be formulated as

$$h = h_g h_a h_t \tag{3}$$

Note that h_g and h_a are deterministic where the analytical models and characteristics of them will be discussed in Sections 1 and 2 of this chapter respectively. h_t is random with distribution discussed in Section 3 of this chapter. Since the time scales of this fading processes ($\approx 10^{-3} - 10^{-2}$ s [92]) are far larger than the bit interval, h is considered to be constant over a large number of transmitted bits. This block fading channel is often termed as slow fading or nonergodic channel [93] and outage performances are selected as the criteria. In this channels, h is chosen from a random ensemble according to it's distribution and is fixed over a long block of bits.

Being interested on the atmospheric condition effects on FSO communication systems, in the following, after introducing our custom design atmospheric chamber and link setup, we investigate geometrical and or setup loss, atmospheric loss, and turbulence in details.

2.1 Link Setup

Due to the difficulty to predict the occurrence of specific atmospheric conditions and to repeat the measurements under the same conditions, it is highly desirable to quantify the FSO system performance in a controlled laboratory environment [94, 95]. As shown in Figure 1, our custom-design emulator is in the form of an atmospheric chamber with dimensions of 60 cm $\times$ 40 cm $\times$ 300 cm. It is made from plexiglas with 20 mm thickness. The chamber has two main compartments. The upper compartment includes all electronics and control units while the optical propagation takes place in the lower compartment. On the left- and right-hand sides of lower compartment, we have 5 holes to launch/collect the optical signal. Using adjustable heaters, coolers and fans, the emulator has the capability to create the desired level of turbulence. It also houses a fog generator and droplet watering system to generate different weather conditions. The conditions within the emulator are monitored through temperature, humidity, visibility, altitude, pressure, dust and wind speed sensors. The functioning of the emulator is controlled by a touch screen controller where heat level/uniformity, wind speed/uniformity, rain and fog levels can be adjusted.

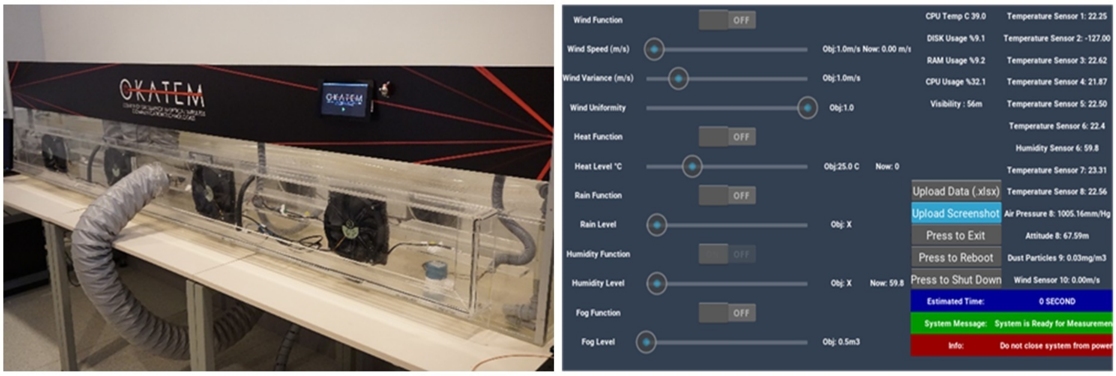

(a) (b)

Figure 1: a) Atmospheric chamber b) control screen.

In our experimental set-up, we use VCSEL infrared lasers with wavelengths of 850, 1310, and 1550 nm. A collimating lens with diameter of $D_{tx} = 5.5$ mm and focal length of $f = 4.51$ mm is used at the transmitter side. At the receiver side, a plano-convex lens of $D_{rx} = 30$ mm and focal length of $f = 75$ mm is used to collect the power. We use photodetectors with aperture sizes of $D = 1$, 3.6, 8.7 mm. We set beam divergence angles θ_{tx} =14, 17 and 20 mrad by adjusting the distance between collimating lens and laser. The link distance (i.e., length of chamber) is $L = 3$ m. The maximum optical power is 10 mW for 850 nm laser and 5 mW for 1310 and 1550 nm. The specifications of the link setup are summarized in Table 2.

Please note that for the experiments of aperture averaging effect, at the receiver side, plano convex lens is removed to only consider the effects of aperture size.

Table 2: Specifications of the Link Setup

	Parameters	Values
Transmitter	Wavelength	$\lambda = 850$, 1310, 1550 nm
	Maximum optical power	$P = 10$, 5, 5 mW
	Beam diameter at TX aperture	$b = 3$, 6, 2 mm
	Beam divergence	$\theta_{tx} = 14$, 17, 20 mrad
	Lens diameter	$D_{tx} = 5.5$ mm
	Lens focal length	$f = 4.51$ mm
Channel	Dimension	$3 \times 0.4 \times 0.6$ m^3
	Link distance	3 m
Receiver	Detector types	Si, Avalanche
	PD absorption ranges	350-1100, 1000-1700 nm
	Plano-convex lens	$D_{rx} = 30$ mm, $f = 75$ mm
	PD responsivity	0.65 mA/W
	Efficiency	90% - 95%

2.2 Geometrical Loss

In a point-to-point FSO link, the received power P_{rx} can be expressed as

$$P_{rx} = P_{tx} - h_g - h_a \ \ [dB] \tag{4}$$

where P_{tx} is the transmit power. To measure the geometrical loss of the system setup in the custom design atmospheric chamber, we need to average the received power to reduce the effect of noise and scintillation and we have

$$h_g = P_{tx} - P_{rx} - h_a \ \ [dB] \tag{5}$$

Usually the atmospheric loss (h_a) is significant for foggy weather or when the water-vapor density is considerably high, but it can be ignored for clear weather conditions compared to the geometrical loss. An unguided electromagnetic wave propagating in free space experiences power loss at the receiver end due to the geometry of diffraction combined with the limited effective area of the receiver. The geometric loss is the loss in power of signal which occurs due to divergence of the laser beam (Fig. 2).

In order to maintain the link, the FSO systems needs to be engineered in such a way that when the beam wobbles, some part of it always hit the receiver.

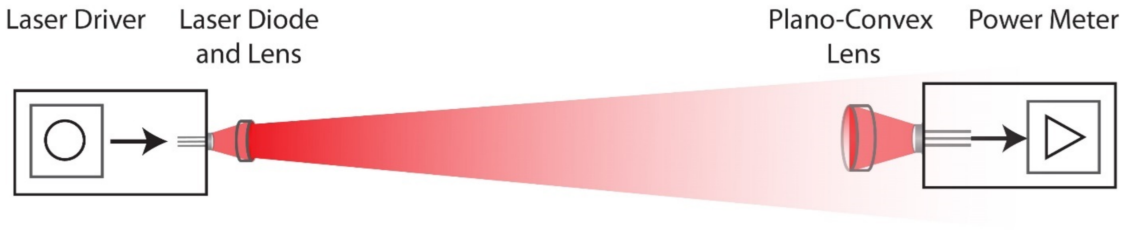

Figure 2: Divergence of FSO beam.

Understanding the beam shape geometric of the transmitting laser happens to be critical for the analysis of geometrical loss. Usually the analytical model is provided for ideal uniform and Gaussian beam shapes. However, it is evident that the geometrical loss formulas are due to change for other beam shapes than uniform and Gaussian beam profile. We also look into the beam shape of currently used laser in our experiment and it happens to be different than ideal beam shapes. In the following, we come up with models to accurately capture the characteristics of practical beam shapes.

2.2.1 Uniform Beam

Under the assumption of perfect alignment, geometrical loss (h_g) will be analyzed in order to quantify the effect of different beam shape profiles. Under the assumption of uniform beam profile (see Fig. 3), the area of the beam at the receiver can be calculated using a simple geometrical formula. The reduction in optical power at the receiver due to the geometrical loss can be estimated by [96]

$$h_g = \frac{D_{rx}^2}{\left(D_{tx} + \tan\left(\theta_{tx}\right) L\right)^2} \approx \frac{D_{rx}^2}{\left(\theta_{tx} L\right)^2} \qquad \text{if} \qquad D_{rx} < D_{tx} + \tan\left(\theta_{tx}\right) L \tag{6}$$

where D_{rx} is the receiving lens diameter, D_{tx} is the transmitting lens diameter, θ_{tx} is the transmitted beam divergence angle, and L is the propagation distance. Typically in an FSO link, the divergence angle θ_{tx} and D_{tx} are small enough where Paraxial approximation holds and can be used in (6). Further, if the area of the beam at the receiver is less than the aperture, we have $h_g = 1$ and there is no geometrical loss.

Typically in an outdoor FSO system, the divergence angle is in the order

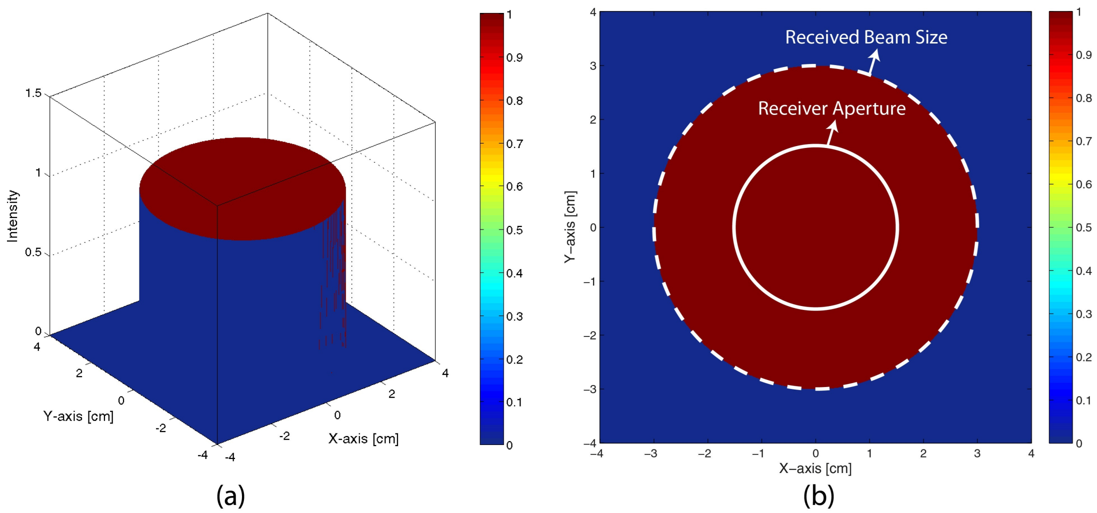

Figure 3: (a) Uniform beam shape profile in 3D view, (b) Uniform beam shape profile with receiver aperture.

of mrad and over long distances, the received beam is about multi times bigger than the receiver aperture. Here also, to mimic the practical outdoor systems and carefully observing the effect of weather conditions on the beam we generate wide beams by engineering the divergence angle. To measure the beam divergence angle, θ_{tx}, we need to look at the wave-front of the beam at specific distances. For this purpose, we take two photos of the beam wave-front 100 mm apart and measure the beam width at each distance. For calculating the divergence angle we have $\tan\left(\theta_{tx}/2\right) = \left(r_2 - r_1\right)/d$ where in our case $d = 100$ mm distance and r_1, r_2 are the beam radius at position 1 and 2 (see Fig. 4).

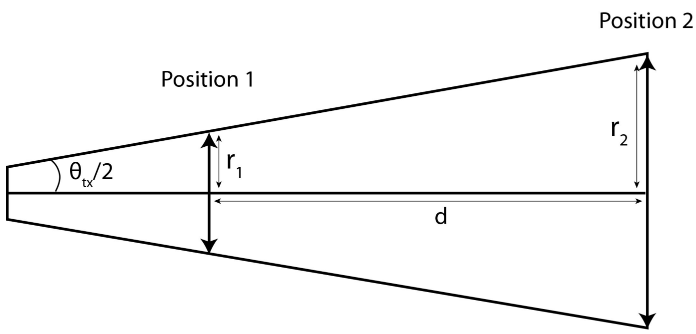

Figure 4: Divergence angle calculation method.

To explore the geometrical loss of the custom-design link over atmospheric chamber, we set beam divergence angles θ_{tx} =14, 17 and 20 mrad by adjusting the distance between collimating lens and laser. The link distance (i.e., length of chamber) is $L = 3$ m. The transmit power of laser (P_{tx}) is changed from 1 to 10 mW. The average received power (P_{rx}) is measured and plotted in Fig. 5. Noting that atmospheric loss is zero (i.e., $h_a = 0$) under clear weather conditions, the analytical results based on (6) are also included in Fig. 5. It can be observed that experimental and analytical results match each other well with a small difference about 0.34 dB. This difference comes from optical loss of the system and power detector's efficiency (i.e., 97% efficiency) as well as the fact that our laser diode produces a top-hat beam shape while (6) assumes a uniform beam profile.

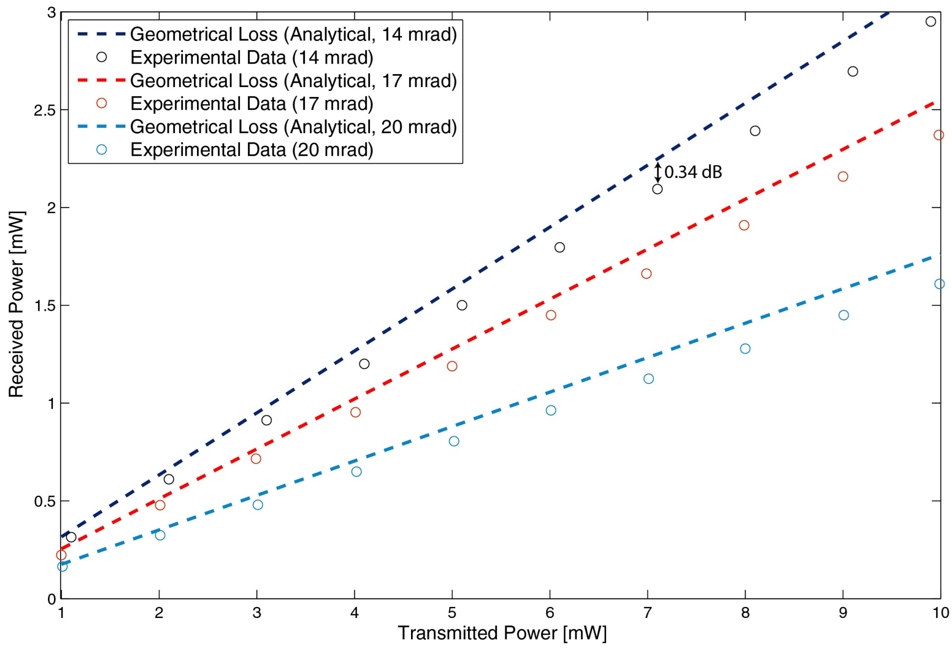

Figure 5: Geometrical loss for different divergence angles.

Further, for the case of transmit power equal to 10 mW and $\theta_{tx} = 20$ mrad we provide a link budget analysis of the link in Table 3. For this specific case h_g is calculated from (6) and compared with the value of table 1 which confirms the accuracy of measurements.

Table 3: A Link budget analysis

Description	Value (mW)	Value (dB)
Transmit Power	10.00 mW	10 dBm
Pointing Loss	-	0 dB
Setup Loss	-	-0.34 dB
Geometrical Loss	-	-7.60 dB
Received Power	1.61 mW	2.06 dBm

2.2.2 Gaussian Beam

For a Gaussian beam (see Fig. 6) an analytic geometrical formula can be developed. Denoting the normalized intensity profile at the receiver plane by $I_L(r)$, we have

$$I_L(r) = \exp\left(-\frac{2r^2}{w_L^2}\right) \tag{7}$$

where r is the radial is distance and w_L is the half beam width at the receiver. The geometrical loss can be found by calculating the portion of power collected by the detector to the total power at the receiver plane. Therefore, we have

$$h_g = \frac{P_{received}}{P_{total}} = \frac{\int_0^{2\pi}\int_0^{D_{rx}/2} \exp\left(-\frac{2r^2}{w_L^2}\right) r dr d\theta}{\int_0^{2\pi}\int_0^{\infty} \exp\left(-\frac{2r^2}{w_L^2}\right) r dr d\theta} \tag{8}$$

By performing the integrals in (8), the geometric loss can found as

$$h_g = 1 - \exp\left(-\frac{D_{rx}^2}{2w_L^2}\right) \tag{9}$$

where under Paraxial approximation, $w_L \approx L \cdot \theta_{tx}/2$ is the half beam width (calculated at e^{-2} of maximum intensity) at propagation distance L.

2.2.3 Top-hat Beam

While theoretically the ideal beam shapes like uniform and Gaussian are considered for calculation of geometrical loss formula as in (6) and (9), in reality, the beam shape of the lasers is not an ideally distributed profile. For example, we use a VCSEL laser and look at its beam shape profile using a beam profiler. Fig. 7,

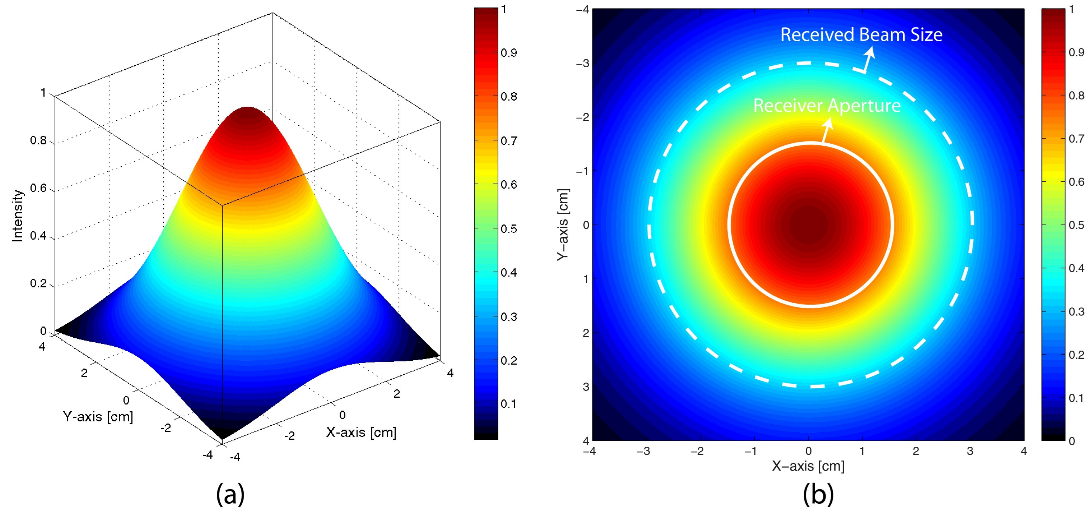

Figure 6: (a) Gaussian beam shape profile in 3D view, (b) Gaussian beam shape profile with depicted received beam size and aperture.

shows beam profile of this laser and as it can be seen from the figure, it can be very well estimated by a Top-hat beam shape with super-Gaussian profile distribution which lies between a uniform and Gaussian beam shape [97].

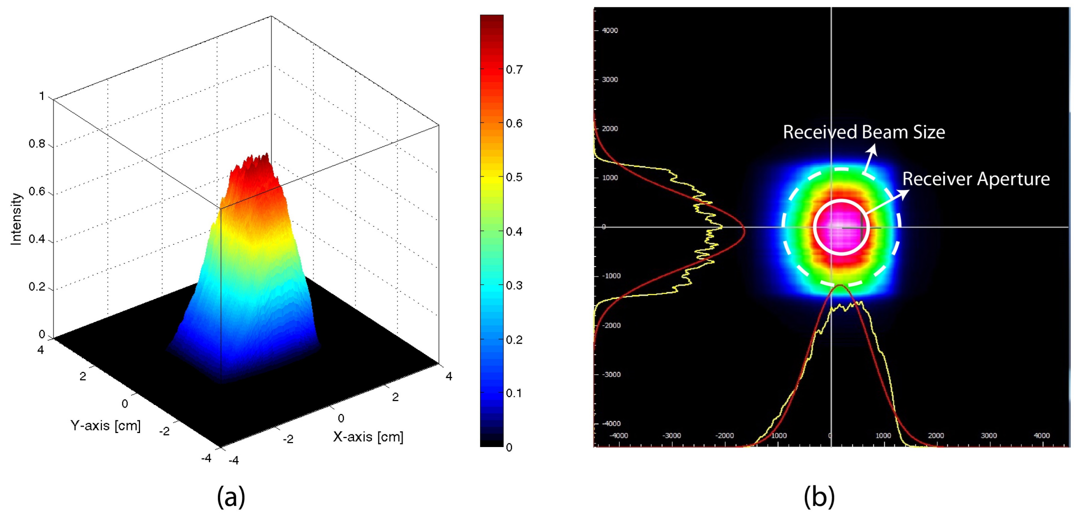

Figure 7: (a) Top-hat beam shape profile in 3D view (VCSEL laser), (b) Top-hat beam shape profile with depicted received beam size and aperture.

Therefore, an accurate mathematical analysis for calculating the geometrical loss of practical top-hat beam shape with super-Gaussian profile distribution is investigated in the following. A more general formulation of a Gaussian profile with a flat-top and Gaussian fall-off can be represented by rectangular super-Gaussian (higher-order Gaussian) and is often used for realistic beam formulation [97]. The normalized intensity profile can then be written as

$$I_L\left(x,y\right) = \exp\left(-2\frac{x^{2n}+y^{2n}}{w_L^{2n}}\right) \tag{10}$$

where the profile orders n determines the degree of convergence where for a top-hat beam shape we have $n \gg 1$. The closer the order n to 1, the profile approaches to Gaussian and for $n = 1$, the intensity profile is Gaussian distributed. For $n \to \infty$, the profile converges to an ideal uniform beam shape. The geometrical loss can be found by calculating the portion of power collected by the detector to the total power at the receiver plane. Therefore, we have

$$h_g = \frac{P_{received}}{P_{total}} = \frac{\int\limits_{-D_{rx}/2}^{D_{rx}/2}\int\limits_{-z}^{z} \exp\left(-2\frac{x^{2n}+y^{2n}}{w_L^{2n}}\right) dydx}{\int\limits_{-\infty}^{\infty}\int\limits_{-\infty}^{\infty} \exp\left(-2\frac{x^{2n}+y^{2n}}{w_L^{2n}}\right) dydx} \tag{11}$$

where $z = \sqrt{\left(D_{rx}/2\right)^2 - x^2}$. To perform the integrals in (11) we approximate by an integration over a square of equal area to the detector, i.e., with side length $\sqrt{\pi}D_{rx}/2$. The integrals in (11) can also be simplified by change of variable. We replace $u = 2^{1/2n}x/w_L$. Therefore we can write (11) as

$$h_g = \frac{\left[\int\limits_0^{2^{(1-4n)/2n}\sqrt{\pi}D_{rx}/w_L} \exp\left(-u^{2n}\right)du\right]^2}{\left[\int\limits_0^{\infty} \exp\left(-u^{2n}\right)du\right]^2} = \frac{\left[\Gamma\left(\frac{1}{2n}\right) - \Gamma\left(\frac{1}{2n}, \frac{\pi D_{rx}^{2n} 2^{1-4n}}{w_L^{2n}}\right)\right]^2}{\left[\Gamma\left(\frac{1}{2n}\right)\right]^2} \tag{12}$$

The integrals in (12) can be solved by use of incomplete gamma function having $\int e^{-u^n}du = -\Gamma\left(1/n, u^n\right)/n$. Replacing it in (12), the geometrical loss can be written as

$$h_g = \left[1 - \frac{\Gamma\left(\frac{1}{2n}, \frac{\pi D_{rx}^{2n} 2^{1-4n}}{w_L^{2n}}\right)}{\Gamma\left(\frac{1}{2n}\right)}\right]^2 \tag{13}$$

As a special case, replacing $n = 1$ in (13) and noting that $\Gamma\left(1\right) = 1$ and $\Gamma\left(1,x\right) = \exp\left(-x\right)$, the geometrical loss will be similar to (9) as for Gaussian beam profile. On the other hand, letting $n \to \infty$ in (12) and noting that $\lim\limits_{n\to\infty} \int_0^{\infty} \exp\left(-u^n\right)du =$

1 and $\lim_{n\to\infty} \int_0^a \exp(-u^n)\, du = a$ for $a < 1$, the geometrical loss will be similar to (6) as for uniform beam shape letting $w_L \approx L \cdot \theta_{tx}/2$.

In Fig. 8, we set beam divergence angle $\theta_{tx} = 25$ mrad by adjusting the distance between collimating lens and laser. The transmit power of laser (P_{tx}) is changed from 1 to 10 mW. The average received power (P_{rx}) is measured and plotted in Fig. 8. Noting that atmospheric loss is zero (i.e., $h_l = 0$) under clear weather conditions, the analytical results based on (6), (9) and (13) for uniform, Gaussian, and super-Gaussian profiles are also included in Fig. 8. It can be observed that for super-Gaussian profile with order of $n = 5$, experimental and analytical results match each other very well. This comes from the fact that our laser diode produces a top-hat beam shape with super-Gaussian distribution profile of $n = 5$.

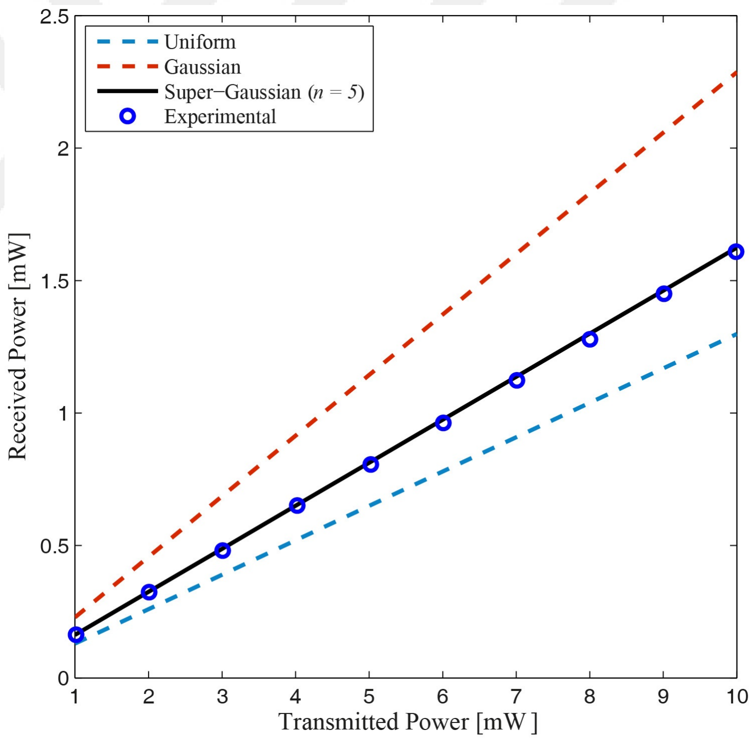

Figure 8: Matching experimental data to super-Gaussian distribution profile.

In Fig. 9, we plot the geometrical loss for different divergence angles. Specifically, we consider uniform, Gaussian, and top-hat beams with super-Gaussian profiles based on (6), (9) and (13) respectively. Further, for top-hat beams we plot the geometrical losses for the super-Gaussian orders of $n = 1, 2, 3, 5, 10$, and 30. Fig. 9 shows that super-Gaussian profile distribution lies between ideal uniform and Gaussian profiles. Specifically, For $n = 1$ the geometrical loss of super-Gaussian and Gaussian profiles match each other. By increasing the order, n, from 1 to higher values the geometrical loss of top-hat beam shape converges toward uniform profile.

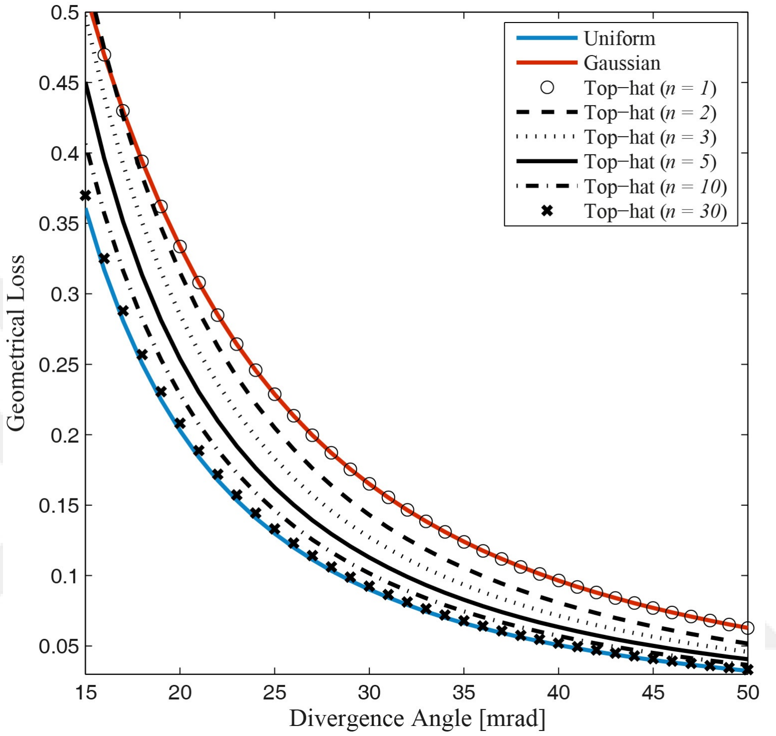

Figure 9: Geometrical loss of Top-hat beam shape for different values of n.

2.3 Atmospheric loss and Fog Attenuation

Atmospheric loss includes weather conditions such as rain and fog. Rain has a distance-reducing impact on FSO, although its impact is significantly less than that of fog. This is because the radius of raindrops (200–2000 μm) is significantly larger than the wavelength of typical FSO light sources. Fog is the most detrimental weather phenomenon to FSO because it is composed of small water droplets with radii about the size of near infrared wavelengths. Weather conditions are typically referred to as fog when visibilities range between 0–4,000 meters.

2.3.1 Existing Models

According to Beer's law, the attenuation of light traveling through the atmosphere due to both absorption and scattering is given as [98]

$$h_a = \exp\left(-\alpha_{\text{fog}} L\right) \tag{14}$$

where α_{fog} is the fog attenuation coefficient. It is defined as [98]

$$\alpha_{\text{fog}} = \left(3.91/V\right)\left(\lambda/\lambda_0\right)^{-q} \tag{15}$$

where V is the visibility in km, λ_0 =550 nm is the maximum spectrum of solar band (i.e., green light) and q is a parameter that can be determined from experimental data. According to the Kruse model [98], we have

$$q = \begin{cases} 0.585V^{1/3} & V < 6\text{km} \\ 1.3 & 6\text{km} < V < 50\text{km} \end{cases} \tag{16}$$

According to Kim's model [99], q is given by

$$q = \begin{cases} 1.6 & \text{for} \quad V > 50 \ \text{ km} \\ 1.3 & \text{for} \quad 6 < V < 50 \ \text{ km} \\ 0.16V + 0.34 & \text{for} \quad 1 < V < 6 \ \text{ km} \\ V - 0.5 & \text{for} \quad 0.5 < V < 1 \ \text{ km} \\ 0 & \text{for} \quad V < 0.5 \ \text{ km} \end{cases} \tag{17}$$

In a recent work [12], Ijaz et al. argue that the Kim model overestimates the fog attenuation for low visibility and propose

$$q = 0.1428\lambda - 0.0947 \ , \qquad V < 1 \quad \text{km} \tag{18}$$

2.3.2 Fog Attenuation Measurements

We conduct a measurement campaign using our own atmospheric emulator in an effort to validate the existing models in the literature. We use three laser diodes operating at λ =850, 1310, and 1550 nm. A green laser (λ_0 =550 nm) is simultaneously launched to measure the visibility. We repeat fog injection 5 times during the experiment with a duration of 4000 seconds. In Fig. 10, we plot normalized received power, i.e., $h_a = P_{rx}^{\text{fog}}/P_{rx}^{\text{clear}}$ where P_{rx}^{clear} and P_{rx}^{fog} respectively denote average received power in clear and foggy conditions. Based on the received power associated with green laser, the visibility values are estimated and thereby different regimes of fog [98] can be defined, i.e., dense fog ($V < 0.5$ km), medium fog ($0.5 < V < 1$ km), light fog ($1 < V < 2$ km), and haze ($2 < V < 4$ km). It is observed that at the beginning of each injection, the received powers for all wavelengths drop down very fast. The power reduction is relatively less for higher wavelengths. This could also be seen from (15) where larger wavelengths result in smaller fog attenuation coefficients.

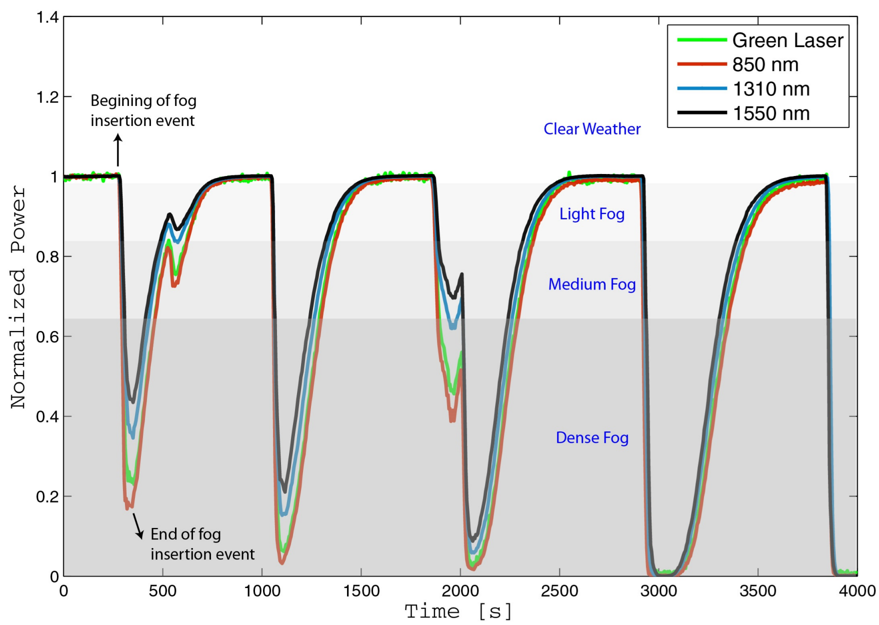

Figure 10: Normalized received power in time during fog events.

In Figs. 11.(a-c), the fog attenuation coefficient is shown in dB/km with respect to visibility for 850, 1310, and 1550 nm wavelengths, respectively, on a log-log scale. Here, we consider visibility ranges up to 1 km which includes dense and medium fog regimes. The attenuation coefficients are calculated from $\alpha_{\text{fog}} = -\log(h_a)/L$. Furthermore, we include a fitted curve in the form of $\alpha_{\text{fog}} = aV^{-b}$ where the coefficients a and b are chosen based on our experimental data. The existing models (Kim, Kruse, and Ijaz models) are further plotted as benchmarks.

It is observed from Fig. 11.a that our fitted curve is in a good agreement with Ijaz model for 850 nm. However, this is not the same for 1310 nm and 1550 nm results (see Figs. 11.b and 11.c) which show better agreement with Kruse model. For all three wavelengths under consideration, Kim's model fails to provide a good match. Furthermore, both Ijaz and Kim models overestimate the fog attenuation at λ =1310 and 1550 nm. In an attempt to compare the three wavelengths under consideration, we plot our fitted curves together in Fig. 11.d. It is observed that the higher the wavelength, the less is its fog attenuation coefficient and more robust to foggy weather conditions. For example, at a visibility of $V = 0.5$ km, the fog attenuation coefficients are calculated as α_{fog} =31.5, 23.5, and 20.3 dB for λ =850, 1310 and 1550 nm respectively.

2.3.3 Proposed Model

Having observed these discrepancies between the old models (i.e, Kruse, Kim, and Ijaz models), here we propose our new hybrid model of fog attenuation coefficient by accurately modeling the behavior of q parameter in (15). Kruse and Kim proposed that q parameter is a function of visibility. On the other hand, Ijaz et. al. in [12] show that q parameter is a function of λ. Here, for all the three wavelength we observe the behavior of q parameter with respect to visibility. We find that the q parameter is a function of both visibility, V and λ where it can be estimated from the numerical results according to the following expression, i.e,

$$q\left(\lambda, V\right) = \frac{\log\left(3.91\right) - \log\left(V\right) - \log\left(\alpha_{fog}\right)}{\log\left(\lambda/\lambda_0\right)} \tag{19}$$

Furthermore, using fitting methods and in an attempt to exactly capture the behavior of q parameter, we propose our new hybrid model of fog attenuation as

$$q\left(\lambda, V\right) = \left(-1.36 \times 10^{-7}\lambda^2 + 4.31 \times 10^{-4}\lambda - 0.228\right)\left(\ln\left(V\right) + 5\right) \tag{20}$$

where λ is in nm and V is in km. The proposed model is plotted in Fig. 12 for three wavelengths of 850, 1310, 1550 nm. Further, in Fig. 12, we plot $q\left(\lambda, V\right)$

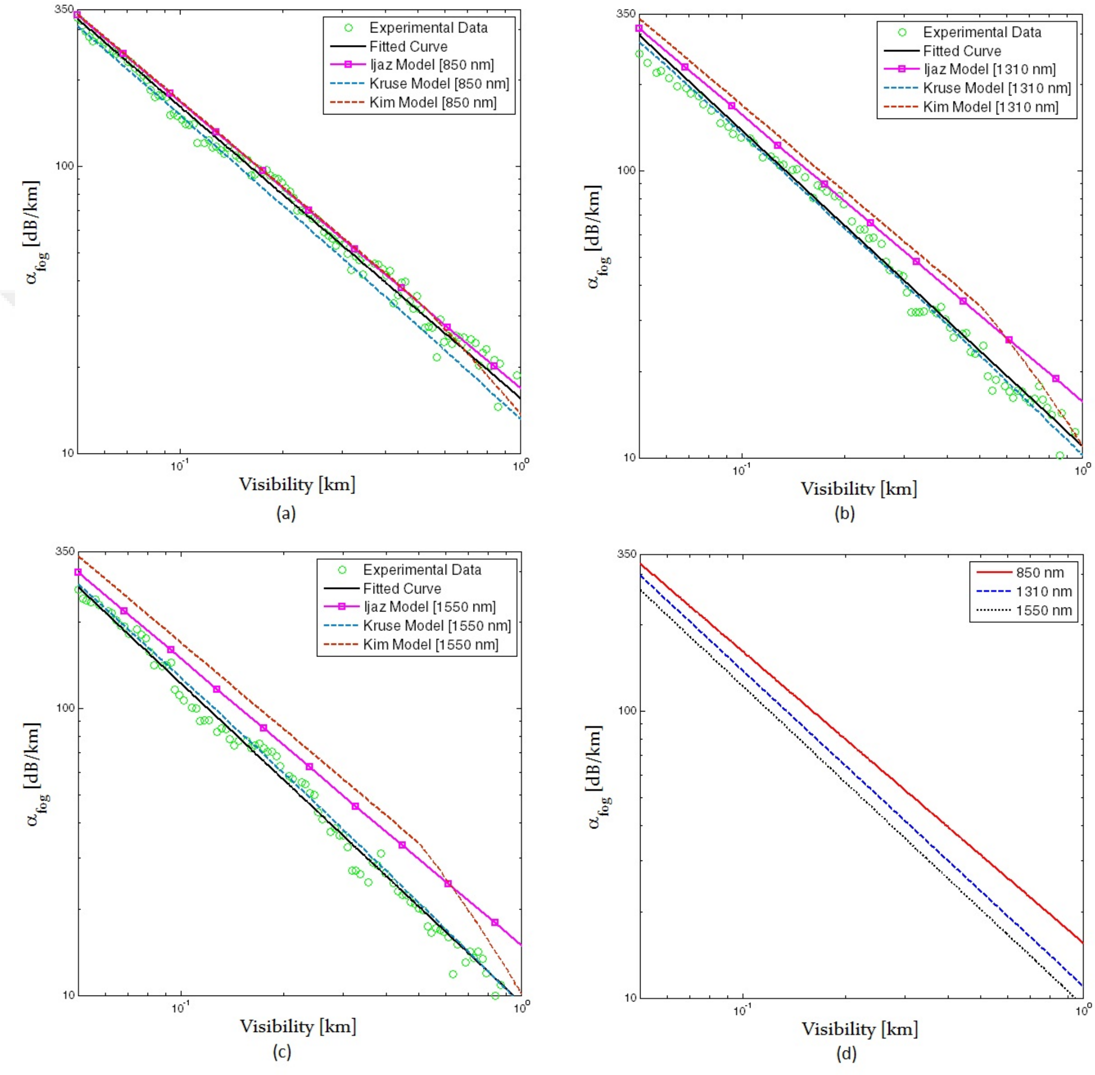

Figure 11: Attenuation coefficient with respect to visibility for a) 850 nm, b) 1310 nm, c) 1550 nm; d) Comparison of fitted curves for three wavelengths.

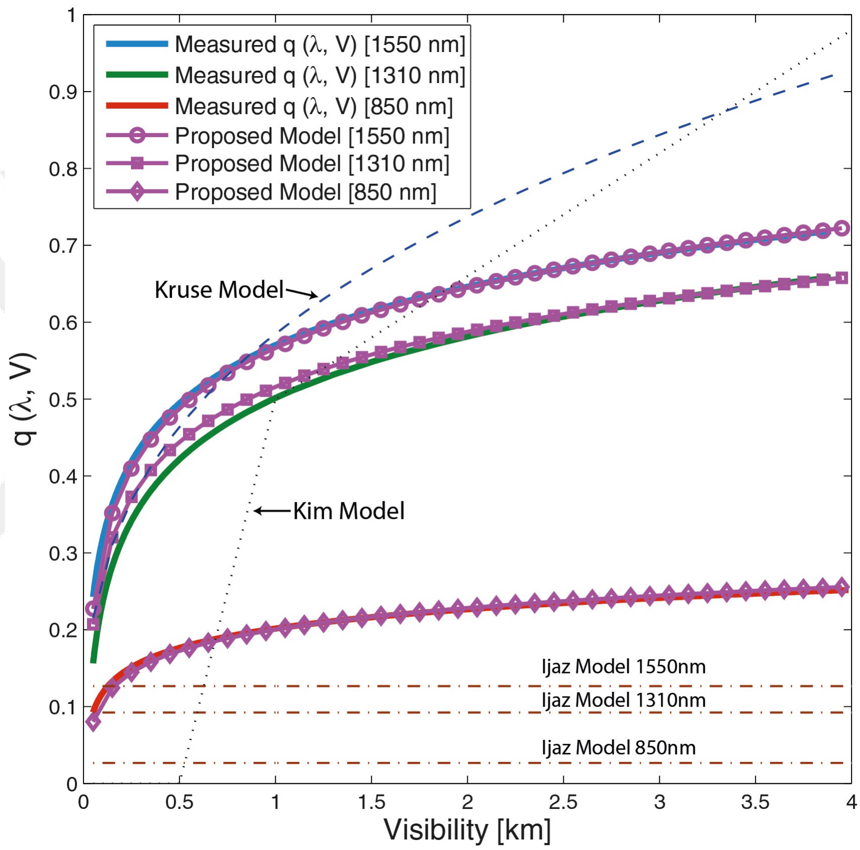

Figure 12: Comparison of the proposed model for q parameter with experimental data.

from the experimental results and according to (19) for three wavelengths of 850, 1310, and 1550 nm. The Kruse and Kim models of q parameter which are only the function of visibility is also plotted in the figure. It can be seen that Kruse tried to capture the behavior of q parameter with $V^{1/3}$ which is more realistic than Kim that suggests a linear behavior. Ijaz et. al. suggested that the q parameter is a function of only wavelength which is plotted in the figure for the three wavelengths. Leaving the dependency of q parameter on the visibility, the Ijaz model can only be considered for low wavelength values. It can be observed that while the proposed model is capturing the behavior of q parameter, it is the function of both wavelength and visibility.

2.4 Turbulence

Atmospheric turbulence is a major impairment in FSO communication systems. Based on the fact that the size of receive aperture is much larger than operation wavelength, aperture averaging extracts inherent receive diversity gains and can be used as an effective fading mitigation technique. We focus on three most common wavelengths used in telecommunications, namely 850 nm, 1310 nm, and 1550 nm and present a comparative performance evaluation of aperture averaging under the same emulated atmospheric conditions. The main motivation of our work is to investigate the trade-off between wavelength and aperture size in the context of aperture averaging. Employing the atmospheric chamber, we conduct experiments over a link distance of 3 m. Plano convex lens is used to expand the laser beam to mimic the condition of outdoor transmission. At the receiver side, three aperture diameters of 1, 3.6, 8.7 mm are employed. For each of the wavelengths under consideration, received powers are recorded at high sampling rates to characterize the turbulence induced fluctuations. Based on these samples, the PDF of atmospheric turbulence channel fading coefficients are determined and compared for wavelengths of 850, 1310, and 1550 nm.Our results demonstrate that by changing the wavelength and/or aperture size, a strong turbulence condition with Gamma-Gamma statistics can turn into a weak turbulence condition with log-normal statistics. Such a phenomena can be observed even for relatively small aperture sizes if the wavelength is sufficiently high.

2.4.1 Turbulence Measurements

In the atmospheric chamber, heaters are used to adjust the temperature levels along the link range. In this way a temperature differential is produced within the chamber to generate a controlled level of turbulence. Specifically, temperature is kept in the range of 20 - 80°C. Relatively high degrees of temperature are necessary to generate sufficiently high turbulence levels for the short link distance considered in our experiment.

Eight temperature sensors are placed at distances of 0, 20, 70, 120, 170, 220, 270, and 300 cm along the length of the chamber. Each sensor records the temperature at each 4 seconds through the duration of the experiments ($\sim$ 20 mins). Let $T_i,\ i = 1, 2, ..., 8$ denote the instantaneous temperatures recorded by each sensor. The average temperatures are calculated as $\bar{T}_i = \langle T_i \rangle,\ i = 1, 2, ..., 8$ based on the averaging over 300 samples where $\langle . \rangle$ denotes time average. These values are provided in Table 4.

Table 4: Average of Measured Temperatures (°C)

$\bar{T}_1$	$\bar{T}_2$	$\bar{T}_3$	$\bar{T}_4$	$\bar{T}_5$	$\bar{T}_6$	$\bar{T}_7$	$\bar{T}_8$
81.7	23.0	25.7	23.9	24.1	22.0	23.0	21.9

We can calculate the temperature structure constants along the transmission path as [4]

$$C_{T_i} = \sqrt{\frac{\left\langle (T_i - T_{i+1})^2 \right\rangle}{R^{2/3}}} \qquad \text{for} \qquad i = 1, 2, ..., 7 \tag{21}$$

The atmospheric structure constant can be then calculated by [4]

$$C_n^2 = \left(79 \times 10^{-6} \frac{P}{T^2} \right)^2 \bar{C}_T^2 \tag{22}$$

where $\bar{C}_T = (1/7) \sum_{i=1}^{7} C_{T_i}$ is the average of temperature structure constants, $P = 1007$ millibar (measured) is the indoor atmospheric pressure, and $T = 295k$

is the average temperature in Kelvin at the receiver. Replacing these within (22), we obtain the atmospheric structure constant as $C_n^2 = 3.5 \times 10^{-10}$. The Rytov variance can be then found as $\sigma_R^2 = 1.23 C_n^2 k^{7/6} L^{11/6}$ [4] where $k = 2\pi/\lambda$ is the wavenumber.

At the receiving end, no collecting lens is used to accurately observe the effect of aperture averaging. We employ photodetectors with active areas of $D = 1$, 3.6, and 8.7 mm. The voltage signal out of photodetector is fed to an oscilloscope with high sampling rate. Irradiance fluctuations are directly proportional to the amplitude variations of the received voltage. Based on the histogram of normalized (i.e. normalized by mean values) irradiance fluctuation samples, we obtain the PDF of turbulence-induced fading channel coefficient.

We modulate the optical signal with 1 MHz sinusoidal. A critical issue in signal acquisition is sampling rate and removal of noise effects. The coherence time of turbulence channels is typically in the order of tens of millisecond (categorized as slow-fading channel). Hence, a sampling rate of 100 K Sample/sec would be sufficient. However, to minimize the effect of noise on the measurements, we use an acquisition sampling rate of 10 M sample/sec, i.e, 1 sample for each 0.1 μsec. The frequency of the signal is 1 MHz, indicating that the signaling period is 1 μsec. The electrical voltage signal is recorded over a duration of 1 sec interval to meet the resolution of 10 M sample/sec for the oscilloscope. Therefore, we have 10 samples per period of sinusoidal signal (i.e., 1 μsec). To acquire sufficiently large number of samples for averaging purposes, we repeat this process 60 times (equivalent of 60 seconds). The recorded data is processed and the entire block of data samples is divided into smaller blocks of 100 sample per block. Each block undergoes fast Fourier transform (FFT). FFT decomposes the signal into its frequency components. Therefore, it gives the opportunity to only focus on the signal of interest located at 1 MHz. Noise terms in other frequencies become irrelevant in this case. In an attempt to reduce the effect of noise, we further average measurement results of each 5 blocks. As an example, Fig. 13 presents one recorded instance of the received signal (blue plot) and normalized irradiance fluctuations (red plot) over 10 sec time interval.

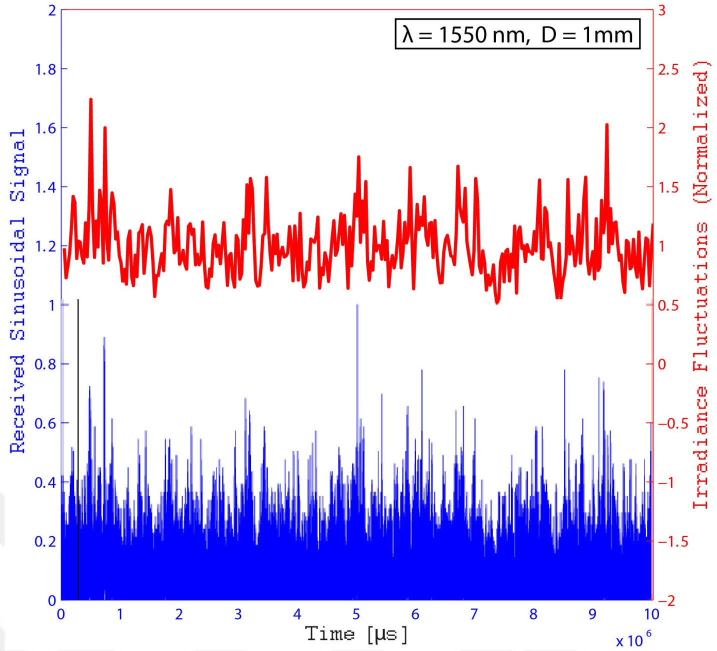

Figure 13: An instance of normalized irradiance fluctuations. 1550 nm laser and photodetector with 1mm diameter are used.

As a final remark, it should be emphasized that the correlation scale of the irradiance fluctuations is defined by the size of the Fresnel zone; thus, significant effects of aperture averaging can be observed only when $D/2 > (L/k)^{1/2}$. In our experiment, we have a path link of $L = 3$ m and the Fresnel zones for the laser diodes with wavelengths of 850 nm, 1310 nm and 1550 nm are calculated to be 0.65, 0.80 and 0.88 mm respectively. As mentioned above, we use photodetectors with active areas of at least 1 mm in diameter. Although a 1 mm aperture is very small and acts like a point receiver in outdoor environment, the effect of aperture averaging can be observed due to the short link distance in our case.

2.4.2 Experimental Results and Discussions

In the following, we present the PDF of the log irradiance, i.e., $\ln(I)$ for three wavelenghts under consideration. In our figures, we use log-scale axis to have precise comparisons especially at tails of the distributions which highly affect the error rate performance of optical systems.

In Figure 14, we consider $\lambda = 850$ nm and present the PDF of the log irradiance for aperture sizes of $D = 1$, 3.6, 8.7 mm under consideration. As the indicator of turbulence strength, we adopt scintillation index. The scintillation indices of $\sigma_I^2 = 0.23$, 0.03 and 0.006 are estimated from the PDF of experimental results. As expected, the higher the aperture size the less it is affected by the turbulence. Larger apertures are able to average out the turbulences with correlation widths less than the aperture size. To verify the accuracy of the measurements, we use the estimated value of Rytov variance $\sigma_R^2 = 0.4$ and calculate the scintillation index using the expression in [4, Ch.10, P.413, Eq.(69)]. This yields $\sigma_I^2 = 0.228$, 0.031, 0.005 which are in good agreement with the above estimated values. LN and GG distributions are plotted as benchmarks. For $D = 1$ mm, it can be observed that GG distribution better matches to experimental data in comparison to LN distribution. In particular, a precise match is observed for the left tail of PDF which is particularly critical for performance analysis of communication systems [4,17,18]. It is observed that LN PDF underestimates the behavior in the left tail as compared with measurement results. Since detection probabilities are primarily based on the left tail of the PDF, underestimating this region significantly affects the accuracy of performance analysis. By increasing the aperture diameter to $D =$ 3.6 and 8.7 mm, the turbulence effect is somewhat compensated and PDF shifts toward LN distribution due to effect of aperture averaging. For these aperture values, it can be observed that GG and LN curves coincide.

In Figure 15, we consider wavelength of $\lambda = 1310$ nm and diameter of $D = 1$ mm. Comparison with measurement results at $\lambda = 850$ nm reveals that the degrading effect of atmospheric turbulence is less. Specifically, a scintillation index of $\sigma_I^2 = 0.07$ is obtained which is smaller than $\sigma_I^2 = 0.23$ measured for $\lambda = 850$ nm. It is observed that while GG distribution is in better agreement with the left tail for λ =850 nm, LN distribution interestingly has a slightly better match to the left tail of the distribution at λ =1310 nm.

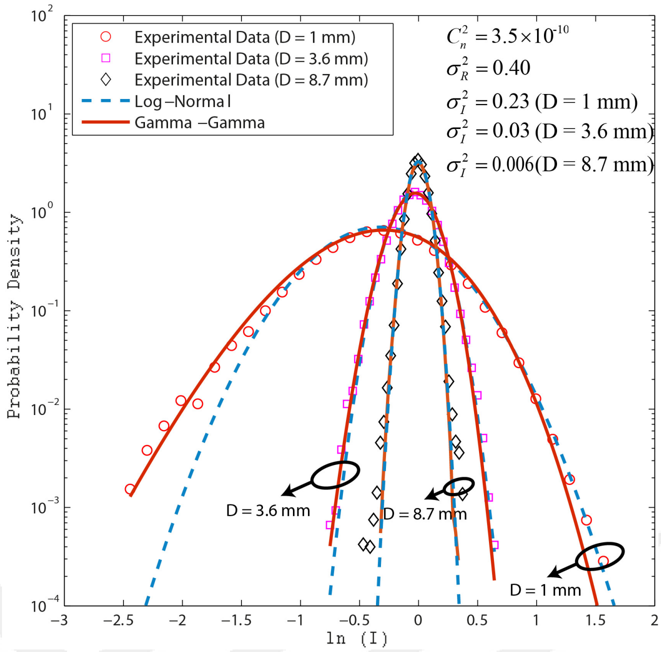

Figure 14: PDF for $\lambda = 850$ nm assuming $D = 1$, 3.6, 8.7 mm.

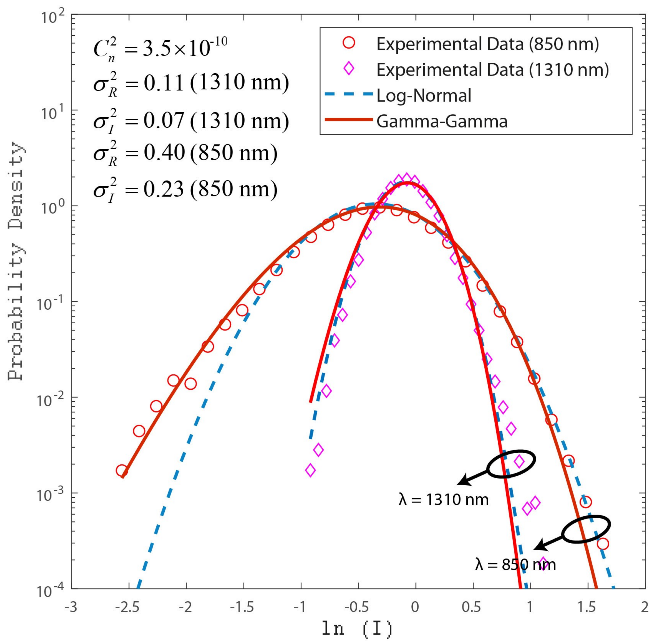

Figure 15: Comparison of measurement results at $\lambda = 850$ nm and $\lambda = 1310$ nm for $D = 1$ mm.

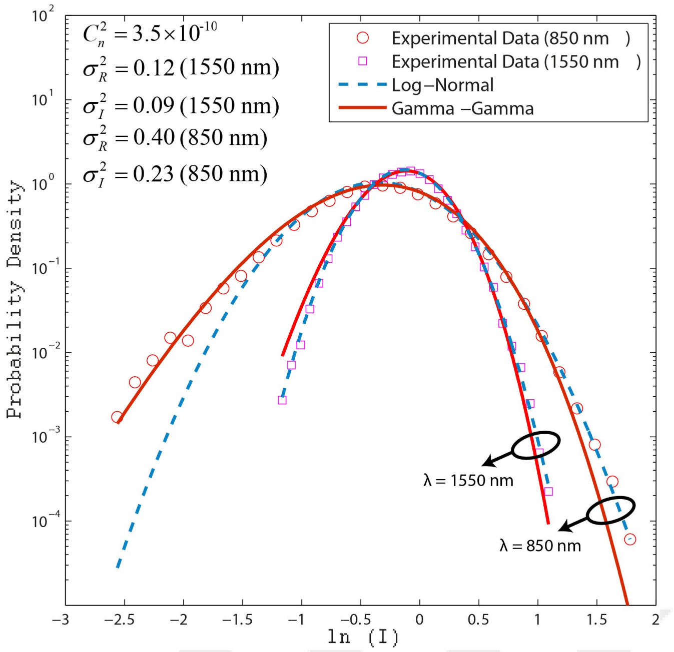

Figure 16: Comparison of measurement results at $\lambda = 850$ nm and $\lambda = 1550$ nm for $D = 1$ mm.

In Figure 16, we consider wavelength of $\lambda = 1550$ nm and diameter of $D = 1$ mm. Comparison with measurement results at $\lambda = 850$ nm reveals that turbulence is experienced less at $\lambda = 1550$ nm. Similar to λ =1310 nm, LN has a better match with the probability density for the left tail at λ =1550 nm under the same atmospheric conditions. Our observations from Figure 7 and 4 indicate that by increasing the wavelength for the same atmospheric conditions the turbulence statistics tend to change from GG toward LN distribution.

In conclusion, we investigated the effect of wavelength on aperture averaging. We considered the three commonly used wavelengths of λ =850, 1310, and 1550 nm. Employing a custom-design atmospheric chamber, we estimated the PDF of atmospheric turbulence-induced fading channel coefficient for aperture sizes of D = 1, 3.6, and 8.7 mm under the same emulated conditions. At a fixed wavelength, the larger the aperture size is, the less it is affected by the turbulence. At the same aperture size, when we increase the wavelength, we have observed that 1310 and 1550 nm links are least affected by the turbulence and exhibit almost similar value of scintillation indices but significantly less than 850 nm. It has been also observed that the PDF tends to shift from GG toward LN distribution even for relatively small aperture sizes if the wavelength is sufficiently high. In summary, by increasing the aperture size and/or wavelength, the distribution shifts toward LN statistics.

CHAPTER III

DMT ANALYSIS UNDER LOG-NORMAL FADING CHANNEL

After characterizing the atmospheric dependency of FSO links, in Chapter 2, we dive into mitigation techniques for the major performance impairment of FSO links, i.e. turbulence induced fading. Generally speaking, fading is a significant impairment in wireless channels which results in random fluctuations in the received signal level. Multiple-input multiple-output (MIMO) communication techniques are widely employed in major wireless standards to mitigate the fading effects and offer dramatic performance improvements in terms of link reliability (via diversity gain) and data rates (via multiplexing gain). However, reaping the dual benefits of MIMO systems needs some caution because maximizing one of the gains does not necessarily maximize the other one. In fact, there is a fundamental tradeoff between multiplexing and diversity gains. Adaptive MIMO FSO systems can switch between modes of transmission which have to obey the diversity multiplexing tradeoff. Considering a MIMO FSO system, the spacetime transmission strategy can also be adjusted, introducing a new dimension for adaptation. This means that practical MIMO link adaptation algorithms must also provide a dynamic adaptation between diversity and multiplexing modes of operation which needs a fundamental understanding of DMT for FSO channel model. This fundamental tradeoff is different under different channel models. It is well-known that a common choose of channel model for FSO systems is Log-normal fading channel. The understanding of DMT under log-normal fading channels will allow us to investigate practical MIMO link adaptation algorithms for FSO links which provide a dynamic adaptation between diversity and multiplexing modes of operation.

Although there has been a growing interest on the study of diversity-multiplexing tradeoff (DMT), the existing works are mostly restricted to the outcomes reported for Rayleigh, Rician, and Nakagami fading channels. In this Chapter, we investigate the optimal tradeoff in the presence of log-normal fading which provides an accurate model for FSO, indoor wireless, optical wireless, and ultra-wideband channels. We consider a MIMO log-normal channel, derive the outage probability expression and then present the asymptotical DMT expression. It is shown that the asymptotical maximum diversity gain tends to infinity with logarithm of signal-to-noise ratio. To have further insight, we normalize the DMT with that of SISO case and express the relative asymptotical DMT of the MIMO log-normal channel as a function of the number of transmit and receive antennas. We further study DMT for finite SNRs and demonstrate convergence to the asymptotical case. Extensive numerical results are provided to corroborate the analytical derivation.

3.1 System Model and Basic Definitions

In this section, we present our system model and summarize the basic definitions for outage probability and DMT which will be used in our derivations.

3.1.1 System Model

We consider a MIMO system with M transmit and N receive antennas over a frequency-flat log-normal fading channel. Under the assumption of slow fading, we assume that the channel coefficients remain constant over a block of l symbols, i.e., l is much smaller than the channel coherence time. Let the transmitted signal and received signal, respectively, be represented by $\mathbf{x} = (x_1, x_2, \ldots, x_M)^T$, $\mathbf{x} \in \mathbb{C}^M$ and $\mathbf{y} = (y_1, y_2, \ldots, y_N)^T$, $\mathbf{y} \in \mathbb{C}^N$. The baseband signal model is then given by

$$\mathbf{y} = \sqrt{\frac{\rho}{M}}\mathbf{H}\mathbf{x} + \mathbf{w} \tag{23}$$

where ρ is the average SNR at each receive antenna and $\mathbf{w} \in \mathbb{C}^N$ is additive white Gaussian noise (AWGN) vector with i.i.d. entries $w_i \sim \mathcal{CN}(0, 1)$, $i = 1, 2, \ldots, N$. The autocorrelation matrix of noise signal is defined by $\mathbf{R}_w = E\left(\mathbf{w}\mathbf{w}^\dagger\right) = \mathbf{I}_N$. The channel matrix is denoted by $\mathbf{H} \in \mathbb{R}^{M\times N}$ whose element h_{ij} $(i = 1, 2, \ldots, N,$

$j = 1, 2, \ldots, M$) represents the channel gain between the j^{th} transmit antenna and the i^{th} receive antenna. The channel matrix elements are assumed to be i.i.d. Dropping indexes for simplicity of the presentation, the probability density function (pdf) of h is given by [47]

$$f_h(h) = \frac{1}{h\sqrt{2\pi\sigma_x^2}} \exp\left(-\frac{(\ln(h) - \mu_x)^2}{2\sigma_x^2}\right) \tag{24}$$

where μ_x and σ_x^2 are, respectively, mean and variance of $\chi = \ln(h)$ which follows Gaussian distribution. To make sure that the fading does not affect the average power level, h is normalized such that $E[h^2] = 1$. This requires the choice of $\mu_x = -\sigma_x^2$ [49]. Typical values of σ_x are within the range of 3-5 dB for indoor wireless channels [35]. Since the entries of $\mathbf{H}$ are independent, the pdf of $\mathbf{H}$ can be obtained as $p_{\mathbf{H}}(H) = \prod_{i=1}^{N}\prod_{j=1}^{M} p_{h_{ij}}(h_{ij})$. We further assume a power constraint on the transmitted signal given by $\sum_{i=1}^{M} E[|x_i|^2] \leq M$ where the expectation is with respect to the distributions of $x_i's$, $i = 1, 2, \ldots, M$, i.e., $p(\mathbf{x}) = \prod_{i=1}^{M} p(x_i)$. In this way, ρ in (23) represents the average SNR at each receiver antenna which is independent of the value of M and allows a fair comparison for different values of M. The autocorrelation matrix of input signal is defined by $\mathbf{R}_x = E\left(\mathbf{x}\mathbf{x}^{\dagger}\right)$ and, due to the power constraint, we have $\mathrm{trace}(\mathbf{R}_x) \leq M$ [100].

3.1.2 Outage Probability and DMT Definitions

Under the assumption of slow fading, the channel matrix $\mathbf{H}$ is chosen randomly according to $p_{\mathbf{H}}(H)$, but is held fixed during the block length l. Such channels are known as non-ergodic fading channels [23] and the outage probability is typically considered as the main performance metric. An outage is defined as the event that the channel does not support a target data rate, or in other words, when the instantaneous (conditioned) channel capacity, $C(\mathbf{H})$, is less than the target data rate, $R(\rho)$[1]. Therefore the outage probability is given by

$$P_{out}(R, \rho) = \Pr\{C(\mathbf{H}) < R\}. \tag{25}$$

[1]To simplify notations, we write $R(\rho)$ as R if it does not make any confusion.

Under the assumption of Gaussian noise, the MIMO channel capacity conditioned on $\mathbf{H}$ is given by [101, Ch. 8, eq. (8.15)]

$$C\left(\mathbf{H}\right) = \log\left(\left|\mathbf{I}_N + \frac{\rho}{M}\mathbf{H}\mathbf{H}^{\dagger}\right|\right). \tag{26}$$

Without loss of generality, for the rest of the thesis, we assume $M \geq N$ since exchanging M and N has no effect on the channel capacity [101]. By replacing (26) in (25) and applying eigenvalue decomposition on the resulting expression, we have

$$P_{out}\left(R, \rho\right) = \Pr\left\{\sum_{k=1}^{N} \log\left(1 + \frac{\rho}{M}\lambda_k\right) < R\right\} \tag{27}$$

where λ_k, $k = 1, 2, \ldots, N$ are real non-negative eigenvalues of $\mathbf{H}\mathbf{H}^{\dagger}$ and $0 \leq \lambda_1 \leq \lambda_2 \leq \cdots \leq \lambda_N$.

In the following we define the *asymptotical DMT* $d^*\left(r\right)$ (i.e., when SNR goes to infinity). Let r and d respectively denote multiplexing and diversity gains. At high SNRs, a diversity order $d^*\left(r\right)$ at multiplexing order r is achieved when [101, Ch. 9, eq. (9.3)]

$$r = \lim_{\rho\to\infty} \frac{R\left(\rho\right)}{\log\rho}, \tag{28}$$

$$\begin{aligned} d^*\left(r\right) &= -\lim_{\rho\to\infty} \frac{\log P_{out}\left(R, \rho\right)}{\log\rho} \\ &= -\lim_{\rho\to\infty} \frac{\partial \ln P_{out}\left(r\log\rho\right)}{\partial \ln\rho} \end{aligned} \tag{29}$$

where the second equality in (29) comes from L'Hôpital's rule. The relation in (29) is commonly represented by the exponential equality [23, 29, 30] denoted as $\doteq$, that means $P_{out}\left(R, \rho\right) \doteq \rho^{-d^*(r)}$ is identical to (29). $\dot{\geq}$ and $\dot{\leq}$ are similarly defined. The above asymptotical DMT curve $d^*\left(.\right)$ characterizes the performance limits of the slow-fading channel.

For *finite-SNR DMT*, the multiplexing and diversity gains are further defined as [24, eq. (5)]

$$r = \frac{R(\rho)}{\log(1+\rho)}, \tag{30}$$

$$\begin{aligned} d(r,\rho) &= -\frac{\partial \log P_{out}(R,\rho)}{\partial \log \rho} \\ &= -\frac{\rho}{P_{out}(R,\rho)} \frac{\partial P_{out}(R,\rho)}{\partial \rho}. \end{aligned} \tag{31}$$

It can be easily checked that the definition of DMT at finite-SNR converges to that of the asymptotical DMT at high SNRs for $\rho \to \infty$, that is, $\lim_{\rho\to\infty} d(r,\rho) = d^*(r)$.

We also introduce the so-called *relative asymptotical DMT*, $\hat{d}^*(r)$ as

$$\begin{aligned} \hat{d}^*(r) &= \frac{d^*(r)}{d^*_{SISO}(0)} \\ &= \lim_{\rho\to\infty} \frac{(\partial \ln P_{out}(r\log\rho)/\partial \ln \rho\,)}{(\partial \ln P_{out}^{SISO}(r\log\rho)/\partial \ln \rho\,)|_{r=0}} \end{aligned} \tag{32}$$

where asymptotical DMT is normalized with respect to asymptotical DMT of SISO case evaluated at $r = 0$. Similarly, we normalize the finite-SNR DMT with the SISO case and obtain the *relative finite-SNR DMT* as $\hat{d}(r,\rho) = d(r,\rho)/d^*_{SISO}(0)$.

3.2 DMT Derivations

In this section, we derive the asymptotical and finite-SNR DMTs for MIMO systems over log-normal fading channels.

3.2.1 Analytical DMT Analysis

In this subsection, we present closed form expressions for asymptotical DMT of MIMO systems and finite-SNR DMT of MISO/SIMO systems.

Asymptotical DMT of MIMO Systems: We consider the data rate of $R = r\log(\rho)$ for $0 \le r \le N$ since the maximum number of degrees of freedom is equal to $\min\{M,N\}$. Without loss of generality, we assume $M \ge N$. The outage probability in (27) for MIMO case can be found using the joint pdf of ordered eigenvalues (i.e., $0 \le \lambda_1 \le \lambda_2 \le \cdots \le \lambda_N$). To the best of our knowledge, there is no closed form expression for the joint pdf of λ_k's where elements of the channel matrix $\mathbf{H}$ are log-normally distributed. The joint pdf of λ_k's is given by [29]

$$\begin{aligned} p_{\mathbf{\Lambda}}(\Lambda) =& \frac{1}{(4\pi)^N}\left(\prod_{i=1}^{N}\lambda_i^{M-N}\right)\cdot\prod_{i<j}(\lambda_i-\lambda_j)^2 \\ &\times \int\limits_{V_{N,N}}\int\limits_{V_{N,M}} p_{\mathbf{H}}\left(U\Lambda^{1/2}Q\right) dQdU \end{aligned} \tag{33}$$

where $\Lambda = diag\{\lambda_1, \lambda_2, \ldots, \lambda_N\}$, $V_{N,N}$ and $V_{N,M}$ are Stiefel manifolds and Q, U are unitary matrices in singular value decomposition (SVD) of the matrix $\mathbf{H}$. Following the same procedure in [23], we define $\alpha_k = -\log\lambda_k/\log\rho$ and hence we have $\lambda_k = \rho^{-\alpha_k}$ for $k = 1, 2, \ldots, N$.

For high SNRs, we have $(1+\rho\lambda_k/M) \doteq \rho^{(1-\alpha_k)^+}$ [23, Lemma 3] and the outage probability in (27) can be therefore written as

$$\begin{aligned} P_{out}(r\log\rho) &\doteq \Pr\left\{\sum_{k=1}^{N}\log\left(\rho^{(1-\alpha_k)^+}\right) < \log\rho^r\right\} \\ &= \Pr\left\{\sum_{k=1}^{N}(1-\alpha_k)^+ < r\right\} \end{aligned} \tag{34}$$

where α_k's show the level of singularity of matrix $\mathbf{H}$. The joint pdf of α_k's can be found by change of variables (i.e., $\lambda_k = \rho^{-\alpha_k}$) in (33) which is given as [29]

$$\begin{aligned} p_{\alpha}(\alpha) =& \left(\frac{\log\rho}{4\pi}\right)^N\left(\prod_{i=1}^{N}\rho^{-(M-N+1)\alpha_i}\right) \\ &\times\prod_{i<j}\left(\rho^{-\alpha_i}-\rho^{-\alpha_j}\right)^2 \\ &\times\int\limits_{V_{N,N}}\int\limits_{V_{N,M}} p_{\mathbf{H}}(UDQ)\, dQdU \end{aligned} \tag{35}$$

where $D = diag\left\{\rho^{-\alpha_1/2}, \ldots, \rho^{-\alpha_N/2}\right\}$. Therefore, we can write (34) as

$$\begin{aligned} P_{out}(r\log\rho) \doteq& \int\limits_{\mathcal{A}(r)}\left(\frac{\log\rho}{4\pi}\right)^N\left(\prod_{i=1}^{N}\rho^{-(M-N+1)\alpha_i}\right) \\ &\times\prod_{i<j}\left(\rho^{-\alpha_i}-\rho^{-\alpha_j}\right)^2 \\ &\times\left[\int\limits_{V_{N,N}}\int\limits_{V_{N,M}} p_{\mathbf{H}}(UDQ)\, dQdU\right] d\alpha \end{aligned} \tag{36}$$

where the set $\mathcal{A}(r) = \{\alpha : \ \alpha_1 \geq \alpha_2 \geq \cdots \geq \alpha_N, \ \sum_k (1-\alpha_k)^+ < r\}$ denotes the outage event.

Since we are only interested in the SNR exponent of $\lim\limits_{\rho\to\infty} \log P_{out}(r\log\rho)/\log\rho$, we can simplify the integral in (36). First, the term $(\log\rho/4\pi)^N$ has no effect on SNR exponent, since $\lim\limits_{\rho\to\infty} \log[(\log\rho/4\pi)^N]/\log\rho \to 0$. Second, we have $(\rho^{-\alpha_i} - \rho^{-\alpha_j})^2 \doteq \rho^{-2\alpha_j}$ for any $j > i$ where $\alpha_j < \alpha_i$ [23, Lemma 3]. Therefore, the outage probability in (36) reduces to

$$P_{out}(r\log\rho) \doteq \int\limits_{\mathcal{A}(r)} \rho^{-\sum_{i=1}^{N}(M-N+2i-1)\alpha_i} \times \left[\int\limits_{V_{N,N}}\int\limits_{V_{N,M}} p_{\mathbf{H}}(UDQ)\, dQdU\right] d\alpha. \tag{37}$$

Next, we need to find the SNR exponent of $\tau(\rho) = \int_{V_{N,N}}\int_{V_{N,M}} p_{\mathbf{H}}(UDQ)\, dQdU$ in (37) where $p_{\mathbf{H}}(H) = \prod_{i=1}^{N}\prod_{j=1}^{M} p_{h_{ij}}(h_{ij})$. Replacing (24) in $p_{\mathbf{H}}(H)$, we have

$$p_{\mathbf{H}}(H) = \frac{1}{(2\pi\sigma_x^2)^{MN/2}} \cdot \frac{1}{\prod\limits_{i=1}^{N}\prod\limits_{j=1}^{M} h_{ij}} \times \exp\left(-\frac{1}{2\sigma_x^2}\sum_{i=1}^{N}\sum_{j=1}^{M}(\ln(h_{ij}) - \mu_x)^2\right). \tag{38}$$

To investigate the SNR exponent of the term $\tau(\rho)$, one can notice that $h_{ij} = [UDQ]_{ij}$ and it is a polynomial expression of ρ where the coefficients are functions of U and Q. At high SNR values where $\rho\to\infty$, we can write $h_{ij} \doteq \rho^{-\alpha_N/2}$ which denotes the term with the highest order. The term $1/(2\pi\sigma_x^2)^{MN/2}$ in (38) can be also ignored because it has no effect on SNR exponent. Therefore, we can write

$$\begin{aligned} &\int_{V_{N,N}}\int_{V_{N,M}} p_{\mathbf{H}}(UDQ)\, dQdU \\ &\doteq \rho^{MN\alpha_N/2} \exp\left(-\frac{MN}{2\sigma_x^2}\left(\frac{\alpha_N}{2}\ln(\rho) + \mu_x\right)^2\right) \\ &= \rho^{\left[\frac{MN\alpha_N}{2} - \frac{MN}{2\sigma_x^2}\left(\frac{\alpha_N^2}{4}\ln(\rho) + \frac{\mu_x^2}{\ln(\rho)} + \alpha_N\mu_x\right)\right]}. \end{aligned} \tag{39}$$

By replacing (39) in (37) and using $\mu_x = -\sigma_x^2$, we obtain

$$P_{out}(r\log\rho) \doteq \int\limits_{\mathcal{A}(r)} \rho^{-\sum_{i=1}^{N}(M-N+2i-1)\alpha_i + \left[\frac{MN\alpha_N}{2} - \frac{MN}{2\sigma_x^2}\left(\frac{\alpha_N^2}{4}\ln(\rho) + \frac{\mu_x^2}{\ln(\rho)} - \alpha_N\sigma_x^2\right)\right]} d\alpha \tag{40}$$

It can be easily shown that the integral in (40) is dominated with the largest ρ exponent when $\rho \to \infty$, and hence the SNR exponent of P_{out} can be written as

$$P_{out}\left(r\log\rho\right) \doteq \rho^{-\inf\limits_{\alpha\in\mathcal{A}(r)}\left\{\sum_{i=1}^{N}\left(M-N+2i-1\right)\alpha_i-\frac{MN\alpha_N}{2}+\frac{MN}{2\sigma_x^2}\left(\frac{\alpha_N^2}{4}\ln(\rho)+\frac{\mu_x^2}{\ln(\rho)}-\alpha_N\sigma_x^2\right)\right\}} \quad (41)$$

Using (29), the optimal DMT curve for MIMO log-normal fading channels is obtained as

$$\begin{aligned} d^*\left(r\right) = \inf_{\alpha\in\mathcal{A}(r)}\Big\{\sum\nolimits_{i=1}^{N}\left(M-N+2i-1\right)\alpha_i \\ -MN\alpha_N + \frac{MN\alpha_N^2}{4\sigma_x^2}\ln\left(\rho\right)\Big\} \end{aligned} \quad (42)$$

where $\mathcal{A}\left(r\right)=\left\{\alpha:\ \alpha_1\geq\alpha_2\geq\cdots\geq\alpha_N,\ \sum_k\left(1-\alpha_k\right)^+<r\right\}$. Furthermore, (42) can be reduced to a mix of quadratic and the piecewise linear function given as

$$d^*\left(r\right)=\begin{cases} MN(1-r)^2\frac{\ln(\rho)}{4\sigma_x^2}+\left(M-1\right)\left(N-1\right) & 0\leq r<1 \\ \left(M-r\right)\left(N-r\right) & 1\leq r\leq N \end{cases} \quad (43)$$

It can be observed from (43) that for the case of $1\leq r\leq N$, the DMT coincides with the DMT of MIMO Rayleigh fading channels. For $0\leq r<1$, (43) indicates that the diversity gain tends to infinity when SNR goes to infinity.

Infinite diversity gains for log-normal channels were also reported in [49, 51, 102, 103]. To deal with such cases and have some further insights into channel limits, relative asymptotical DMT given by (32) can be used. This yields

$$\hat{d}^*\left(r\right)=\begin{cases} MN(1-r)^2 & 0\leq r\leq 1 \\ 0 & otherwise \end{cases} \quad (44)$$

which shows MN-fold increase in diversity gain.

Finite-SNR DMT of MISO/SIMO Systems: A closed form expression for finite-SNR DMT of MIMO systems is unfortunately not available. Therefore, we consider MISO/SIMO systems as special cases and obtain closed-form expressions for finite-SNR DMT. For a MISO system, we replace $N=1$ in (27) and set the data rate of $R=r\log\left(1+\rho\right)$ for $0\leq r\leq 1$. The outage probability is then given by

$$P_{out}\left(r,\rho\right) = \Pr\left\{\log\left(1+\frac{\rho}{M}\sum_{j=1}^{M}h_j^2\right) < r\log\left(1+\rho\right)\right\}$$
$$= \Pr\left\{\sum_{j=1}^{M}h_j^2 < \frac{\left(1+\rho\right)^r-1}{\rho/M}\right\}. \tag{45}$$

The summation $\sum_{j=1}^{M}h_j^2$ in (45) is the sum of M i.i.d. log-normal RVs which can be well approximated as a single log-normal RV as e^z with mean μ_z and variance of σ_z^2 [104,105]. As discussed in the Appendix, for $\sigma_x < 4$ dB, we use Fenton-Wilkinson's approach [104] with $\sigma_z^2 = \ln\left(1+\left(e^{4\sigma_x^2}-1\right)/M\right)$ and $\mu_z = \ln\left(M\right) - \sigma_z^2/2$. On the other hand, for $\sigma_x > 4$, we use MGF-based approach [105] where μ_z and σ_z^2 are estimated (see Appendix). We write the outage probability expression as

$$P_{out}\left(r,\rho\right) \cong \Pr\left\{z < \ln\left(\frac{\left(1+\rho\right)^r-1}{\rho/M}\right)\right\}$$
$$= Q\left(\left[\ln\left(\frac{\rho/M}{\left(1+\rho\right)^r-1}\right)+\mu_z\right]/\sigma_z\right). \tag{46}$$

Replacing (46) in (31) and using Leibniz rule to perform the differentiation of Q function, we obtain the finite-SNR DMT for MISO system as

$$d\left(r,\rho\right) = \frac{1}{\sigma_z}\left[1-\frac{r\rho(1+\rho)^{r-1}}{\left(1+\rho\right)^r-1}\right] \times \frac{\exp\left(-\left[A_z\left(r,\rho\right)\right]^2/2\right)}{\sqrt{2\pi}Q\left(A_z\left(r,\rho\right)\right)}$$
$$A_z\left(r,\rho\right) = \left[\ln\left(\frac{\rho/M}{\left(1+\rho\right)^r-1}\right)+\mu_z\right]/\sigma_z. \tag{47}$$

It can be noted that M and N are interchangeable in (26), i.e.,

$$\log\left(\left|\mathbf{I}_N + \frac{\rho}{M}\mathbf{H}\mathbf{H}^\dagger\right|\right) = \log\left(\left|\mathbf{I}_M + \frac{\rho}{M}\mathbf{H}^\dagger\mathbf{H}\right|\right). \tag{48}$$

Therefore, the result in (47) is also valid for SIMO system where M is replaced by N.

For $\rho \to \infty$, it can be shown that (47) converges to $\left(1-r\right)^2\ln\rho/\sigma_z^2$. It can be readily checked that this coincides with (43) for $N = 1$ and small values of σ_x. Normalizing the finite-SNR DMT with the SISO scheme, we can obtain the *relative finite-SNR DMT* as

$$\hat{d}\left(r,\rho\right) = d\left(r,\rho\right)/[\ln\rho/4\sigma_x^2]. \tag{49}$$

3.2.2 Numerical DMT Analysis

As mentioned in the previous subsection, derivation of a closed form expression for finite-SNR DMT of MIMO systems is intractable. In this subsection, we use numerical methods to evaluate the finite-SNR DMT of MIMO systems.

Finite-SNR DMT of MIMO Systems: For finite-SNR DMT derivation, we use the outage probability definition in (27) and consider the data rate of $R = r \log(1+\rho)$ for $0 \leq r \leq N$. To derive the outage probability, we will approximate the joint pdf of λ_k's in (27) with a log-normal distribution. This can be readily checked from $\Lambda = U^{\dagger} H H^{\dagger} U$ in which λ_k's are some polynomials of h_{ij}'s. Therefore each λ_k can be considered as a sum of log-normal RVs where it can be considered as a log-normally distributed RV (see Appendix A). Noting that λ_k's are correlated log-normal RVs, we use a modified version of MGF-based approach in [105] since it provides an accurate approximation for the sum of correlated log-normal RVs. In this approach, we match the MGFs based on the trace equality

$$\sum_{i=1}^{N} \lambda_i = \sum_{i=1}^{N} \sum_{j=1}^{M} h_{ij}^2. \tag{50}$$

The Gauss-Hermite representation of the MGF for right hand side of (50) can be expressed as

$$\begin{aligned}
&\prod_{j=1}^{MN} \hat{\Psi}_{h_{ij}^2}(s_k; 2\mu_x, 2\sigma_x) \\
&= \prod_{j=1}^{MN} \sum_{n=1}^{K} \frac{w_n}{\sqrt{\pi}} \exp\left[-s_k \exp\left(2\sqrt{2}\sigma_x a_n + 2\mu_x\right)\right].
\end{aligned} \tag{51}$$

The left hand side of (50) is a sum of correlated log-normal RVs. The corresponding Gaussian RVs, i.e., $u_i = \ln(\lambda_i)$ follow the joint distribution

$$p_{\mathbf{u}}(\mathbf{u}) = \frac{1}{(2\pi)^{N/2} |\mathbf{C}|^{1/2}} \exp\left(-\frac{(\mathbf{u}-\boldsymbol{\mu})^{\dagger} \mathbf{C}^{-1} (\mathbf{u}-\boldsymbol{\mu})}{2}\right) \tag{52}$$

where $\mathbf{C}$ is covariance matrix and $\boldsymbol{\mu}$ is vector of means of the Gaussian RVs. Let $\mathbf{C}_{sq}$ denote the square root of $\mathbf{C}$, i.e., $\mathbf{C} = \mathbf{C}_{sq} \mathbf{C}_{sq}^{\dagger}$. Here, c'_{ij} denotes the $(i, j)^{th}$

element of $\mathbf{C}_{sq}$. The MGF function of $\sum_{i=1}^{N} \lambda_i$ is given by [105, eq. (17)]

$$\hat{\Psi}^{(c)}_{\left(\sum_{i=1}^{N} \lambda_i\right)}(s_k; \boldsymbol{\mu}, \mathbf{C}) = \sum_{n_1=1}^{K} \cdots \sum_{n_N=1}^{K} \left[\prod_{i=1}^{N} \frac{w_{n_i}}{\sqrt{\pi}}\right] \times \exp\left(-s_k \sum_{i=1}^{N} \left[\exp\left(\sqrt{2} \sum_{j=1}^{N} c'_{ij} a_{n_j} + \mu_i\right)\right]\right). \quad (53)$$

To find $\mathbf{C}$ and $\boldsymbol{\mu}$, we should solve the following system of equations

$$\hat{\Psi}^{(c)}_{\left(\sum_{i=1}^{N} \lambda_i\right)}(s_k; \boldsymbol{\mu}, \mathbf{C}) = \prod_{j=1}^{MN} \hat{\Psi}_{h_{ij}^2}(s_k; 2\mu_x, 2\sigma_x) \quad (54)$$

$$\text{for} \quad k = 1, 2, ..., N(N+1)$$

where $\prod_{j=1}^{MN} \hat{\Psi}_{h_{ij}^2}(s_k; 2\mu_x, 2\sigma_x)$ and $\hat{\Psi}^{(c)}_{\sum_{i=1}^{N} \lambda_i}(s_k; \boldsymbol{\mu}, \mathbf{C})$ are respectively given by (51) and (53). It has been found that $K = 12$ is sufficient to accurately determine the unknown values [105] and the values of s_k are optimized to reduce the mean absolute error accuracy metric (see Appendix A).

The approximated joint pdf of λ_k's can be then written as

$$p_{\boldsymbol{\Lambda}}(\Lambda) = \frac{1}{(2\pi)^{N/2} |\mathbf{C}|^{1/2} \prod_{k=1}^{N} \lambda_k} \times \exp\left(-\frac{(\ln(\Lambda) - \boldsymbol{\mu})^{\dagger} \mathbf{C}^{-1} (\ln(\Lambda) - \boldsymbol{\mu})}{2}\right) \quad (55)$$

Let us denote the mutual information expression within (27) by

$$I = \sum_{k=1}^{N} \log\left(1 + \frac{\rho}{M} \lambda_k\right) = \sum_{k=1}^{N} \beta_k \quad (56)$$

where $\beta_k = \log(1 + \lambda_k(\rho/M))$. Using the change of variable rule in [100], we find the joint distribution of β_k's in (57)

$$p_{\beta}(\beta) = \frac{\exp\left(\sum_{k=1}^{N} \beta_k\right)}{(2\pi)^{N/2} |\mathbf{C}|^{1/2} \prod_{k=1}^{N} (\exp(\beta_k) - 1)} \times \exp\left(-\frac{(\ln(\mathbf{B}) - \mu + \ln(M/\rho))^{\dagger} \mathbf{C}^{-1} (\ln(\mathbf{B}) - \mu + \ln(M/\rho))}{2}\right) \quad (57)$$

in which $\mathbf{B} = diag\left\{\left(\exp\left(\beta_1\right)-1\right),...,\left(\exp\left(\beta_N\right)-1\right)\right\}$. Using (57), the outage probability can be found by performing the following integral

$$P_{out}\left(R,\rho\right) = \int\limits_{\mathcal{B}(r)} p_{\boldsymbol{\beta}}\left(\beta\right) d\boldsymbol{\beta} \tag{58}$$

where $\mathcal{B}\left(r\right) = \left\{\beta : \sum_{k=1}^{N} \beta_k < r\log\left(1+\rho\right)\right\}$.

The integration in (58) is difficult to be followed mathematically for the general case. In the following, we consider a special case where some further simplifications can be made.

Special case 1: As a special case, we assume a MIMO system with $M = N = 2$. In this case, there exist only two eigenvalues λ_1 and λ_2 with the corresponding RVs β_1 and β_2. From (56), we have $I = \beta_1 + \beta_2$. The joint distribution of β_1 and β_2 can be written from (57) as

$$\begin{aligned} p\left(\beta_1,\beta_2\right) = & \frac{\exp\left(\beta_1+\beta_2\right)}{2\pi\sigma_1\sigma_2\sqrt{1-c^2}\left(\exp\left(\beta_1+\beta_2\right)-\exp\left(\beta_1\right)-\exp\left(\beta_2\right)+1\right)} \exp\left(\frac{-1}{2\left(1-c^2\right)}\right. \\ & \times\left[\frac{\left(\ln\left(\exp\left(\beta_1\right)-1\right)-\mu_1+\ln\left(M/\rho\right)\right)^2}{\sigma_1^2} + \frac{\left(\ln\left(\exp\left(\beta_2\right)-1\right)-\mu_2+\ln\left(M/\rho\right)\right)^2}{\sigma_2^2}\right. \\ & \left.\left. - \frac{2c\left(\ln\left(\exp\left(\beta_1\right)-1\right)-\mu_1+\ln\left(M/\rho\right)\right)\left(\ln\left(\exp\left(\beta_2\right)-1\right)-\mu_2+\ln\left(M/\rho\right)\right)}{\sigma_1\sigma_2}\right]\right) \end{aligned} \tag{59}$$

where c is the correlation between β_1 and β_2. The joint pdf of I and β_2 is given as

$$\begin{aligned} p\left(I,\beta_2\right) = & \frac{\exp\left(I\right)}{2\pi\sigma_1\sigma_2\sqrt{1-c^2}\left(\exp\left(I\right)-\exp\left(I-\beta_2\right)-\exp\left(\beta_2\right)+1\right)} \exp\left(-\frac{1}{2\left(1-c^2\right)}\right. \\ & \times\left[\frac{\left(\ln\left(\exp\left(I-\beta_2\right)-1\right)-\mu_1+\ln\left(M/\rho\right)\right)^2}{\sigma_1^2} + \frac{\left(\ln\left(\exp\left(\beta_2\right)-1\right)-\mu_2+\ln\left(M/\rho\right)\right)^2}{\sigma_2^2}\right. \\ & \left.\left. - \frac{2c\left(\ln\left(\exp\left(I-\beta_2\right)-1\right)-\mu_1+\ln\left(M/\rho\right)\right)\left(\ln\left(\exp\left(\beta_2\right)-1\right)-\mu_2+\ln\left(M/\rho\right)\right)}{\sigma_1\sigma_2}\right]\right) \end{aligned} \tag{60}$$

Taking integration of (60) with respect to β_2, it can be found that

$$p\left(I,\rho\right) = \frac{\exp\left(I\right)}{2\pi\sigma_1\sigma_2\sqrt{1-c^2}} \int\limits_0^{I/2} g\left(\beta_2, I, \rho\right) d\beta_2 \tag{61}$$

where $g\left(\beta_2, I, \rho\right)$ is expressed by

$$g\left(\beta_2, I, \rho\right) = \frac{1}{\left(\exp\left(I\right) - \exp\left(I-\beta_2\right) - \exp\left(\beta_2\right) + 1\right)} \exp\left(-\frac{1}{2\left(1-c^2\right)}\right.$$
$$\times \left[\frac{\left(\ln\left(\exp\left(I-\beta_2\right)-1\right) - \mu_1 + \ln\left(M/\rho\right)\right)^2}{\sigma_1^2} + \frac{\left(\ln\left(\exp\left(\beta_2\right)-1\right) - \mu_2 + \ln\left(M/\rho\right)\right)^2}{\sigma_2^2}\right.$$
$$\left.\left.-\frac{2c\left(\ln\left(\exp\left(I-\beta_2\right)-1\right) - \mu_1 + \ln\left(M/\rho\right)\right)\left(\ln\left(\exp\left(\beta_2\right)-1\right) - \mu_2 + \ln\left(M/\rho\right)\right)}{\sigma_1\sigma_2}\right]\right) \tag{62}$$

The integration $\int_0^{I/2} g\left(\beta_2, I, \rho\right) d\beta_2$ can be calculated numerically for each value of ρ and I. The outage probability for each r and ρ can be computed by

$$P_{out}\left(r, \rho\right) = \Pr\left\{I < r\log\left(1+\rho\right)\right\} = \tag{63}$$
$$\frac{1}{2\pi\sigma_1\sigma_2\sqrt{1-c^2}} \int_0^{r\log(1+\rho)} \exp\left(I\right)\left(\int_0^{I/2} g\left(\beta_2, I, \rho\right) d\beta_2\right) dI.$$

Using the Leibniz integral rule [100], $\partial P_{out}\left(r, \rho\right)/\partial\rho$ can be further obtained as

$$\frac{\partial P_{out}\left(r, \rho\right)}{\partial\rho} = \frac{1}{2\pi\sigma_1\sigma_2\sqrt{1-c^2}}\left[\frac{r}{1+\rho}\exp\left(r\log\left(1+\rho\right)\right)\right.$$
$$\times\left(\int_0^{r\log(1+\rho)/2} g\left(\beta_2, r\log\left(1+\rho\right), \rho\right) d\beta_2\right)$$
$$\left.+\int_0^{r\log(1+\rho)} \exp\left(I\right) \times \left(\int_0^{I/2} \frac{\partial g\left(\beta_2, I, \rho\right)}{\partial\rho} d\beta_2\right) dI\right] \tag{64}$$

where $\partial g\left(\beta_2, I, \rho\right)/\partial\rho$ is given as

$$\frac{\partial g\left(\beta_2, I, \rho\right)}{\partial\rho} = \frac{g\left(\beta_2, I, \rho\right)}{\left(1-c^2\right)\rho} \cdot \left[\frac{\left(\ln\left(\exp\left(I-\beta_2\right)-1\right) - \mu_1 + \ln\left(M/\rho\right)\right)}{\sigma_1^2}\right.$$
$$+\frac{\left(\ln\left(\exp\left(\beta_2\right)-1\right) - \mu_2 + \ln\left(M/\rho\right)\right)}{\sigma_2^2}$$
$$\left.-\frac{c\left(\ln\left(\exp\left(I\right) - \exp\left(I-\beta_2\right) - \exp\left(\beta_2\right) + 1\right) - \mu_1 - \mu_2 + 2\ln\left(M/\rho\right)\right)}{\sigma_1\sigma_2}\right] \tag{65}$$

The integrals in above expressions can be computed using numerical methods. After obtaining $P_{out}\left(r, \rho\right)$ from (63) and $\partial P_{out}\left(r, \rho\right)/\partial\rho$ from (64), the relative finite-SNR DMT can be obtained using (31).

Special case 2: As another special case, we consider multiple-input single-output (MISO) systems and obtain closed-form expressions for finite-SNR DMT. We replace $N = 1$ in (27) and set the data rate of $R = r\log(1+\rho)$ for $0 \le r \le 1$. The outage probability is then given by

$$\begin{aligned} P_{out}(r,\rho) &= \Pr\left\{\log\left(1+\frac{\rho}{M}\sum_{j=1}^{M}h_j^2\right) < r\log(1+\rho)\right\} \\ &= \Pr\left\{\sum_{j=1}^{M}h_j^2 < \frac{(1+\rho)^r-1}{\rho/M}\right\} \end{aligned} \tag{66}$$

The summation $\sum_{j=1}^{M} h_j^2$ in (66) is the sum of M i.i.d. log-normal RVs which can be well approximated as a single log-normal RV as e^z with mean μ_z and variance of σ_z^2 [104, 105]. As discussed in the Appendix, for $\sigma_x < 4$ dB, we can use Fenton-Wilkinson's approach [104] with $\sigma_z^2 = \ln\left(1+\left(e^{4\sigma_x^2}-1\right)/M\right)$ and $\mu_z = \ln(M) - \sigma_z^2/2$. On the other hand, for $\sigma_x > 4$, we use MGF-based approach [105] where μ_z and σ_z^2 are estimated (see Appendix A). We write the outage probability expression as

$$\begin{aligned} P_{out}(r,\rho) &\cong \Pr\left\{z < \ln\left(\frac{(1+\rho)^r-1}{\rho/M}\right)\right\} \\ &= Q\left(\left[\ln\left(\frac{\rho/M}{(1+\rho)^r-1}\right)+\mu_z\right]/\sigma_z\right). \end{aligned} \tag{67}$$

Replacing (67) in (31) and using Leibniz rule to perform the differentiation of Q function, we obtain the finite-SNR DMT for MISO system as

$$\begin{aligned} d(r,\rho) &= \frac{1}{\sigma_z}\left[1-\frac{r\rho(1+\rho)^{r-1}}{(1+\rho)^r-1}\right] \times \frac{\exp\left(-[A_z(r,\rho)]^2/2\right)/\sqrt{2\pi}}{Q(A_z(r,\rho))} \\ A_z(r,\rho) &= \left[\ln\left(\frac{\rho/M}{(1+\rho)^r-1}\right)+\mu_z\right]/\sigma_z \end{aligned} \tag{68}$$

It can be noted that M and N are interchangeable, i.e.,

$$\log\left(\left|\mathbf{I}_N+\frac{\rho}{M}\mathbf{H}\mathbf{H}^\dagger\right|\right) = \log\left(\left|\mathbf{I}_M+\frac{\rho}{M}\mathbf{H}^\dagger\mathbf{H}\right|\right). \tag{69}$$

Therefore, the result in (68) is also valid for MISO systems where M is replaced by N.

For $\rho \to \infty$, it can be shown that (68) converges to $(1-r)^2 \ln \rho/\sigma_z^2$. It can be readily checked that this coincides with (43) for $N = 1$. Normalizing the finite-SNR DMT with the SISO scheme, we can obtain the *relative finite-SNR DMT* as

$$\hat{d}(r,\rho) = d(r,\rho)/[\ln \rho/4\sigma_x^2] \tag{70}$$

3.3 DMT Performance Evaluation

We first consider a SISO system which is used as a benchmark for this work. By replacing $M = N = 1$ in (44) and (49), we obtain the relative asymptotical DMT and relative finite-SNR DMT curves for the SISO system, respectively. We assume $\sigma_x^2 = 3$ dB and plot DMT curves for SISO system in Fig. 17. As expected, it is observed that as SNR increases, the relative finite-SNR DMT curves tend to the relative asymptotical DMT curve of the channel. As discussed earlier, in log-normal fading channels, infinite diversity gain is achieved at extreme point of $r = 0$. This could be observed in the zoomed part of Fig. 17, which shows that the finite-SNR curves go to very big values as $r \to 0$.

In an attempt to compare the optimal DMT curve with the performance of some well-known modulation schemes, the tradeoff curves for PAM and QAM are depicted in Fig. 18. The error probability of PAM and QAM is given by $P_e(\rho,r) = \int_0^\infty Q\left(\sqrt{2D_{\min}^2 h^2}\right) f_h(h)\,dh$. Assuming a data rate of R bits/s/Hz and considering that there are 2^R and $2^{R/2}$ constellation points for PAM and QAM respectively, the infimum distances are approximated as $D_{\min} \approx \sqrt{SNR}/2^R$ for PAM and $D_{\min} \approx \sqrt{SNR}/2^{R/2}$ for QAM [101, Ch. 9]. The asymptotical DMT for PAM and QAM is then found by inserting the above integral in (29) and is plotted for high SNRs. The value $\hat{d}^*(0)$ is interpreted as the decreasing rate of error probability with SNR exponent for a fixed data rate which describes conventional diversity gain of a scheme. For SISO system, this value is 1 for QAM and PAM, as expected. Another extreme point is $\hat{d}^*(r_{\max}) = 0$ where $r_{\max}$ describes increment of the data rate with respect to SNR considering a fixed error probability. $r_{\max}$

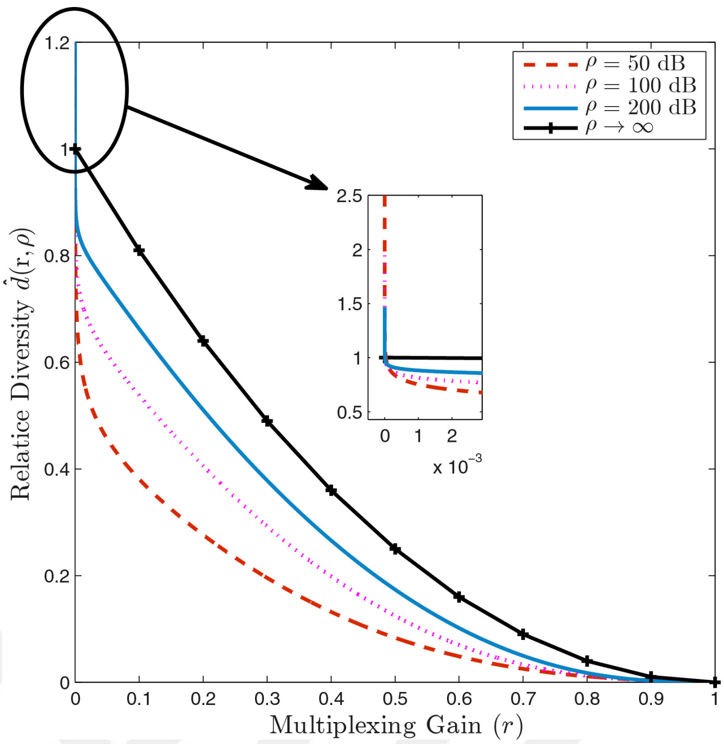

Figure 17: Relative asymptotical DMT curves of SISO system over log-normal fading channel.

is 1 for QAM and optimal DMT curve, but reduces to 0.6 for PAM. The other values in between two end points show the possibility of extracting diversity and multiplexing gain according to the tradeoff curve. The above discussion makes sense due to the fact that PAM uses half degree of freedom (real dimension) and QAM uses full degree of freedom (real and imaginary dimensions). As it is depicted in Fig. 18, the curve of QAM achieves the optimal DMT curve.

In Fig. 19, we demonstrate the relative asymptotical DMT curves of the MIMO log-normal fading channels using (44). First, we compare the cases of $M = N = 2$, $M = 3$, $N = 2$ and $M = N = 3$. It can be observed that MN-fold increase in diversity is achieved for all of the cases, however, for $r > 1$ no improvement is observed and the diversity gains are so small. This means that at high SNR values, multiplexing gains are achievable at the price of very low diversity gains. This can also be demonstrated from (42). When SNR goes to infinity, the first and second terms in (42) will be negligible and the remaining term after applying normalization (i.e. $\inf\{MN\alpha_N^2\}$) is equal to $MN\left(1 - r^2\right)$ for $0 \leq r \leq 1$ and

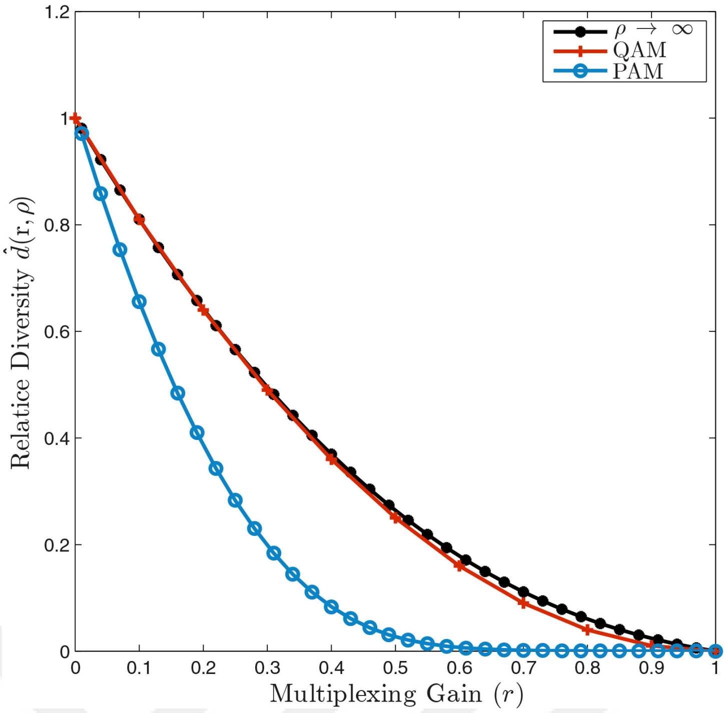

Figure 18: Comparison of the performance of modulation schemes with the optimal DMT curve.

zero for $1 \leq r \leq N$. This discussion is based on the definition of relative DMT curve where the diversity is normalized by SISO benchmark. It should not be misunderstood that the diversity gain will be zero for $r > 1$. The conventional (i.e., unnormalized) asymptotical DMT curves obtained through (43) are also depicted as an inset to clarify the above statement. All of the three curves show quadratic behavior for $0 \leq r \leq 1$ and tend to infinity when $r \to 0$. However, they have the piecewise linear behavior for $r > 1$ as $(M - r)(N - r)$. Specifically, for the case of $M = N = 3$, the diversity gains of 4 and 1 are achieved for $r = 1$ and $r = 2$, respectively. For the cases of $M = N = 2$ and $M = 3,\ N = 2$, the diversity gains of 1 and 2 are achieved for $r = 1$, respectively.

In Fig. 20, we investigate the effect of number of the antennas and channel variance on relative finite-SNR DMT for a MISO system using (49). Particularly, we consider $M = 2,\ 4,\ 6$ and consider two cases of $\sigma_x = 3$ and 4 dB. As a benchmark, the performance of SISO system is also depicted in the figure. For each case, we depict the relative finite-SNR DMT curve at SNR $= 20$ dB. It is

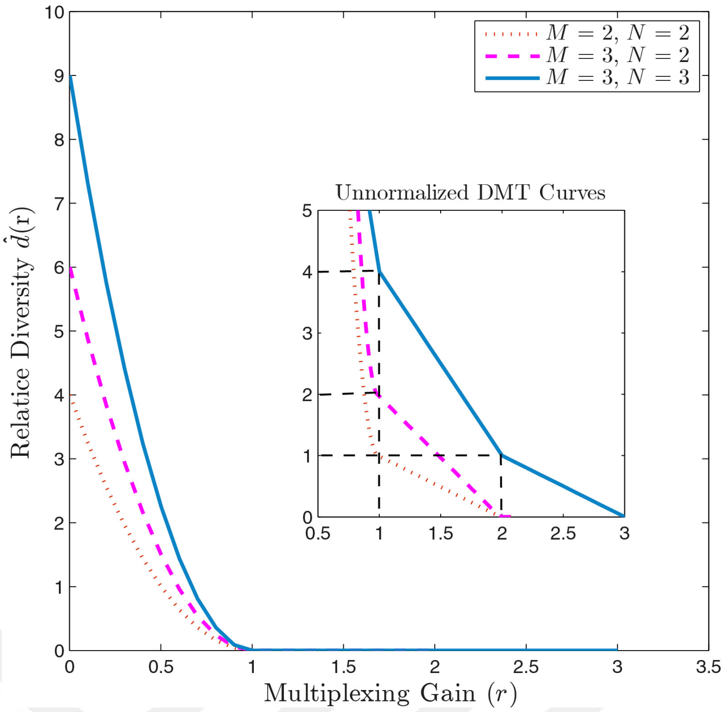

Figure 19: Relative asymptotical DMT curves of the MIMO system over log-normal fading channel.

observed that when M increases from 1 to 6 there is an increase in diversity gain at all multiplexing gains. Specifically, for $\sigma_x = 3$ dB and SNR $= 20$ dB the relative diversity gain at $r = 0.1$ increases from 0.25 to 0.29, 0.32, and 0.34 for $M = 1$, 2, 4 and 6 respectively. It is observed that this increase in maximum diversity gain is much more pronounced when σ_x is small or SNR is high. This reveals that -fold increase in diversity gain for log-normal channel is possible when SNR is high and/or σ_x is small. In other words, the fading strength in log-normal channels has an intense effect on the achievable diversity order. This can be shown by using the relative asymptotical DMT curve of MISO system for sufficiently small values of σ_x as

$$\begin{aligned}\hat{d}^*(r) &= \frac{(1-r)^2 \ln \rho/\sigma_z^2}{\ln \rho/4\sigma_x^2} \\ &= (1-r)^2 \frac{4\sigma_x^2}{\ln\left(1+\left(e^{4\sigma_x^2}-1\right)/M\right)} \\ &\simeq (1-r)^2 \frac{4\sigma_x^2}{\ln\left(1+4\sigma_x^2/M\right)} \\ &\simeq (1-r)^2 \frac{4\sigma_x^2}{4\sigma_x^2/M} \\ &= M(1-r)^2\end{aligned} \tag{71}$$

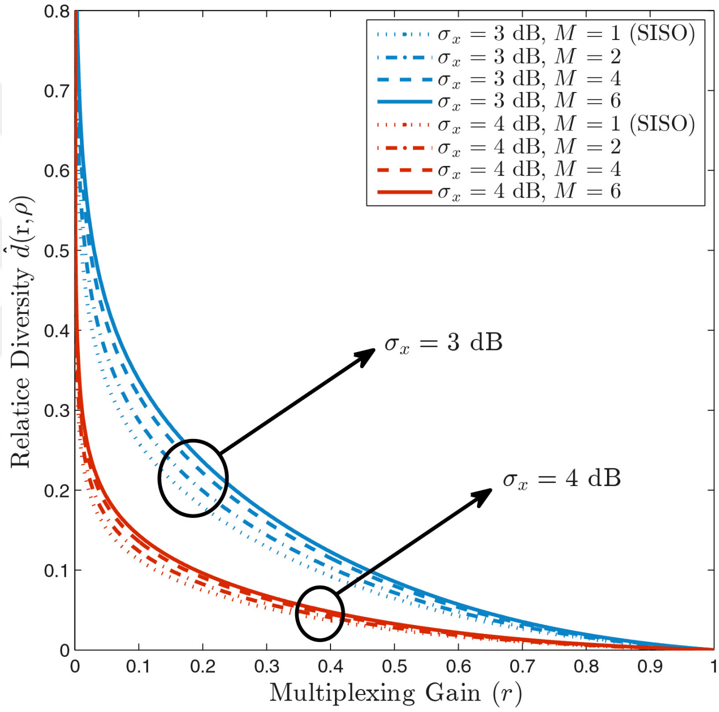

Figure 20: Effect of M and σ_x on the DMT of the MISO system ($\sigma_x = 3$, 4 dB and $M = 1$, 2, 4, 6).

In Fig. 21, we investigate the relative finite-SNR DMT of a 2×2 MIMO system (see Special Case). We assume SNR values of 10 and 20 dB and $\sigma_x = 3$ and $\sigma_x = 4$ dB. It can be observed that as SNR increases DMT curve shows better performance. Specifically, at $r = 0.1$ and SNR = 10 dB, diversity gains of 0.64 and 0.15 are achieved respectively for the cases of $\sigma_x = 3$ and $\sigma_x = 4$ dB. These climb up to 1.50 and 0.37 when SNR increases to 20 dB. It can be also observed that the case of $\sigma_x = 3$ dB shows better performance in comparison with $\sigma_x = 4$ dB at both SNR values under consideration. Finally, all cases indicate poor multiplexing gain performance. Specifically, for $r > 1$ the relative diversity gain for all of the cases is approximately zero as earlier discussed in Fig. 19.

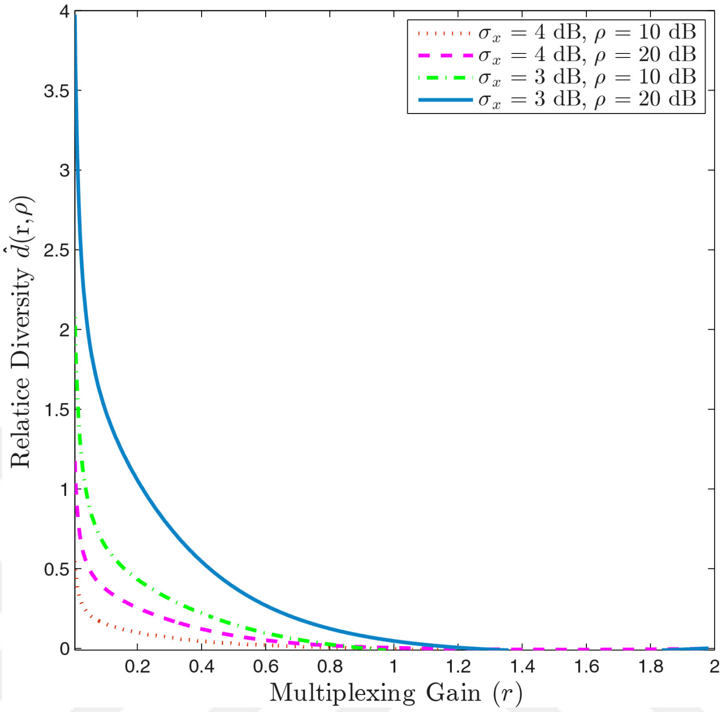

Figure 21: Relative finite-SNR DMT curves of the 2×2 MIMO system over log-normal fading.

In conclusion of this chapter, we have investigated the DMT over MIMO log-normal fading channels. We first have derived the asymptotical DMT for MIMO systems. Our results have shown that the asymptotical maximum diversity gain tends to infinity with $\ln(SNR)$. To have a fair comparison of gains between different cases, we have normalized the diversity gains with that of a benchmark (i.e., SISO case) and used the concept of relative asymptotical DMT. The relative asymptotical DMT curve is described by $MN(1-r)^2$ and a maximum diversity gain of MN can be obtained. Then, we have focused on finite-SNR DMT which does not yield a closed-form expression for the general MIMO case. As special cases, we have investigated MISO/SIMO systems and 2×2 MIMO system. Numerical results for MIMO systems show that at high SNR values, multiplexing gains are achievable at the price of very low diversity gains. This means that while designing coding schemes for MIMO systems over log-normal channel, one may decide to invest more on extracting diversity other than multiplexing.

CHAPTER IV

ADAPTIVE MIMO FSO SYSTEMS

As discussed in previous chapter, In MIMO FSO system, the spacetime transmission strategy can also be adjusted, introducing a new dimension for adaptation. The understanding of DMT under log-normal fading channel in Chapter 3 will allow us to investigate practical MIMO link adaptation algorithms for FSO links which provide a dynamic adaptation between diversity and multiplexing modes of operation. We suggest a framework for practical MIMO FSO system with adaptive architectures and show how to use this framework to increase either link reliability (via diversity gain) and or data rates (via multiplexing gain). We proposed a judiciously designed switching mechanism which chooses different operation modes, i.e., diversity, multiplexing or hybrid, based on the fundamental DMT discussed in chapter 3.

In this Chapter, we propose an adaptive MIMO FSO system with dynamic adaptation between spatial modes of operation. The proposed adaptive system supports three MIMO modes. In spatial multiplexing mode, the system transmits independent parallel data streams over multiple apertures to increase data rate. In diversity mode, the system transmits coded streams through multiple apertures to extract diversity gains. In the hybrid mode, a trade-off between diversity and multiplexing gains is targeted. For each operation mode, we first derive the outage probability for MIMO FSO system over log-normal turbulence channels. Then, we formulate the design of adaptive FSO system as to select the MIMO mode that yields the highest throughput while satisfying a predefined target outage probability. Extensive numerical results are provided to demonstrate the performance of proposed adaptive scheme.

4.1 Signal Model

We consider an adaptive MIMO FSO system with M transmit and N receive apertures over a frequency-flat log-normal fading channel. The maximum number of degrees of freedom is defined by $\min\{M, N\}$ and, without loss of generality, we assume $M \leq N$. The adaptive system supports three MIMO modes. In spatial multiplexing mode, the system transmits independent parallel data streams over M apertures to increase data rate. In diversity mode, the system transmits coded streams through multiple apertures to extract diversity gains. Unlike RF communications where sophisticated space-time codes are required to achieve diversity gains, simple repetition codes can be used for this purpose [106] and are also adopted in our system. In the hybrid mode, a trade-off between diversity and multiplexing gains is targeted. In this mode, k parallel streams are sent across the M transmit apertures. In particular, we assume that k repetition codes run over M/k different sets of apertures.

Let x_i, $i = 1, 2, ..., M$ denote the modulated symbols with unit power. We consider intensity modulation with direct detection (IM/DD). Based on the MIMO mode, the transmitted signal takes different forms. In multiplexing mode, we have M independent streams of data and the transmitted signal is therefore in the form of $\mathbf{x}^A = (x_1, x_2, \ldots, x_M)^T$. In diversity mode, we have $\mathbf{x}^B = (x_1, x_1, \ldots, x_1)^T$ where the same signal is simply repeated across M transmit apertures. Here, without loss of generality, we assume that x_1 is repeated. Finally, in hybrid mode with k parallel streams, we have $\mathbf{x}^C = (\mathbf{x}_1, \mathbf{x}_2, \ldots, \mathbf{x}_k)^T$ where $\mathbf{x}_i$ is a vector of length M/k and denotes the repeated signals over M/k transmit apertures.[1]

The baseband signal model is then given by

$$\mathbf{y} = \frac{\eta L P_T}{M}\mathbf{H}\mathbf{x}^U + \mathbf{w},\ U \in \{A, B, C\} \tag{72}$$

where P_T is the total optical transmit power budget and η is electro-optical conversion constant. In (72), $\mathbf{w} \in \mathbb{R}^N$ is additive white Gaussian noise (AWGN) vector

[1] We assume that M and N are multiples of k.

with independent and identically distributed (i.i.d.) entries, i.e., $w_i \sim \mathcal{N}(0, N_0/2)$, $i = 1, 2, \ldots, N$. Here, N_0 [W/Hz] denotes the value of double-sided power spectral density. In (72), L is the path loss [107, 108] which combine geometric loss in (6) and atmospheric loss (14)-(16) defined in Chapter 2.

In (72), $\mathbf{H} \in \mathbb{R}^{M\times N}$ denotes the fading channel matrix whose element h_{ij} ($i = 1, 2, \ldots, N$, $j = 1, 2, \ldots, M$) represents the channel gain between the j^{th} transmit aperture and the i^{th} receive aperture. Under the assumption of slow fading, we assume that the channel coefficients remain constant over a block of r symbols, i.e., r is much smaller than the channel coherence time. The channel matrix elements are assumed to be independent and identically distributed. Under weak turbulence conditions, we model the turbulence-induced fading coefficient with log-normal distribution. Dropping the index for notational convenience, we express the probability density function (pdf) as

$$f_h(h) = \frac{1}{h\sqrt{2\pi\sigma_{\ln h}^2}} \exp\left(-\frac{\left(\ln(h) + \sigma_{\ln h}^2/2\right)^2}{2\sigma_{\ln h}^2}\right) \tag{73}$$

where $\sigma_{\ln h}^2$ is the log-irradiance variance. In weak turbulence, we have $\sigma_{\ln h}^2 \cong \sigma_R^2$ [73] where the Rytov variance is $\sigma_R^2 = 1.23(2\pi/\lambda)^{7/6} C_n^2 d^{11/6}$ with C_n^2 denoting the refractive-index structure constant. The pdf in (73) satisfies $E[h] = 1$ to ensure that the fading does not attenuate or amplify the average power.

4.2 Adaptive Algorithm Design

The block diagrams of transmitter and receiver for the proposed adaptive MIMO system are illustrated in Fig. 22. The transmitter is equipped with an adaptation module which chooses one of the operation modes described in Section 4.1 (i.e., multiplexing, diversity or hybrid) based on the feedback. During operation, the receiver first calculates the instantaneous signal-to-noise ratio (SNR) which is a function of turbulence-induced fading. The SNR is compared against the SNR thresholds available in a look-up table (LUT) and the optimal transmission mode is selected accordingly. The transmitter is then informed of the selected mode via a low-rate control channel and adaptively switches between MIMO modes.

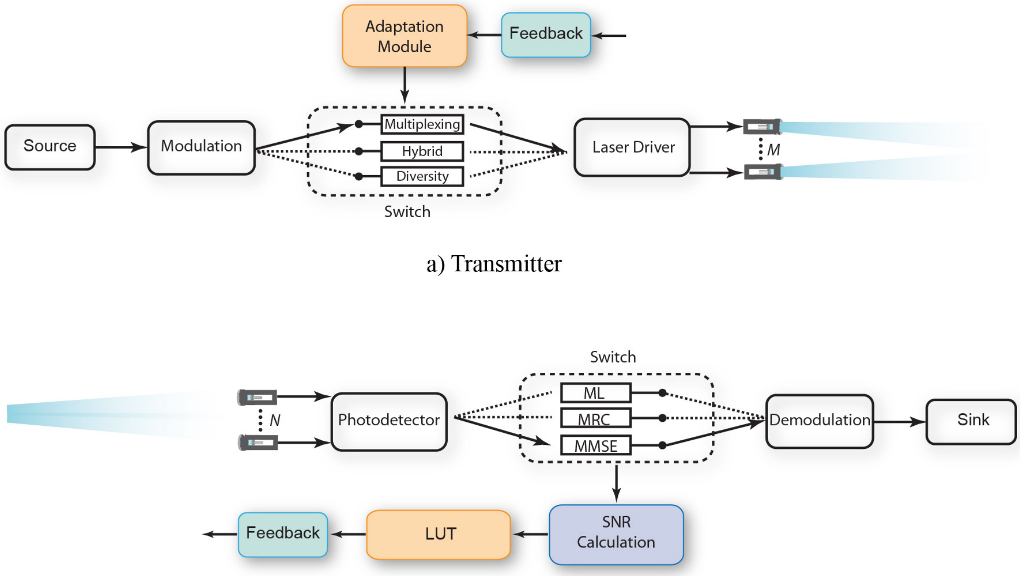

b) Receiver

Figure 22: Block diagram of adaptive MIMO FSO communication system. a) Transmitter, b) Receiver.

We formulate the adaptive system design, i.e., construction of LUT, to maximize the data rate while satisfying a predefined outage probability for a given channel realization. An outage is defined as the event that the channel does not support a target data rate, or in other words, when the instantaneous channel capacity is less than the target data rate, R [bits/s/Hz]. Therefore, the outage probability is given by

$$P_{out}\left(R,\rho\right) = \Pr\left\{C\left(\mathbf{H}\right) < R\right\} \tag{74}$$

where $C\left(\mathbf{H}\right)$ denotes the instantaneous channel capacity. It is given by [109]

$$C\left(\mathbf{H}\right) = \frac{1}{2}\log\left(\left|\mathbf{I}_N + \frac{\rho}{M^2}\mathbf{H}\mathbf{H}^T\right|\right) \tag{75}$$

where ρ is the electrical SNR defined as

$$\rho = 2\eta^2 L^2 \frac{P_T^2}{N_0}. \tag{76}$$

Outage capacity is the maximum achievable rate while keeping the outage probability less than a specified value denoted by ε. Mathematically, we can write [109]

$$C_{\varepsilon}(\rho) = \max\{R : P_{out}(R,\rho) \leq \varepsilon\} \tag{77}$$
$$= F_C^{-1}(\varepsilon)$$

where $F_C(.)$ is the cumulative distribution function (CDF) of $C(\mathbf{H})$.

Let D denote the set of divisors of M. Further, let $P_{out}^{k}(R,\rho)$ and $C_{\varepsilon}^{k}(\rho)$, $k \in D$, denote the outage probability and the outage capacity for the k^{th} operation mode. $k = 1$ and $k = M$ correspond to diversity and spatial multiplexing modes respectively. In the hybrid mode, we have $k \in D$ and $k \neq 1,\ k \neq M$. The range of SNR values under consideration is divided into regions such that, in each region, the operation mode that provides the maximum capacity is selected. The design problem is therefore formulated as

$$\hat{k} = \arg\max_{k} C_{\varepsilon}^{k}(\rho) \tag{78}$$

where $\hat{k} \in D$ denotes the selected operation mode for SNR value of ρ. The threshold points where we switch from one operation mode to another are then determined to construct the LUT.

The derivations of outage capacity expressions for different operation modes are provided in the following.

4.2.1 Outage Performance of Spatial Multiplexing Mode

In spatial multiplexing, the maximum number of degrees of freedom is $\min\{M,N\} = M$. Hence, the channel matrix reduces to a diagonal form of $\mathbf{H} = diag\{h_1, h_2, ..., h_M\}$. From (74) and (75), the outage probability can be written as

$$P_{out}^{M}(R,\rho) = \Pr\left\{\frac{1}{2}\sum_{j=1}^{M}\log\left(1+\frac{\rho}{M^2}|h_j|^2\right) < R\right\}. \tag{79}$$

Considering the overall data rate and the maximum number of degrees of freedom, a rate of R/M should be supported per sub-channel. Outage occurs if a sub-channel cannot support this rate. Mathematically speaking, the probability in

(79) reduces to multiplication of independent outage events for each sub-channel. Then we have

$$P_{out}^{M}(R,\rho)=\left[\Pr\left\{\frac{1}{2}\log\left(1+\frac{\rho}{M^2}|h_1|^2\right)<\frac{R}{M}\right\}\right]^M \tag{80}$$

where the inner probability can be written in the form of a Q-function, i.e., $Q(x)=\sqrt{1/2\pi}\int_x^{\infty}\exp\left(-u^2/2\right)du$. The outage probability can be then found as

$$P_{out}^{M}(R,\rho)=\left[Q\left(\frac{1}{2\sigma_{\ln h}}\ln\left(\frac{\rho/M^2}{2^{2R/M}-1}\right)-\frac{\sigma_{\ln h}}{2}\right)\right]^M. \tag{81}$$

In order to find outage capacity, we solve (81) for R and then ε-capacity is obtained as

$$C_{\varepsilon}^{M}(\rho)=\frac{M}{2}\log\left[\frac{\rho}{M^2}\exp\left(-2\sigma_{\ln h}Q^{-1}\left(\varepsilon^{1/M}\right)-\sigma_{\ln h}^2\right)+1\right] \tag{82}$$

4.2.2 Outage Performance of Diversity Mode

Under the assumption of repetition coding, (72) simplifies to

$$y_i=\frac{\eta L}{M}\left(\sum_{j=1}^{M}h_{ij}\right)x_1^B+w_i \quad \text{for} \quad i=1,...,N. \tag{83}$$

The outage probability can be then found as

$$P_{out}^{1}(R,\rho)=\Pr\left\{\frac{1}{2}\log\left(1+\frac{\rho}{M^2}\sum_{i=1}^{N}\left(\sum_{j=1}^{M}h_{ij}\right)^2\right)<R\right\}. \tag{84}$$

The term $\sum_{i=1}^{N}\left(\sum_{j=1}^{M}h_{ij}\right)^2$ is the sum of log-normal random variables and can be approximated by a log-normal distribution. First, we approximate the inner sum as $e^{z_i}=\sum_{j=1}^{M}h_{ij}$ with $\sigma_{z_i}^2=\ln\left(1+\left(e^{\sigma_{\ln h}^2}-1\right)/M\right)$ and $\mu_{z_i}=\ln(M)-\sigma_{z_i}^2/2$. Second, we approximate the outer sum as $e^u=\sum_{i=1}^{N}e^{2z_i}$ with $\sigma_u^2=\ln\left(1+\left(e^{4\sigma_{z_i}^2}-1\right)/N\right)$ and $\mu_u=\ln(N)+2\mu_z+\left(4\sigma_{z_i}^2-\sigma_u^2\right)/2$. Therefore, (84) can be approximated as

$$\begin{aligned}P_{out}^{1}(R,\rho)&\cong\Pr\left\{u<\ln\left(\frac{2^{2R}-1}{\rho/M^2}\right)\right\}\\&=Q\left(\frac{1}{\sigma_u}\ln\left(\frac{\rho/M^2}{2^{2R}-1}\right)+\frac{\mu_u}{\sigma_u}\right)\end{aligned} \tag{85}$$

In order to find outage capacity, we solve (85) for R and then ε-capacity is obtained as

$$C_{\varepsilon}^{1}(\rho)=\frac{1}{2}\log\left[\frac{\rho}{M^2}\exp\left(\mu_u-\sigma_uQ^{-1}(\varepsilon)\right)+1\right]. \tag{86}$$

4.2.3 Outage Performance of Hybrid Mode

This method combines diversity and spatial multiplexing by constructing k parallel streams across M transmit apertures. In particular, repetition codes run over M/k different sets of apertures. The i^{th} received signal at the l^{th} stream is written as

$$y_{i,l} = \frac{\eta L}{M}\left(\sum_{j=1}^{M/k} h_{ij}^{l}\right) x_{l}^{C} + w_{i,l} \tag{87}$$

$$\text{for} \quad i = 1, ..., N/k \quad \text{and} \quad l = 1, ..., k$$

where h_{ij}^{l} is the channel coefficient from the j^{th} transmit aperture to the i^{th} receive aperture in the l^{th} stream. To simplify the notation, we further define $\alpha_{i,l} = \sum_{j=1}^{M/k} h_{ij}^{l}$, $i = 1, ..., N/k$ and $l = 1, ..., k$, which is the sum of log-normal random variables and can be approximated by a log-normal distribution as discussed earlier.

In this transmission mode, the channel matrix $\mathbf{H}$ can be written in the following format:

$$\mathbf{H} = \begin{bmatrix} \alpha_{1,1} & 0 & \cdots & 0 \\ \vdots & & & \vdots \\ \alpha_{N/k,1} & & & \vdots \\ 0 & \ddots & & 0 \\ \vdots & & \ddots & \alpha_{1,k} \\ \vdots & & & \vdots \\ 0 & \cdots & 0 & \alpha_{N/k,k} \end{bmatrix}_{N\times k} \tag{88}$$

It can be readily verified that $\mathbf{HH}^T$ is a block diagonal matrix and given by

$$\mathbf{HH}^T = \begin{bmatrix} \mathbf{A}_1 & 0 & \cdots & 0 \\ 0 & \mathbf{A}_2 & \cdots & 0 \\ \vdots & \vdots & \ddots & \vdots \\ 0 & 0 & \cdots & \mathbf{A}_k \end{bmatrix}_{N\times N} = \mathbf{A}_1 \oplus \mathbf{A}_2 \oplus \cdots \oplus \mathbf{A}_k \tag{89}$$

where $\mathbf{A}_l = \boldsymbol{\alpha}_l^T \boldsymbol{\alpha}_l$ and $\boldsymbol{\alpha}_l = [\alpha_{1,l}, \alpha_{2,l}, \ldots, \alpha_{N/k,l}]$, $l = 1, ..., k$ with matrix dimensions $(N/k) \times (N/k)$. Replacing (89) in (75) we obtain

$$\begin{aligned} C(\mathbf{H}) &= \frac{1}{2} \log \left(\left| \mathbf{I}_N + \frac{\rho}{M^2} (\mathbf{A}_1 \oplus \mathbf{A}_2 \oplus \cdots \oplus \mathbf{A}_k) \right| \right) \\ &= \frac{1}{2} \log \left(\left| \left(\mathbf{I}_{N/k} + \frac{\rho}{M^2} \mathbf{A}_1 \right) \oplus \left(\mathbf{I}_{N/k} + \frac{\rho}{M^2} \mathbf{A}_2 \right) \oplus \cdots \oplus \left(\mathbf{I}_{N/k} + \frac{\rho}{M^2} \mathbf{A}_k \right) \right| \right) \\ &= \frac{1}{2} \log \left(\left| \left(\mathbf{I}_{N/k} + \frac{\rho}{M^2} \mathbf{A}_1 \right) \right| \times \left| \left(\mathbf{I}_{N/k} + \frac{\rho}{M^2} \mathbf{A}_2 \right) \right| \times \cdots \times \left| \left(\mathbf{I}_{N/k} + \frac{\rho}{M^2} \mathbf{A}_k \right) \right| \right) \\ &= \frac{1}{2} \sum_{l=1}^{k} \log \left(\left| \left(\mathbf{I}_{N/k} + \frac{\rho}{M^2} \mathbf{A}_l \right) \right| \right) \end{aligned} \tag{90}$$

In (90), the second equality comes from the diagonality of block matrix, the third equality comes from its determinant properties, and the last equality comes from logarithm function properties. Replacing (90) in (74), we have

$$P_{out}^k (R, \rho) = \Pr \left\{ \frac{1}{2} \sum_{l=1}^{k} \log \left(\left| \left(\mathbf{I}_{N/k} + \frac{\rho}{M^2} \mathbf{A}_l \right) \right| \right) < R \right\}. \tag{91}$$

In hybrid transmission mode, outage occurs if a stream cannot support a rate of R/k. Mathematically speaking, we have

$$P_{out}^k (R, \rho) = \left[\Pr \left\{ \frac{1}{2} \log \left(\left| \left(\mathbf{I}_{N/k} + \frac{\rho}{M^2} \mathbf{A}_l \right) \right| \right) < \frac{R}{k} \right\} \right]^k. \tag{92}$$

The inner determinant can be found by replacing $\mathbf{A}_l = \boldsymbol{\alpha}_l^T \boldsymbol{\alpha}_l$ and using the Sylvester's determinant identity, i.e.,

$$\left| \left(\mathbf{I}_{N/k} + \frac{\rho}{M^2} \boldsymbol{\alpha}_l^T \boldsymbol{\alpha}_l \right) \right| = \left| \left(1 + \frac{\rho}{M^2} \boldsymbol{\alpha}_l \boldsymbol{\alpha}_l^T \right) \right|. \tag{93}$$

Therefore, the outage probability will be simplified as

$$P_{out}^k (R, \rho) = \left[\Pr \left\{ \frac{1}{2} \log \left(1 + \frac{\rho}{M^2} \sum_{i=1}^{N/k} |\alpha_{i,l}|^2 \right) < \frac{R}{k} \right\} \right]^k. \tag{94}$$

It can be noted that the inner probability in (94) has a similar form to (84), i.e., outage probability earlier obtained for the diversity mode. The summation in (94) can be approximated by a log-normal random variable as $e^{u'} = \sum_{i=1}^{N/k} |\alpha_{i,l}|^2$ with $\alpha_{i,l} = \sum_{j=1}^{M/k} h_{ij}^l$. Following similar steps in Section 4.2.3, we obtain

$$P_{out}^k (R, \rho) = \left[Q \left(\frac{1}{\sigma_{u'}(k)} \ln \left(\frac{\rho / M^2}{2^{2R/k} - 1} \right) + \frac{\mu_{u'}(k)}{\sigma_{u'}(k)} \right) \right]^k. \tag{95}$$

In (95), $\sigma_{u'}^2(k)$ and $\mu_{u'}(k)$ respectively denote the variance and mean of u' and are given by

$$\sigma_{u'}^2(k) = \ln\left(1 + \left(e^{4\sigma_{z'_i}^2(k)} - 1\right)/[N/k]\right) \tag{96}$$

$$\mu_{u'}(k) = \ln\left(\frac{N}{k}\right) + 2\mu_{z'_i}(k) + \frac{1}{2}\left(4\sigma_{z'_i}^2(k) - \sigma_{u'}^2(k)\right) \tag{97}$$

where we define $z'_i = \ln \alpha_{i,l}$ with variance $\sigma_{z'_i}^2(k) = \ln\left(1 + \left(e^{\sigma_{\ln h}^2} - 1\right)/[M/k]\right)$ and mean $\mu_{z'_i}(k) = \ln(M/k) - \sigma_{z'_i}^2/2$. In order to find outage capacity, we solve (95) for R and then ε-capacity is obtained after some mathematical manipulations as

$$C_\varepsilon^k(\rho) = \frac{k}{2}\log\left[1 + \rho\frac{\exp\left(\mu_{u'}(k) - \sigma_{u'}(k)\,Q^{-1}\left(\varepsilon^{1/k}\right)\right)}{M^2}\right]. \tag{98}$$

4.3 Numerical Results

In this section, we consider 4×4 and 6×6 MIMO systems, construct LUTs for adaptive systems and present their outage performance highlighting the improvements. We consider an operating wavelength of $\lambda = 1550$ nm and refractive-index structure constant $C_n^2 = 10^{-14}$ m$^{-2/3}$. This yields Rytov variance of $\sigma_{\ln h}^2$ =0.2 for $d = 1$ km. We further assume noise power of $N_0 = 10^{-4}$, receiver aperture diameter $D_r = 10$ cm, and electro-optical conversion constant $\eta = 1$. Unless otherwise stated, we assume visibility $V = 10$ km, and beam divergence angle of $\theta_{tx} = 1$ mrad.

In Fig. 23, we plot the outage capacity of adaptive 4×4 MIMO FSO link with a targeted outage of $\varepsilon = 0.1$ for three operation modes under consideration. The outage capacity of SISO case (i.e., $M = N = 1$) is depicted as a benchmark. In diversity mode, we set $k = 1$ and repetition code runs over all transmit apertures. In multiplexing mode, we set $k = 4$ indicating four streams in parallel. In hybrid mode, we set $k = 2$ where two different repetition codes run in parallel. The corresponding outage capacities for multiplexing, diversity and hybrid modes are obtained respectively based on (82), (86) and (98). Based on (78), the LUT is constructed specifying the SNR regions where each transmission mode should be used (see Table 5 and 6). In each SNR region, the adaptive algorithm selects the mode which results in the highest outage capacity. The performance of the adaptive scheme is therefore presented based on the aggregation of underlying three plots. It can be observed that for SNR values less than 11.6 dB, the adaptive system works in diversity mode as it yields the highest rate in poor channel conditions. For SNR values between 11.6 and 19 dB, the adaptive system is in hybrid mode to ensure a trade-off between the link reliability and the data rate. Finally, for SNR values greater than 19 dB, multiplexing mode should be active to ensure highest data rate.

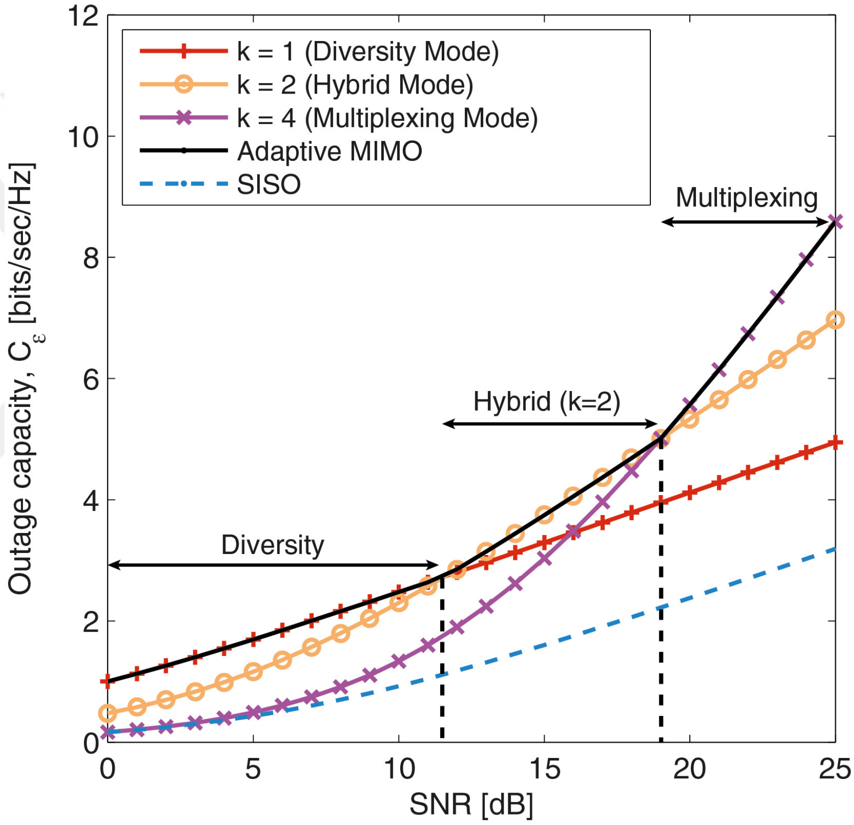

Figure 23: Outage capacity of adaptive 4×4 MIMO FSO system ($d = 1$ km).

In Fig. 24, we plot the outage capacity of a 6×6 MIMO FSO link assuming a targeted outage of $\varepsilon = 0.1$. Here, we change the number of streams as $k = 1$, 2, 3, and 6. The cases of $k = 1$ and $k = 6$ correspond respectively to diversity and multiplexing modes. The cases of $k = 2$ and $k = 3$ correspond to the hybrid mode. The LUT is provided in Table 7. It is observed that for SNR values less than 9.3 dB, diversity mode should be active while hybrid mode with either $k = 2$ or $k = 3$

Table 5: LUTs for a 4×4 adaptive MIMO FSO system assuming different link distances ($\varepsilon = 0.1$).

	Diversity ($k = 1$)	Hybrid ($k = 2$)	Multiplexing ($k = 4$)
$d = 1$ km	$\rho < 11.6$ dB	$11.6 < \rho < 19.0$ dB	$\rho > 19.0$ dB
$d = 2$ km	$\rho < 14.0$ dB	$14.0 < \rho < 20.0$ dB	$\rho > 20.0$ dB
$d = 3$ km	$\rho < 17.8$ dB	$17.8 < \rho < 22.0$ dB	$\rho > 22.0$ dB
$d = 4$ km	$\rho < 20.4$ dB	$20.4 < \rho < 23.0$ dB	$\rho > 23.0$ dB
$d = 5$ km	$\rho < 20.0$ dB	$20.0 < \rho < 21.0$ dB	$\rho > 21.0$ dB

Table 6: LUTs for a 4×4 adaptive MIMO FSO system assuming different values of targeted outage probability ($d = 1$ km).

	Diversity ($k = 1$)	Hybrid ($k = 2$)	Multiplexing ($k = 4$)
$\varepsilon = 10^{-1}$	$\rho < 11.6$ dB	$11.6 < \rho < 19.0$ dB	$\rho > 19.0$ dB
$\varepsilon = 10^{-2}$	$\rho < 14.0$ dB	$14.0 < \rho < 22.5$ dB	$\rho > 22.5$ dB
$\varepsilon = 10^{-3}$	$\rho < 16.0$ dB	$16.0 < \rho < 25.0$ dB	$\rho > 25.0$ dB
$\varepsilon = 10^{-4}$	$\rho < 17.0$ dB	$17.0 < \rho < 26.9$ dB	$\rho > 26.9$ dB
$\varepsilon = 10^{-5}$	$\rho < 18.2$ dB	$18.2 < \rho < 28.5$ dB	$\rho > 28.5$ dB

can be used for the SNR range of 9.3 dB - 20.7 dB. For SNR values greater than 20.7 dB, multiplexing mode can be used.

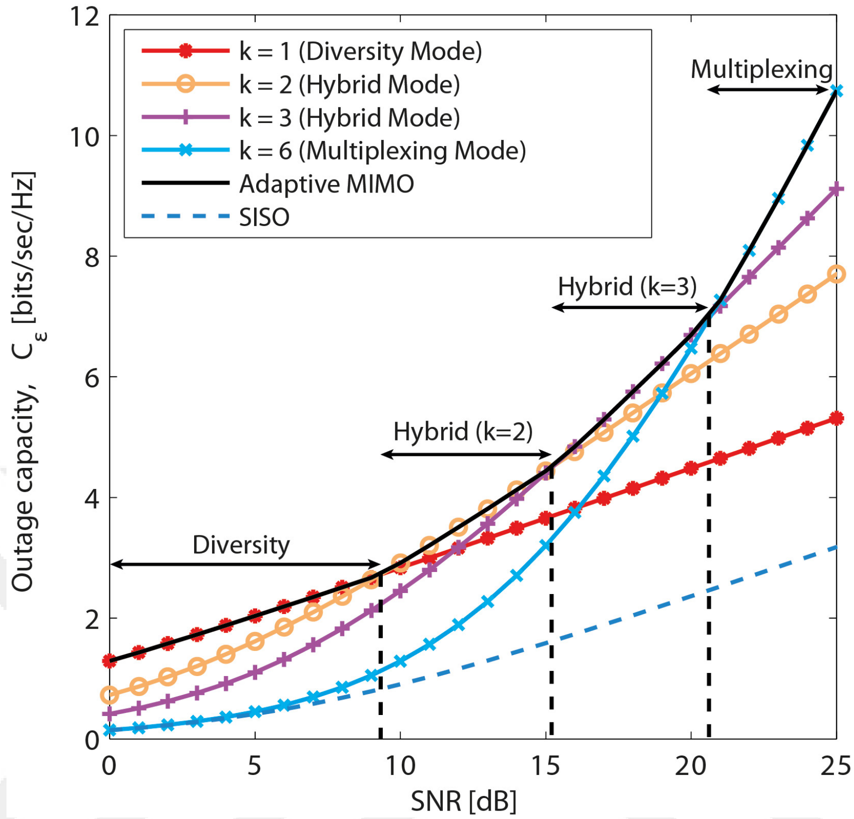

Figure 24: Outage capacity of adaptive 6×6 MIMO FSO system ($d = 1$ km).

Table 7: LUT for a 6×6 adaptive MIMO FSO system ($d = 1$ km and $\varepsilon = 0.1$).

Diversity ($k = 1$)	Hybrid ($k = 2$)	Hybrid ($k = 3$)	Multiplexing ($k = 6$)
$\rho < 9.3$	$9.3 < \rho < 15.3$	$15.3 < \rho < 20.7$	$\rho > 20.7$

While similar trends are observed for the performances of 4×4 and 6×6 MIMO FSO links, it can be noted that 6×6 MIMO scheme gives more flexibility by providing two regions for hybrid case, (see $k = 2$ and $k = 3$ in Fig. 24). The partitioning of SNR region for operation modes is also different. For example, the diversity mode is active for the 4×4 MIMO FSO link when $\rho < 11.6$ dB. This reduces to $\rho < 9.3$ dB for a 6×6 MIMO FSO link. Furthermore, it can be observed that the achievable data rates for a 6×6 MIMO FSO link are higher than those in 4×4 MIMO case as expected. Specifically, at SNR = 25 dB, a maximum data rate of 10.7 bits/sec/Hz can be achieved for a 6×6 MIMO FSO link, while this value for a 4×4 MIMO FSO link is equal to 8.5 bits/sec/Hz.

In Fig. 25, we investigate the performance of adaptive system under different visibility levels. Specifically, we consider $V = 1$, 2, 4, 7, and 10 km and plot the outage capacity of 6×6 MIMO FSO system with respect to optical transmit power P_T. We assume a targeted outage of $\varepsilon = 0.1$. Specifically, at $P_T = -10$ dB, the outage capacities of 1.95, 4.47, 6.58, 7.88, and 8.20 bits/s/Hz are achieved for $V = 1$, 2, 4, 7, and 10 km respectively. It is observed that the visibility (determined by weather conditions) is a critical factor and the outage capacity significantly decreases with poor visibility.

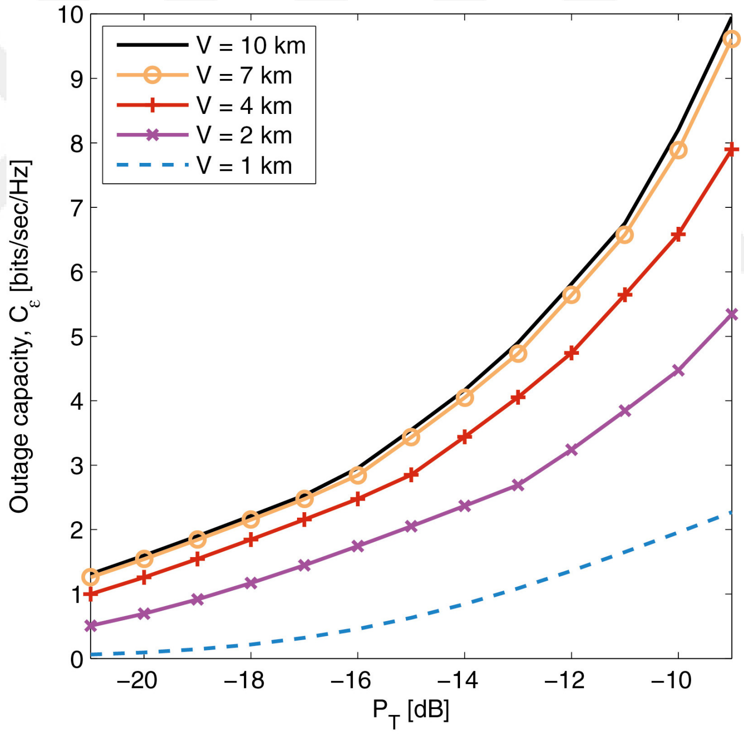

Figure 25: Effect of visibility on the outage capacity of adaptive 6×6 MIMO FSO system.

In Fig. 26, we investigate the effect of beam divergence angle. We assume $\varepsilon = 0.1$ km and plot the outage capacity of 6×6 MIMO FSO system for $\theta_{tx} = 0.5$, 0.75, 1, 1.5, and 2 mrad. Specifically, at $P_T = -10$ dB, the outage capacities of 19.55, 12.72, 8.20, 4.46, and 2.94 bits/s/Hz are achieved for $\theta_{tx} = 0.5$, 0.75, 1, 1.5, and 2 mrad. For smaller divergence angles, i.e., narrower beams, since more energy is captured by the receiver aperture, less power loss is experienced. Consequently, the outage capacity increases.

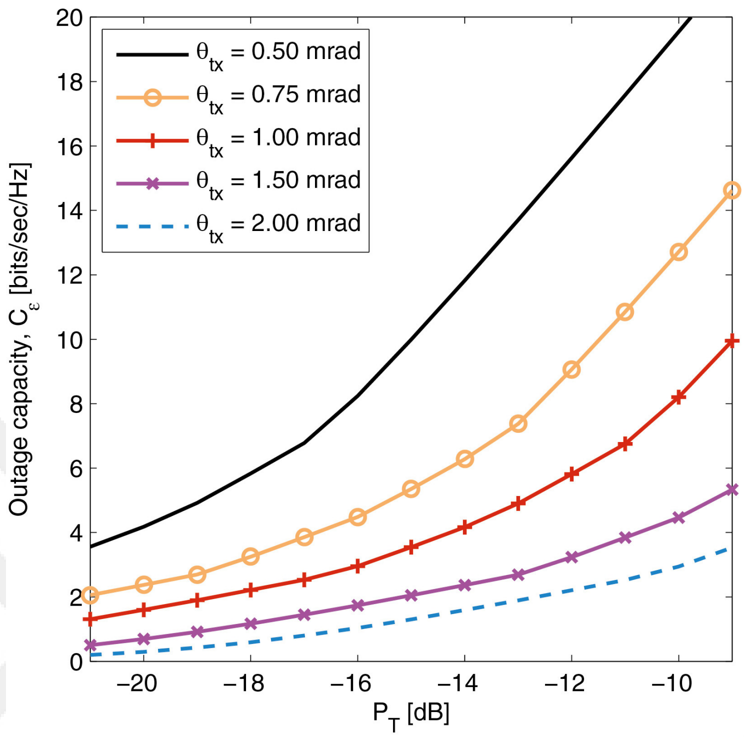

Figure 26: Effect of transmitter divergence angle on the outage capacity of adaptive 6×6 MIMO FSO system.

In conclusion of this chapter, we proposed an adaptive MIMO FSO system where a judiciously designed switching mechanism chooses different operation modes, i.e., diversity, multiplexing or hybrid, based on channel conditions. We formulated the design of adaptive FSO system as a maximization problem of the outage capacity while satisfying a predefined target outage probability. We calculated the outage capacities for each operation mode and constructed the LUTs. In the proposed system, the received SNR is compared against the SNR thresholds available in the LUT and the optimal transmission mode is selected accordingly. Our numerical results revealed that the proposed system has significant improvements over stand-alone diversity and multiplexing schemes and ensure an overall robust performance throughout the SNR range.

CHAPTER V

ADAPTIVE MODULATION AND POWER CONTROL

The understanding of DMT under log-normal fading channel created the basis for us to investigate practical MIMO link adaptation algorithms for FSO links. An adaptive MIMO FSO system with dynamic adaptation between spatial modes of operation was proposed in Chapter 4. We suggested a framework for practical MIMO FSO system with adaptive architectures and show how to use this framework to increase either link reliability (via diversity gain) and or data rates (via multiplexing gain). In summary, we proposed a judiciously designed switching mechanism which chooses different operation modes, i.e., diversity, multiplexing or hybrid, based on the channel conditions. The spatial adaptation can be combined with conventional adaptive modulation and coding (AMC) to give the optimal system performance. In contrast to previous chapter where the modulation size/type and power where constant, in Chapter 5, we extend the adaptive scheme and formulate the design of adaptive modulation and power control algorithms for multiple aperture FSO systems.

In this Chapter, we consider MISO and SIMO FSO systems with PPM and PAM. We propose three adaptive algorithms where the modulation size and/or transmit power are adjusted according to the channel conditions. We formulate the design of adaptive algorithms to maximize the spectral efficiency under peak and average power constraints while maintaining a targeted value of outage probability. We present extensive Monte Carlo simulations to demonstrate the performance of proposed adaptive schemes over turbulence channels.

5.1 System Model

In this section, we first summarize the channel characteristics, then introduce the signal model under consideration.

5.1.1 Channel Model

We consider an FSO system with a link distance of d. Let θ_{tx} and D_{rx} respectively denote the beam divergence angle and receiving lens diameter. The path loss is then expressed as [110, 111] $L = D_{rx}^2 e^{-\alpha d}/(\theta_{tx} d)^2$ where α represents the atmospheric attenuation coefficient. It is given by [111] $\alpha = (3.91/V)\,(\lambda/550)^{-q}$ where λ is wavelength, V is visibility in kilometers (km) and q is a visibility-dependent parameter [112]. To model atmospheric turbulence, we consider both log-normal (LN) and Gamma-Gamma (GG) distributions, covering respectively weak and moderate-to-strong turbulence conditions [113]. Assuming LN turbulence model, the probability density function (pdf) of the channel coefficient h is given by

$$f_h\left(h\right) = \frac{1}{h\sqrt{2\pi\sigma_{\ln h}^2}} \exp\left(-\frac{\left(\ln\left(h\right) + \sigma_{\ln h}^2/2\right)^2}{2\sigma_{\ln h}^2}\right), \tag{99}$$

where $\sigma_{\ln h}^2$ is the log-irradiance variance and can be expressed in terms of the scintillation index (σ_h^2) as $\sigma_{\ln h}^2 = \ln\left(\sigma_h^2 + 1\right)$. In weak turbulence, we have $\sigma_{\ln h}^2 \cong \sigma_R^2$ [113] where the Rytov variance is $\sigma_R^2 = 1.23(2\pi/\lambda)^{7/6} C_n^2 d^{11/6}$ with C_n^2 denoting the refractive-index structure constant.

Under GG model, the pdf of h is given by [113]

$$p_h\left(h\right) = \frac{2}{\Gamma\left(\alpha\right)\Gamma\left(\beta\right) I} (\alpha\beta I)^{(\alpha+\beta)/2} K_{\alpha-\beta}\left(2\sqrt{\alpha\beta I}\right), \tag{100}$$

where $\Gamma\left(x\right)$ is the gamma function and $K_\mu\left(x\right)$ is the modified Bessel function of the second kind. α and β represent the effective numbers of large- and small-scale scatterers, respectively. They are given by $\alpha = 1/\sigma_x^2 = \left[\exp\left(\sigma_{\ln x}^2\right) - 1\right]^{-1}$ and $\beta = 1/\sigma_y^2 = \left[\exp\left(\sigma_{\mathrm{lny}}^2\right) - 1\right]^{-1}$. The scintillation index is given by $\sigma_h^2 = \exp\left(\sigma_{\ln x}^2 + \sigma_{\ln y}^2\right) - 1 = \alpha^{-1} + \beta^{-1} + (\alpha\beta)^{-1}$.

5.1.2 Signal Model

We consider a MISO system with n_t transmit apertures and a SIMO system with n_r apertures. We assume the deployment of M-ary PPM and M-ary PAM where $M = 2^n$, $n \in \mathbb{Z}^+$. In PPM, the symbol duration T_s, is divided into M parts and an optical pulse is transmitted in one of these chips according to the value of the symbol. To maintain average transmit power for all values of M, the amplitude of the pulse in chip duration is increased with increase of M. In PAM, the information is modulated into the intensity of the optical pulse and each mapping represents a constant pulse with a different amplitude through the symbol duration.

Let $x_i(t)$, $i = 1, 2, \ldots, n_t$, $0 \leq t < T_s$ denote the modulation symbol transmitted from the i^{th} aperture. Furthermore, let x_i denote its vector space representation[1]. The transmitted symbol can be then written as $x_i(t) = P_t + s_m(t)$, $m = 1, 2, \ldots, M$, $i = 1, 2, ..., n_t$ where P_t represents the average optical transmit power per symbol duration, i.e., $\overline{x_i(t)} = P_t$. Here, $s_m(t)$ denotes PAM/PPM modulation symbol with unit power, respectively, given as

$$s_m(t) = \begin{cases} (M-1) P_t & (m-1)\frac{T_s}{M} \leq t < m\frac{T_s}{M} \\ -P_t & \text{otherwise} \end{cases}, \tag{101}$$

$$s_m(t) = (2m - 1 - M) \frac{P_t}{M-1} \quad \text{for} \quad 0 \leq t < T_s. \tag{102}$$

Let the transmitted and received signals be represented by $\mathbf{x} = (x_1, x_2, \ldots, x_{n_t})^T$ and $\mathbf{y} = (y_1, y_2, \ldots, y_{n_r})^T$, respectively. It should be noted that $\mathbf{x}$ and $\mathbf{y}$ respectively reduce to scalars for MISO and SIMO systems. Unlike RF communications where sophisticated space-time codes are required to achieve diversity gains, simple repetition codes can be used for FSO systems [114] and are also adopted in our MISO system. The baseband signal model is then given by

$$\mathbf{y} = \frac{\eta L}{n_t} \mathbf{h}\mathbf{x} + \mathbf{w}, \tag{103}$$

where η is electro-optical conversion constant which includes responsivity and transimpedance amplifier gain of photodetector. In the MISO system, $P_t^i = P_t / n_t$ is allocated for each transmit aperture. This ensures to make a fair comparison

[1]The dimension of PAM is one and therefore its vector space representation reduces to a scalar. On the other hand, PPM is represented by an M-dimensional vector. Here, we use italic letter to represent PPM signal although it is not scalar, to avoid confusion with MIMO representation.

between the MISO and SIMO schemes, since the total transmit power from the optical head is P_t in both cases.

In (103), the channel vector is denoted by $\mathbf{h} = (h_1, h_2, \ldots, h_{n_t})$, $\mathbf{h} \in \mathbb{R}^{n_t}$ for MISO system and $\mathbf{h} = (h_1, h_2, \ldots, h_{n_r})^T$, $\mathbf{h} \in \mathbb{R}^{n_r}$ for SIMO system. The channel matrix elements are assumed to be independent and identically distributed (i.i.d.). Under the assumption of quasi-static fading, we assume that the channel coefficients remain constant over a block of symbols where the block length is smaller than channel coherence time. In (103), denotes the additive white Gaussian noise (AWGN) vector with independent and identically distributed (i.i.d.) entries $w_i \sim \mathcal{N}(0, \sigma_w^2)$, $i = 1, 2, \ldots, n_r$. The variance, $\sigma_w^2 = N_0/2$, denotes the power of noise term. The autocorrelation matrix of noise signal is therefore defined by $\mathbf{R}_w = E\left(\mathbf{w}\mathbf{w}^T\right) = \sigma_w^2 \mathbf{I}_N$.

In MISO system where one receive aperture exists, the received signal will be a superposition of transmitted signals from n_t transmitters whereas in SIMO system with n_r receive apertures, equal gain combining (EGC) is used. The outputs are given as

$$y = \frac{\eta L}{n_t} \sum_{i=1}^{n_t} h_i x_1 + w_1 \qquad \text{for MISO} \tag{104a}$$

$$y = \eta L \sum_{i=1}^{n_r} h_i x_1 + \sum_{i=1}^{n_r} w_i \qquad \text{for SIMO} \tag{104b}$$

5.2 Adaptive Transmission Schemes

We propose three adaptive schemes where the modulation size and/or transmit power are adjusted according to the channel conditions. In the *first algorithm* which is called "Adaptive Modulation Algorithm-1 (AMA-1)", we assume only the use of PPM. While keeping the outage probability less than a pre-specified value, we aim to maximize spectral efficiency by adaptively changing the PPM size under power constraints. In the *second algorithm* which is called "Adaptive Modulation Algorithm-2 (AMA-2)", we assume the deployment of both PPM and PAM. In this algorithm, similar to the first one, we aim to maximize spectral efficiency, but this time we adaptively change both modulation type and size under power constraints. In the *third algorithm* which is called "Adaptive Modulation and Power Algorithm (AMPA)", we aim to maximize spectral efficiency by adaptively changing the transmit power and modulation size/type according to channel conditions.

In the proposed adaptive algorithms, the available received power region is optimally divided into a number of intervals and one transmission mode is assigned for each interval. These results are pre-computed and stored at the transmitter side as a look-up table (LUT). During the operation, receiver calculates the instantaneous received power according to the channel coefficients, and a feedback is provided to the transmitter determining the mode of transmission. The transmission mode is determined by checking which interval of the LUT the calculated received power falls in. The transmitter then switches to the selected mode of transmission. In terms of complexity, AMA-1 is simplest which only employs adaptation of PPM size. AMA-2 comes the second which employs both PPM and PAM schemes. In AMPA, power adaptation is further added which is an additional factor for complexity.

In the MISO system, as seen from (104a), the received signal is a superposition of transmitted signals from n_t transmitters. Similarly, in the SIMO system, it is observed from (104b) that the output of EGC is a superposition of received signals from n_r receive apertures. Therefore, in both cases, the *channel condition* is determined by $h_{eff} = (1/\kappa) \sum_{i=1}^{\kappa} h_i$, $\kappa \in \{n_t, n_r\}$. Having average optical transmit power of P_t, the *average* received power is given by $P_r = \eta L P_t$. The *instantaneous* received power as a function of channel condition can be then expressed as $P_r(h_{eff}) = \eta L P_t h_{eff} = P_r h_{eff}$. The *average* electrical signal-to-noise ratio (SNR) is therefore defined as

$$\bar{\rho} = \eta^2 L^2 \frac{\sigma_x^2}{\sigma_w^2}. \tag{105}$$

Consequently, the *instantaneous* SNR as a function of channel condition is $\rho(h_{eff}) =$

$\bar{\rho}h_{eff}^2$. For the calculation of (105), we need to determine the variances of the modulation signals which can be calculated from

$$\begin{aligned}\sigma_x^2 &= E\left[\overline{\left(x\left(t\right)-\overline{x\left(t\right)}\right)^2}\right] \\ &= E\left[\overline{\left(s_m\left(t\right)\right)^2}\right] = \begin{cases} P_t^2\left(M-1\right) & \text{for} \quad \text{PPM} \\ P_t^2\frac{(M+1)}{3(M-1)} & \text{for} \quad \text{PAM}\end{cases}\end{aligned} \tag{106}$$

where we assume equal-likely symbols. By replacing (106) in (105), we can write the *instantaneous* SNR as

$$\rho\left(h_{eff}\right) = \begin{cases} \frac{\left[P_r\left(h_{eff}\right)\right]^2}{\sigma_w^2}\left(M-1\right) & \text{for} \quad \text{PPM} \\ \frac{\left[P_r\left(h_{eff}\right)\right]^2}{\sigma_w^2}\frac{(M+1)}{3(M-1)} & \text{for} \quad \text{PAM}\end{cases}. \tag{107}$$

Since the modulation size and transmit power are changed according to the channel conditions in AMPA, we denote them as a function of the channel condition, i.e., namely $M\left(h_{eff}\right)$ and $P_t\left(h_{eff}\right)$ in the following. In AMA-1 and AMA-2, the only adjustable parameter is $M\left(h_{eff}\right)$while the transmit power is constant.

In adaptive system design, we adopt three performance measures. The first one is the *spectral efficiency.* For PPM and PAM, the spectral efficiency is respectively given as $R\left(h_{eff}\right) = \log_2[M\left(h_{eff}\right)]/M\left(h_{eff}\right)$ and $R\left(h_{eff}\right) = \log_2[M\left(h_{eff}\right)]$ (bits/s/Hz) [75]. The second performance measure is the *outage probability.* An outage is defined as an event that the channel does not support a target data rate, or in other words, when the instantaneous/conditioned channel capacity is less than the target data rate. The third performance measure is related to *power consumption.* Lifetime of the laser and eye safety standards impose some constraints on the average and peak optical transmission power. The latter is particularly important for FSO applications where eye safety standards impose restrictions on the peak of the transmit power. The constraint on average power can be expressed as

$$\begin{aligned}P_{ot} &= E\left[\sum_{i=1}^{n_t} P_t^i\left(h_{eff}\right)\right] \\ &= \int_0^\infty P_t\left(h_{eff}\right) f_{h_{eff}}\left(h_{eff}\right) dh_{eff} \leq P_{ot,\max}\end{aligned} \tag{108}$$

Here, P_{ot} is the expected value of average transmit power with respect to the distribution of h_{eff} and $P_{ot,\max}$ is the bound on average power. Recall that P_t earlier defined in Section 5.1 represents the average optical transmit power per symbol duration. The peak transmit power is bounded as

$$P_{pt} = \begin{cases} P_t\left(h_{eff}\right) \leq P_{pt,\max} & \text{for} \quad \text{PPM} \\ 2P_t\left(h_{eff}\right) \leq P_{pt,\max} & \text{for} \quad \text{PAM} \end{cases} \tag{109}$$

where $P_{pt,\max}$ is the bound on peak power.

5.2.1 Adaptive Modulation Algorithm-1 (AMA-1)

In this algorithm, we aim to maximize spectral efficiency by adaptively changing the PPM size under power constraints. The average transmit power is fixed for each signaling interval, therefore we simply have $P_{ot} = P_t \leq P_{ot,\max}$ and $P_{pt} = P_t \leq P_{pt,\max}$. In an FSO system, we typically have $P_{ot,max} < P_{pt,\max}$ and hence we can write $P_t = P_{ot,\max}$. We aim to keep the outage probability less than a pre-specified value ε. To maximize the instantaneous spectral efficiency, we formulate the problem as

$$\begin{aligned} & M' = \arg \max_{M\left(h_{eff}\right)} R\left(h_{eff}\right) = \arg \max_{M\left(h_{eff}\right)} \frac{log_2\left(M\left(h_{eff}\right)\right)}{M\left(h_{eff}\right)} \\ & \text{s.t.} \\ & \quad 1) \quad P_{out}\left(R\left(h_{eff}\right), \bar{\rho}\right) < \varepsilon \\ & \quad 2) \quad M\left(h_{eff}\right) = \begin{cases} 2 & \text{if} \quad P_1 \leq P_r\left(h_{eff}\right) \\ 2^n & \text{if} \quad P_n \leq P_r\left(h_{eff}\right) < P_{n-1} \end{cases} \\ & \quad 3) \quad P_t = P_{ot,\max} \end{aligned} \tag{110}$$

where M' is the optimal value of modulation size in each signaling interval. Here P_n, $n = 1, 2, ..., \log_2\left(M_{PPM}^{\max}\right)$ denote switching thresholds between different transmission modes, i.e., different modulation sizes of PPM, and $M_{PPM}^{\max}$ is the maximum allowable modulation order (see Appendix C) to satisfy a pre-defined outage probability. Considering that $log_2\left(M\left(h_{eff}\right)\right)/M\left(h_{eff}\right)$ in (110) is monotonically decreasing, maximizing the spectral efficiency in (110) is equivalent to selecting the minimum modulation size, i.e., $M\left(h_{eff}\right)$, in each interval that meets the constraints.

Let C_{th} =0.5 $\log\left(1+\rho\left(h_{eff}\right)\right)$ denote the highest conditional channel capacity (conditioned on fading coefficient) for MISO system that is acceptable by the system for a fixed SNR. The outage probability is $P_{out}\left(R\left(h_{eff}\right),\bar{\rho}\right)=\Pr\left\{R\left(h_{eff}\right)>C_{th}\right\}$ (see Appendix B for derivation details[1]). First note that we must have $R\left(h_{eff}\right)<C_{th}$ to prevent outage. Therefore, we can write

$$R\left(h_{eff}\right)<\frac{1}{2}\log_2\left[1+\rho\left(h_{eff}\right)\right]. \tag{111}$$

We replace (107) in (111) and replace $R\left(h_{eff}\right)=\log_2[M\left(h_{eff}\right)]/M\left(h_{eff}\right)$ in the resulting expression. This yields a lower bound on the instantaneous received power as

$$P_r\left(h_{eff}\right)>\sigma_w\left[\frac{\left([M\left(h_{eff}\right)]^{2/M\left(h_{eff}\right)}-1\right)}{M\left(h_{eff}\right)-1}\right]^{1/2}. \tag{112}$$

Next, we consider the second constraint in (110) which dictates the discreteness of modulation size. Replacing each value of modulation size in (112), it provides a specific region for the received power. Therefore, the minimization problem reduces to choosing the minimum value of modulation size in each region. Finally, the maximization problem in (110) reduces to

$$M'=\begin{cases}\text{BPPM} & \sigma_w\leq P_r\left(h_{eff}\right)\\ 2^n\text{-PPM} & \sigma_w\sqrt{\frac{2^{\frac{2n}{2^n}}-1}{2^n-1}}\leq P_r\left(h_{eff}\right)<\sigma_w\sqrt{\frac{2^{\frac{2(n-1)}{2^{n-1}}}-1}{2^{n-1}-1}}\end{cases}. \tag{113}$$

Paying attention to the intervals in (113), the switching thresholds are determined as

$$P_n=\sigma_w\left(\frac{2^{2n/2^n}-1}{2^n-1}\right)^{1/2}\quad\text{for}\quad n=1,2,...,log_2\left(M_{PPM}^{\max}\right). \tag{114}$$

In the light of above descriptions, the algorithm flow is provided in Fig. 27a.

[1] Here, without loss of generality, we only consider MISO system. The outage results can be easily extended for SIMO system. We avoid repeating the same derivations for SIMO system; instead, we discuss and compare the numerical results in Section 5.4.

5.2.2 Adaptive Modulation Algorithm-2 (AMA-2)

In this algorithm, we consider both PPM and PAM as modulation types. This aims to exploit high spectral efficiency of PAM and also high reliability of PPM whenever needed. As discussed earlier, we have $P_{ot} = P_t \leq P_{ot,\max}$ and $P_{pt} = P_t \leq P_{pt,\max}$ for PPM. For PAM, we have $P_{ot} = P_t \leq P_{ot,\max}$ and $P_{pt} = 2P_t \leq P_{pt,\max}$. We can therefore write $P_t = \min\{P_{ot,\max}, 0.5P_{pt,\max}\}$. For a typical FSO system, we can assume $P_{ot,max} < 0.5P_{pt,\max}$ and hence we have $P_t = P_{ot,\max}$. To maximize the instantaneous spectral efficiency, we formulate the problem as

$$
\begin{aligned}
M' = \arg \max_{M(h_{eff})} & \begin{cases} log_2\left(M\left(h_{eff}\right)\right)/M\left(h_{eff}\right) & \text{for} \quad \text{PPM} \\ log_2\left(M\left(h_{eff}\right)\right) & \text{for} \quad \text{PAM} \end{cases} \\
\text{s.t.} & \\
& 1) \quad P_{out}\left(R\left(h_{eff}\right), \bar{\rho}\right) < \varepsilon \\
& 2) \quad M\left(h_{eff}\right) = \begin{cases} 2^n\text{-PAM} & \text{if} \quad {P'}_n \leq P_r\left(h_{eff}\right) < {P'}_{n+1} \\ 2\text{-PAM} & \text{if} \quad {P'}_1 \leq P_r\left(h_{eff}\right) < {P'}_2 \\ 2\text{-PPM} & \text{if} \quad P_1 \leq P_r\left(h_{eff}\right) < {P'}_1 \\ 2^n\text{-PPM} & \text{if} \quad P_n \leq P_r\left(h_{eff}\right) < P_{n-1} \end{cases} \\
& 3) \quad P_t = P_{ot,\max}
\end{aligned}
\tag{115}
$$

where ${P'}_n$'s, $n = 1, 2, ..., \log_2\left(M_{PAM}^{\max}\right)$ are switching thresholds between transmission modes for PAM while P_n's, $n = 1, 2, ..., \log_2\left(M_{PPM}^{\max}\right)$ are defined for PPM. ${P'}_1$ also serves as the threshold for switching between PPM and PAM schemes. Following similar steps as in the previous section, the above maximization problem reduces to

$$
M' = \begin{cases} 2^n\text{-PAM} & \sqrt{3}\sigma_w\left[2^n - 1\right] \leq P_r\left(h_{eff}\right) < \sqrt{3}\sigma_w\left[2^{n+1} - 1\right] \\ \text{OOK} & \sqrt{3}\sigma_w \leq P_r\left(h_{eff}\right) < 3\sqrt{3}\sigma_w \\ \text{BPPM} & \sigma_w \leq P_r\left(h_{eff}\right) < \sqrt{3}\sigma_w \\ 2^n\text{-PPM} & \sigma_w\sqrt{\frac{2^{\frac{2n}{2^n}}-1}{2^n-1}} \leq P_r\left(h_{eff}\right) < \sigma_w\sqrt{\frac{2^{\left[\frac{2(n-1)}{2^{n-1}}\right]}-1}{2^{n-1}-1}} \end{cases}
\tag{116}
$$

This can be further written as

$$M' = \begin{cases} 2^n\text{-PAM} \; P'_{n+1}/\left(\eta L P_{ot,\max}\right) > h_{eff} \geq P'_n/\left(\eta L P_{ot,\max}\right) \\ \text{OOK} \qquad P'_2/\left(\eta L P_{ot,\max}\right) > h_{eff} \geq P'_1/\left(\eta L P_{ot,\max}\right) \\ \text{BPPM} \qquad P'_1/\left(\eta L P_{ot,\max}\right) > h_{eff} \geq P_1/\left(\eta L P_{ot,\max}\right) \\ 2^n\text{-PPM} \quad P_{n-1}/\left(\eta L P_{ot,\max}\right) > h_{eff} \geq P_n/\left(\eta L P_{ot,\max}\right) \end{cases} \tag{117}$$

where

$$P'_n = \sqrt{3}\sigma_w\left(2^n - 1\right) \;,\; n = 1, 2, ..., log_2\left(M_{PAM}^{\max}\right) \tag{118}$$

are the switching thresholds for PAM transmission modes. The switching thresholds for PPM transmission modes, i.e. P_n's, remain the same as in (114).

The algorithm flow diagram of this algorithm is presented in Fig. 27b. It basically remains the same as AMA-1 with some modifications. Specifically, the rate optimization is now based on (115) and the switching thresholds between PAM transmission modes are further included.

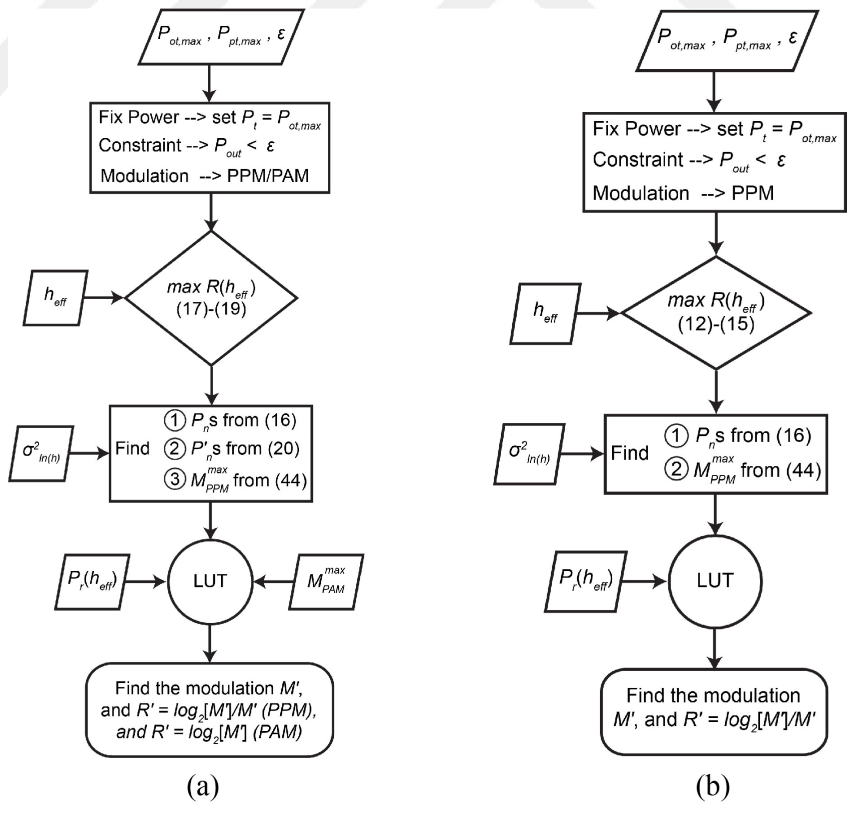

Figure 27: Algorithm flow diagram of a) AMA-1 and b) AMA-2.

5.2.3 Adaptive Modulation and Power Algorithm (AMPA)

In this scheme, we aim to maximize spectral efficiency by adaptively changing both transmit power and modulation size of PPM/PAM according to channel conditions while keeping the outage probability equal to ε.

Considering the transmit power as a function of channel condition, i.e. $P_t\left(h_{eff}\right)$, we must have at least $R\left(h_{eff}\right) = C_{th}$ to prevent the outage event. Therefore, $\rho\left(h_{eff}\right)$ is obtained as

$$\rho\left(h_{eff}\right) = \left(2^{2R\left(h_{eff}\right)} - 1\right). \tag{119}$$

Noting $\rho\left(h_{eff}\right) = \bar{\rho} h_{eff}^2$ and using (105) and (106), we can find $P_t\left(h_{eff}\right)$ as

$$P_t\left(h_{eff}\right) = \frac{\sigma_w}{h_{eff}\eta L}\sqrt{K_1\left(M\right)} \tag{120}$$

where $K_1\left(M\right)$ is given by

$$K_1\left(M\right) = \begin{cases} \frac{\left(M^{2/M}-1\right)}{(M-1)} & \text{for} \quad \text{PPM} \\ 3(M-1)^2 & \text{for} \quad \text{PAM} \end{cases} \tag{121}$$

For small values of h_{eff}, $P_t\left(h_{eff}\right)$ may violate peak power constraint. To avoid this, we apply peak power constraints, i.e., $P_t\left(h_{eff}\right) \leq P_{pt,\max}$ for PPM (c.f. section 5.2.1) and $2P_t\left(h_{eff}\right) \leq P_{pt,\max}$ for PAM (c.f. section 5.2.2). Then, we find a threshold on the value of h_{eff}, i.e., $h_{eff} \geq th_M$ to determine the switching threshold where a transmission mode switches to a lower spectral-efficient modulation with higher reliability. This is defined as

$$th_M^r = \frac{\sigma_w}{P_{pt,\max}\eta L}\sqrt{K_2\left(M\right)} \tag{122}$$

where $r \in \{\text{PAM,PPM}\}$ and $K_2\left(M\right)$ is given by

$$K_2\left(M\right) = \begin{cases} \frac{\left(M^{2/M}-1\right)}{(M-1)} & \text{for} \quad \text{PPM} \\ 12(M-1)^2 & \text{for} \quad \text{PAM} \end{cases} \tag{123}$$

Therefore, we can write (120) as

$$P_t\left(h_{eff}\right) = \begin{cases} \frac{\sigma_w}{h_{eff}\eta L}\sqrt{K_1\left(M\right)} & h_{eff} \geq th_M^r \\ \frac{\sigma_w}{h_{eff}\eta L}\sqrt{K_1\left(\hat{M}\right)} & h_{eff} < th_M^r \end{cases} \tag{124}$$

where $\hat{M}$ is the second highest spectral-efficient modulation under consideration, i.e., $\hat{M} = 2M$, for PPM and $\hat{M} = M/2$ for PAM. The average power constraint should also be conserved. The switching thresholds th_M^r divides the region of h_{eff} into different intervals assigned to one transmission scheme. Therefore, the average power constraint in (108) can be written as

$$\begin{aligned} P_{ot} &= \int\limits_{0}^{\infty} P_t\left(h_{eff}\right) f_{h_{eff}}\left(h_{eff}\right) dh_{eff} \\ &= \sum_{M} \int\limits_{th_M^r} P_t\left(h_{eff}\right) f_{h_{eff}}\left(h_{eff}\right) dh_{eff} \end{aligned} \tag{125}$$

Considering having th_M^r, $r \in \{\text{PAM,PPM}\}$ as the switching thresholds, it can be noted from (122) that we always have $th_M^{PAM} > th_M^{PPM}$ and th_M^{PAM} is an increasing function of M, while th_M^{PPM} is a decreasing function of M. Therefore, we can divide the integral region in (125) as

$$P_{ot} = \sum_{M=M_{PPM}^{\max}}^{2} P_{ot}^{PPM}\left(M\right) + \sum_{M=2}^{M_{PAM}^{\max}} P_{ot}^{PAM}\left(M\right) \tag{126}$$

where $P_{ot}^{PPM}\left(M\right)$ and $P_{ot}^{PAM}\left(M\right)$ are average powers within one interval assigned to M for PPM and PAM schemes respectively. Using (124), we can write $P_{ot}^{PPM}\left(M\right)$ and $P_{ot}^{PAM}\left(M\right)$ as

$$\begin{aligned} P_{ot}^{PPM}\left(M\right) &= \int\limits_{th_M^{PPM}}^{th_{M/2}^{PPM}} \frac{\sigma_w}{\eta L h_{eff}} \sqrt{\frac{\left(M^{\frac{2}{M}}-1\right)}{(M-1)}} f_{h_{eff}}\left(h_{eff}\right) dh_{eff} \\ &= P_{pt,\max} th_M^{PPM} \int\limits_{th_M^{PPM}}^{th_{M/2}^{PPM}} \frac{1}{h_{eff}} f_{h_{eff}}\left(h_{eff}\right) dh_{eff} \end{aligned} \tag{127}$$

$$\begin{aligned} P_{ot}^{PAM}\left(M\right) &= \int\limits_{th_{M/2}^{PAM}}^{th_M^{PAM}} \frac{\sigma_w}{\eta L h_{eff}} \sqrt{3(M-1)^2} f_{h_{eff}}\left(h_{eff}\right) dh_{eff} \\ &= \frac{P_{pt,\max} th_M^{PAM}}{2} \int\limits_{th_{M/2}^{PAM}}^{th_M^{PAM}} \frac{1}{h_{eff}} f_{h_{eff}}\left(h_{eff}\right) dh_{eff} \end{aligned} \tag{128}$$

where we used the definition of th_M^r, $r \in \{\text{PAM,PPM}\}$ in (122).

The derivation of the integrals in (127) and (128) is provided in the Appendix D. It is seen that P_{ot} is an increasing function of $M_{PAM}^{\max}$, therefore, the constraint $P_{ot} \leq P_{ot,\max}$ determines the maximum modulation order of PAM scheme, i.e., $M_{PAM}^{\max}$. If $P_{ot,max}$ is small enough that $P_{ot} \leq P_{ot,\max}$ does not hold for any PAM modulation order, then we need to consider the minimum PPM modulation order, i.e., $M_{PPM}^{\min}$. In this case, adaptive system reduces to only PPM scheme. To avoid this, we assume that the value of $P_{ot,\max}$ is sufficiently high and that it holds for at least one M_{PAM}. Clearly, the outage occurs when $h_{eff} < th_{M_{PPM}^{\max}}$ and this imposes a constraint on $M_{PPM}^{\max}$ whose calculation is provided in the Appendix C.

To maximize the spectral efficiency, we should find the maximum value of M (denoted by M') that satisfies the constraints. Hence, we formulate the problem as

$$
\begin{aligned}
& M' = \arg \max_{M\left(h_{eff}\right)} R\left(h_{eff}\right) \\
& \text{s.t.} \\
& \quad 1)\ \ P_t\left(h_{eff}\right) = \frac{\sigma_w}{h_{eff}\eta L}\sqrt{K_1\left(M\right)}\ h_{eff} \geq th_M \\
& \quad 2)\ \ M\left(h_{eff}\right) = \begin{cases} 2^n\text{-PAM} & \text{if} \quad P'_n \leq P_r\left(h_{eff}\right) < P'_{n+1} \\ 2\text{-PAM} & \text{if} \quad P'_1 \leq P_r\left(h_{eff}\right) < P'_2 \\ 2\text{-PPM} & \text{if} \quad P_1 \leq P_r\left(h_{eff}\right) < P'_1 \\ 2^n\text{-PPM} & \text{if} \quad P_n \leq P_r\left(h_{eff}\right) < P_{n-1} \end{cases} \\
& \quad 3)\ \ M_{PPM}^{\max} \text{ is found from Appendix C.} \\
& \quad 4)\ \ M_{PAM}^{\max} \text{ is found from Appendix D.}
\end{aligned}
\tag{129}
$$

The switching thresholds, P_n and P'_n, can be found by replacing $h_{eff} = th_M$ in (124) and calculating the received power, i.e. $P_n = \eta L P_T\left(th_M\right) th_M$. The switching thresholds are found as

$$P_n = \sigma_w \left(\frac{2^{\frac{2n}{2^n}} - 1}{2^n - 1} \right)^{1/2} \qquad \text{for PPM} \tag{130}$$

$$P'_n = \sqrt{3}\sigma_w\left(2^n - 1\right) \qquad \text{for PAM} \tag{131}$$

It can be noticed from (130) and (131) that the switching thresholds are the same as the ones in (116). It should be however noted that power is adaptively changed in AMPA. Hence, it is not fair to compare AMPA with AMA-2 and AMA-1 in terms of received power. Alternatively, we can compare the schemes with respect to channel condition h_{eff}. A better scheme is supposed to provide higher data rate at worse channel conditions (i.e., lower values of h_{eff}). From (122), we have switching thresholds of $c_n = th_{M=2^n}^{PPM}$ for PPM and $c'_n = th_{M=2^n}^{PAM}$ for PAM given as

$$c_n = \frac{\sigma_w}{\eta L P_{pt,\max}} \left(\frac{2^{2n/2^n} - 1}{2^n - 1} \right)^{1/2} = \frac{P_n}{\eta L P_{pt,\max}} \qquad \text{for PPM} \tag{132}$$

$$c'_n = 2\sqrt{3} \frac{\sigma_w}{\eta L P_{pt,\max}} \left(2^n - 1 \right) = \frac{P'_n}{0.5 \eta L P_{pt,\max}} \qquad \text{for PAM} \tag{133}$$

Therefore, the maximization problem in (129) reduces to

$$M' = \begin{cases} 2^n\text{-PAM} & \frac{P'_n}{(0.5\eta L P_{pt,\max})} \le h_{eff} < \frac{P'_{n+1}}{(0.5\eta L P_{pt,\max})} \\ \text{OOK} & \frac{P'_1}{(0.5\eta L P_{pt,\max})} \le h_{eff} < \frac{P'_2}{(0.5\eta L P_{pt,\max})} \\ \text{BPPM} & \frac{P_1}{(\eta L P_{pt,\max})} \le h_{eff} < \frac{P'_1}{(0.5\eta L P_{pt,\max})} \\ 2^n\text{-PPM} & \frac{P_n}{(\eta L P_{pt,\max})} \le h_{eff} < \frac{P_{n-1}}{(\eta L P_{pt,\max})} \end{cases} \tag{134}$$

The optimized transmit power for adaptive scheme can be found by replacing M' in (124). The algorithm flow steps are summarized in Fig. 28.

5.3 Average Achievable Spectral Efficiency

As discussed in the previous section, the aim of the proposed adaptive schemes is to maximize the instantaneous spectral efficiency denoted by $R(h_{eff})$. However, in order to compare the performance of proposed adaptive schemes in different turbulence statistics, *average achievable spectral efficiency* (average data rate in a given bandwidth) will be a more proper metric. Mathematically speaking, this will be given by

$$\bar{R} = \frac{S}{W} = E_{h_{eff}} \left[R\left(h_{eff} \right) \right] \qquad \text{(bits/sec/Hz)} \tag{135}$$

where S denotes the transmission data rate.

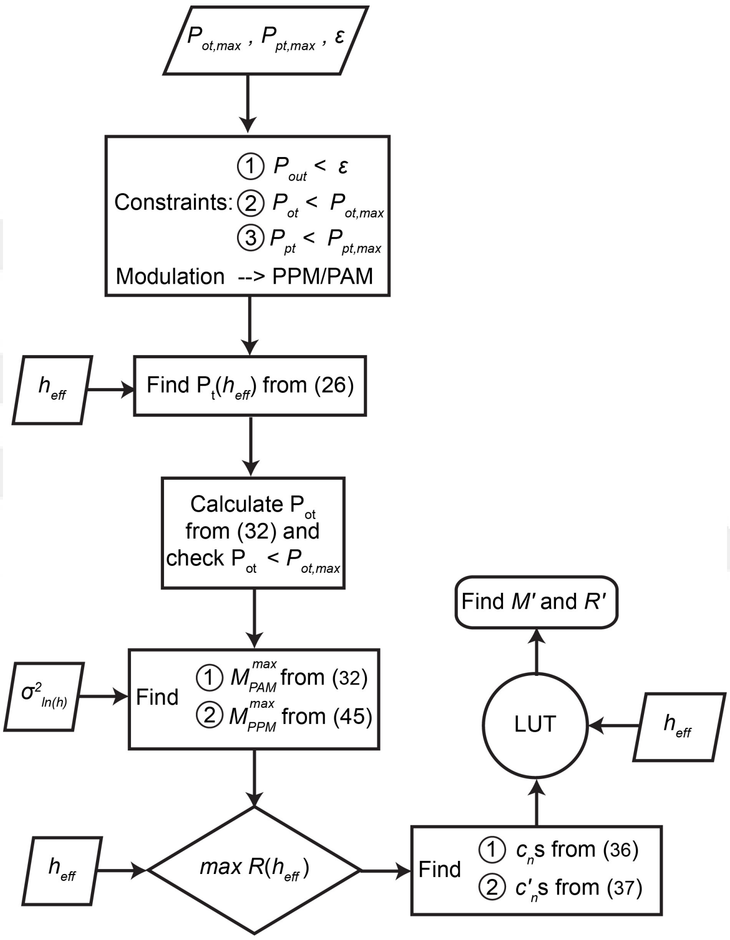

Figure 28: Algorithm flow diagram of AMPA.

5.3.1 AMA-1

For AMA-1, we can write the average achievable spectral efficiency as

$$\bar{R} = \sum_{n=1}^{N} \Pr\left\{c_n < h_{eff} < c_{n-1}\right\} \frac{\log_2(M_n)}{M_n} \tag{136}$$

where $N = log_2\left(M_{PPM}^{\max}\right)$ and the thresholds are given by

$$c_n = \frac{P_n}{\eta L P_{ot,\max}} = \frac{1}{P_M}\left(\frac{2^{\frac{2n}{2^n}} - 1}{2^n - 1}\right)^{1/2} \tag{137}$$

In (137), power margin is defined as $P_M = \eta L P_{ot,\max}/\sigma_w$. Note that $M_{PPM}^{\max}$, and consequently N, are functions of P_M and pre-specified outage probability of ε. Replacing $M_n = 2^n$ in (136) and writing it in term of the pdf of h_{eff}, we have

$$\begin{aligned}\bar{R} &= \sum_{n=1}^{N} \frac{n}{2^n} \int_{c_n}^{c_{n-1}} f_{h_{eff}}(h_{eff})\, dh_{eff} \\ &= \sum_{n=1}^{N} \frac{n}{2^n}\left[F_{h_{eff}}(c_{n-1}) - F_{h_{eff}}(c_n)\right]\end{aligned} \tag{138}$$

where $F_{h_{eff}}(\cdot)$ is the cumulative density function (CDF) of h_{eff}. Note that $c_0 \to \infty$ and therefore $F_{h_{eff}}(c_0) \to 1$. Similarly, we have $c_N \to 0$ implying that $F_{h_{eff}}(c_N) \to 0$. Therefore, (138) reduces to

$$\bar{R} = \frac{1}{2} - \sum_{n=1}^{N-1} \frac{n-1}{2^{n+1}} F_{h_{eff}}(c_n) \tag{139}$$

From (139), it is observed that 0.5 bit/sec/Hz is the maximum achievable rate by PPM. Using the derived expressions for the CDF of h_{eff} in Appendix B, we obtain the average achievable spectral efficiency of AMA-1 over LN and GG turbulence fading channels as

$$\bar{R} = \frac{1}{2} - \sum_{n=1}^{N-1} \frac{n-1}{2^{n+1}} Q\left(-\frac{1}{2\sigma_u}\ln(c_n) - \frac{\sigma_u}{2}\right) \quad \text{for LN} \tag{140a}$$

$$\bar{R} = \frac{1}{2} - \sum_{n=1}^{N-1} \frac{n-1}{2^{n+1}} \frac{\Gamma\left(\nu, \nu\kappa c_n^{\tau}/\hat{\omega}^{\tau}\right)}{\Gamma(\nu)} \quad \text{for GG} \tag{140b}$$

where the definition of parameters σ_u, ν, τ and $\hat{\omega}$ can be found in Appendix B.

5.3.2 AMA-2

In this algorithm, the ordering of adaptive scheme starts from lowest spectral efficiency which is the maximum order of PPM. Then it moves toward BPPM and then OOK. Finally, it increases to the maximum order of PAM. Therefore, we can write the average achievable spectral efficiency as

$$\begin{aligned}\bar{R} &= \sum_{n=1}^{N} \Pr\left\{c_n < h_{eff} < c_{n-1}\right\} \frac{\log_2\left(M_n\right)}{M_n} \\ &+ \sum_{n=1}^{N'} \Pr\left\{c'_n < h_{eff} < c'_{n+1}\right\} \log_2\left(M_n\right)\end{aligned} \tag{141}$$

where $N = log_2\left(M_{PPM}^{\max}\right)$ and $N' = log_2\left(M_{PAM}^{\max}\right)$. Here, c_n is as defined in (137) while the PAM thresholds are given by

$$c'_n = \frac{P'_n}{\eta L P_{ot,\max}} = \frac{\sqrt{3}\left(2^n - 1\right)}{P_M} \tag{142}$$

Replacing $M_n = 2^n$ in (141) and writing the resulting expressions in terms of the CDF of h_{eff}, we obtain

$$\begin{aligned}\bar{R} &= \sum_{n=1}^{N} \frac{n}{2^n}\left[F_{h_{eff}}\left(c_{n-1}\right) - F_{h_{eff}}\left(c_n\right)\right] \\ &+ \sum_{n=1}^{N'} n\left[F_{h_{eff}}\left(c'_{n+1}\right) - F_{h_{eff}}\left(c'_n\right)\right]\end{aligned} \tag{143}$$

Note that, unlike AMA-1, c_0 is not unbounded and it is basically determined by the threshold that the adaptive strategy switches from PPM to PAM (i.e., $c_0 = c'_1$). Therefore, $F_{h_{eff}}\left(c_0\right) = F_{h_{eff}}\left(c'_1\right)$. Similarly we have $c_N \to 0$ and $c'_{N'+1} \to \infty$ implying that $F_{h_{eff}}\left(c_N\right) \to 0$ and $F_{h_{eff}}\left(c'_{N'+1}\right) \to 1$, respectively. Consequently, (143) reduces to

$$\bar{R} = N' - \sum_{n=1}^{N-1} \frac{n-1}{2^{n+1}} F_{h_{eff}}\left(c_n\right) - \frac{1}{2} F_{h_{eff}}\left(c'_1\right) - \sum_{n=2}^{N'} F_{h_{eff}}\left(c'_n\right) \tag{144}$$

From (144), it can be observed that $N' = log_2\left(M_{PAM}^{\max}\right)$ bit/sec/Hz is the maximum achievable rate by AMA-2. Using the derived expressions for the CDF of h_{eff} in Appendix B, we can write the average achievable spectral efficiency over LN and

GG turbulence fading channels respectively as

$$\bar{R} = N' - \sum_{n=1}^{N-1} \frac{n-1}{2^{n+1}} Q\left(\frac{-1}{2\sigma_u}\ln\left(c_n\right) - \frac{\sigma_u}{2}\right) \tag{145a}$$
$$- \frac{1}{2} Q\left(\frac{-1}{2\sigma_u}\ln\left({c'}_1\right) - \frac{\sigma_u}{2}\right) - \sum_{n=2}^{N'} Q\left(\frac{-1}{2\sigma_u}\ln\left({c'}_n\right) - \frac{\sigma_u}{2}\right)$$

$$\bar{R} = N' - \sum_{n=1}^{N-1} \frac{n-1}{2^{n+1}} \frac{\Gamma\left(\nu, \nu\kappa c_n^{\tau}/\hat{\omega}^{\tau}\right)}{\Gamma\left(\nu\right)} \tag{145b}$$
$$- \frac{1}{2} \frac{\Gamma\left(\nu, \nu\kappa {c'_1}^{\tau}/\hat{\omega}^{\tau}\right)}{\Gamma\left(\nu\right)} - \sum_{n=2}^{N'} \frac{\Gamma\left(\nu, \nu\kappa {c'_n}^{\tau}/\hat{\omega}^{\tau}\right)}{\Gamma\left(\nu\right)}$$

where the definition of parameters σ_u, ν, τ and $\hat{\omega}$ can be found in Appendix B.

5.3.3 AMPA

The average achievable spectral efficiency of AMPA algorithm has a similar form of that of AMA-2 algorithm. Mathematically speaking, it is given by (145) where the values of switching thresholds c_n and ${c'}_n$ should be calculated from (132) and (133).

5.4 Numerical Results

In this section, we present simulation results to collaborate analytical derivations. We consider an operating wavelength of $\lambda = 1550$ nm and refractive-index structure constant $C_n^2 = 3.5 \times 10^{-14}$ m$^{2/3}$. We consider $d = 1$ km. We set the outage probability threshold as $\varepsilon = 10^{-7}$. We further assume noise power of $\sigma_w = 10^{-4}$, visibility $V = 10$ km, receiver aperture diameter $D_r = 10$ cm, beam divergence angle of $\theta_{tx} = 3$ mrad, average power bound of $P_{ot,\max} = 100$ mW, and maximum allowable peak power of $P_{pt,\max} = 800$ mW [115].

First, we present comparisons of adaptive algorithms using *instantaneous* spectral efficiency based on the derivations in Section 5.2. It should be emphasized that adaptive algorithms change the parameters according to the instantaneous value of fading channel coefficient (i.e., based on a realization of fading channel) and therefore the optimal data rates obtained in (113), (116), and (134) are obviously independent of the channel statistics.

In Fig. 29, we plot the instantaneous spectral efficiency of AMA-1 and AMA-2 for MISO/SIMO FSO systems with respect to instantaneous received power based on (113) and (116) respectively. From (168) of Appendix C, to maintain an outage of $\varepsilon = 10^{-7}$, $M_{PPM}^{\max}$ are calculated as 2, 16, and 32 for SIMO, MISO, and SISO systems respectively. From Fig. 29, it is observed that, in the MISO system with AMA-2, 4-PAM is employed for $P_r\left(h_{eff}\right) \geq -2.84$ dBm achieving a spectral efficiency of 2 bits/sec/Hz. When received power is less than -2.84 dB, the system switches to 2-PAM (OOK) with spectral efficiency of 1 bits/sec/Hz. For the range of $-12.38 \leq P_r\left(h_{eff}\right) \leq -7.62$ dB, 2-PPM/4-PPM is employed with spectral efficiency of 0.5 bits/sec/Hz. On the other hand, it is observed that SIMO system with AMA-2 system employs 16-PAM, 8-PAM and 2-PPM/4-PPM, respectively, for received power ranges of $P_r\left(h_{eff}\right) \geq -1.87$ dB, $-5.19 \leq P_r\left(h_{eff}\right) \leq -1.87$ and $-18.38 \leq P_r\left(h_{eff}\right) \leq -13.64$. Therefore, spectral efficiency of 4, 3, and 0.5 bits/sec/Hz are respectively obtained. In SIMO and MISO system, -13.64 dB and -7.62 dB are respectively found to be the threshold values where the AMA-2 algorithm switches from PAM to PPM. This indicates a power improvement gain of almost 6 dB in favor of SIMO system.

Comparison of AMA-1 and AMA-2 plots reveals that the maximum spectral efficiency that can be achieved by AMA-1 is limited to 0.5 bits/s/Hz. However, AMA-2 based on the joint use of PPM and PAM, gives the flexibility to cover more transmission modes and achieves higher spectral efficiencies. The existence of different PPM modulation orders makes it possible to achieve higher reliability at low power values where the channel experiences adverse conditions.

In Fig. 30, we plot the instantaneous spectral efficiency of AMPA and compare it with AMA-2. As earlier discussed in Section 5.2.3, since it is unfair to make comparisons with respect to power, we present the spectral efficiency with respect to h_{eff}, see (117) and (134). The h_{eff} values in Fig. 30 are given in dB meaning

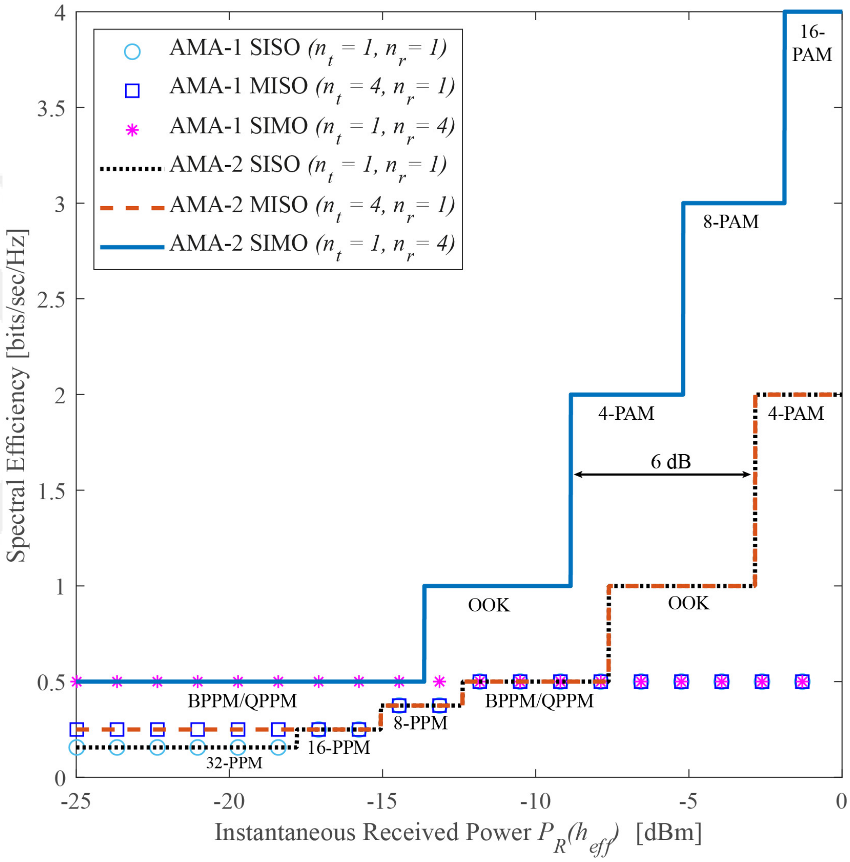

Figure 29: Instantaneous spectral efficiencies of proposed adaptive algorithm AMA-1 and AMA-2.

that $h_{eff} = 0$ dB (i.e., $h_{eff} = 1$) is the mean value of the channel fading coefficient. This indicates $h_{eff} > 0$ dB (i.e., $h_{eff} > 1$) amplifies the signal and $h_{eff} < 0$ dB (i.e., $0 < h_{eff} < 1$) attenuates the signal. As expected, AMPA outperforms AMA-2 due to the additional flexibility given by power control. Specifically, for MISO system, a rate of 0.5 bits/s/Hz is achieved for AMA-2 while it increases to 1 bits/s/Hz for AMPA assuming $h_{eff} = -2$ dB. For SIMO system, this changes to 1 bits/s/Hz for AMA-2 and 2 bits/s/Hz for AMPA. This improvement comes from the fact that AMPA tries to compensate the power loss due to channel fading fluctuations by supplying more power but limited to $P_{pt,\max}$. In this way, the modulation order and rate can be kept at higher values. Finally, comparing MISO and SIMO systems, it can be concluded that SIMO system with AMPA gives the best performance among others. SIMO system with AMPA outperforms MISO system with AMA-2 by a gain of 12 dB where 6 dB of this comes from the use of receive apertures and another 6 dB from the power gain of AMPA.

In the following, we demonstrate the effect of turbulence on the performance of proposed algorithms. For this purpose, we use *average* achievable spectral efficiency which was obtained through the expectation over relevant channel statistics (see Section 5.3). For LN turbulence channel, we assume a Rytov variance of $\sigma_R^2 = 0.7$ (weak/medium turbulence) for $d = 1$ km. For GG turbulence channel, we assume a Rytov variance of $\sigma_R^2 = 5$ and scintillation index of $\sigma_h^2 = 3.33$ with parameters of $\alpha = 0.69$ and $\beta = 1.30$. As an example, we consider SIMO ($n_t = 1$, $n_r = 4$) case.

In Fig. 31 and 32, we plot the average achievable spectral efficiency ($\bar{R}$) of AMA-1, AMA-2, and AMPA versus power margin (P_M) based on (140) and (145). It is worth mentioning that unlike instantaneous spectral efficiencies with staircase characteristics (see Figs. 29 and 30), the average spectral efficiencies are continuous. The reason is that for instantaneous spectral efficiencies, the algorithm switches at each interval region of channel fading coefficient. However, in the

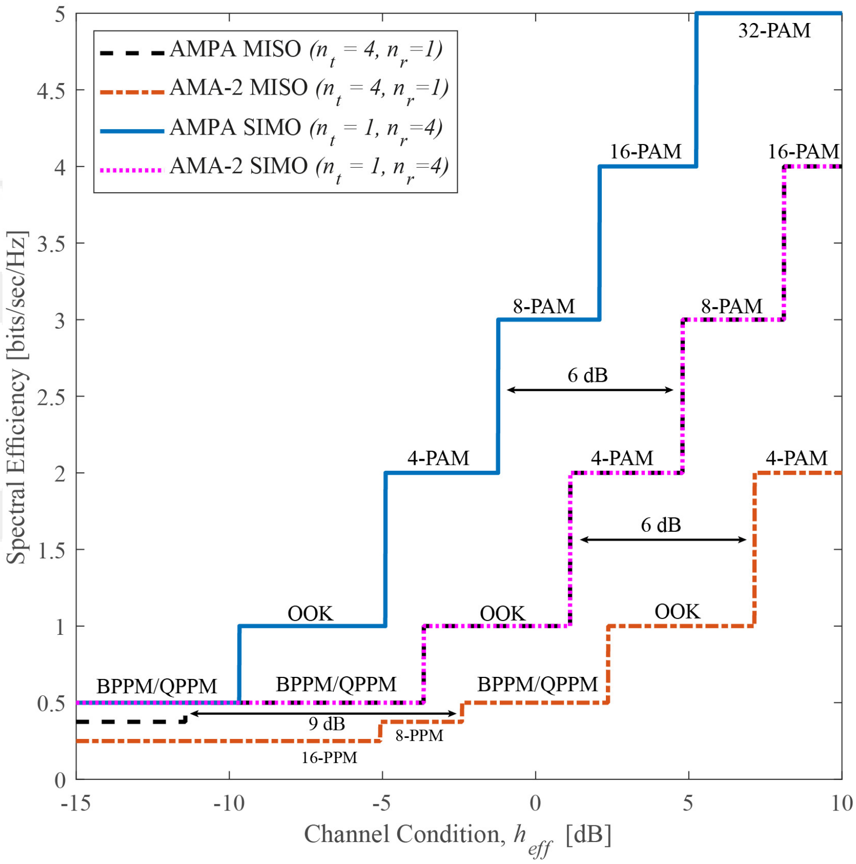

Figure 30: Instantaneous spectral efficiencies of proposed adaptive algorithm AMPA and comparison with AMA-2.

calculation of average spectral efficiencies, averaging is performed over the channel statistics and therefore the resulting plots have continuous characteristics. It should be further noted that the average spectral efficiency of non-adaptive system (included as a benchmark in Fig. 31 and 32) still shows staircase format since its spectral efficiency is fixed independent of the channel statistics. In the non-adaptive system, we choose the highest rate that satisfies the predefined outage probability of less than $\varepsilon = 10^{-7}$ for each value of P_M.

From Fig. 31 presented for LN turbulence channel, it is observed that non-adaptive system provides more efficiency than AMA-1 for high power margins. However, this is not the case for AMA-2 and AMPA, and they always outperform the non-adaptive case by employing PAM scheme. From Fig. 32 presented for GG turbulence channel, it can be observed that the efficiency of non-adaptive case is very poor. This is expected due to strong turbulence conditions. Unlike LN channels, AMA-1 algorithm with the PPM scheme brings improvement over non-adaptive case. While the performance of AMA-2 is similar to AMA-1 algorithm for small power margins, it does not saturate at higher power values and can achieve at maximum $\log_2 (M_{PAM}^{\max})$ bits/sec/Hz unlike AMA-1 with a maximum value of 0.5 bits/sec/Hz. It can be concluded from comparisons of Fig. 31 and Fig. 32 that adaptive systems are particularly beneficial in strong turbulence conditions.

In conclusion of this Chapter, we have proposed variable-rate and variable-power MISO and SIMO FSO systems. The proposed three adaptive algorithms, namely AMA-1, AMA-2, AMPA, maximize the spectral efficiency under peak and average power constraints while maintaining a targeted value of outage probability. In AMA-1, the spectral efficiency is maximized by adaptively changing the PPM size. In AMA-2, both PPM and PAM are deployed, and modulation type/size is changed to maximize the spectral efficiency. In AMPA, in addition to modulation size/type, transmit power is further adapted to channel conditions. Numerical results demonstrate the superiority of proposed adaptive schemes over non-adaptive systems. It is also observed that AMA-2 based on the joint use of PPM and PAM

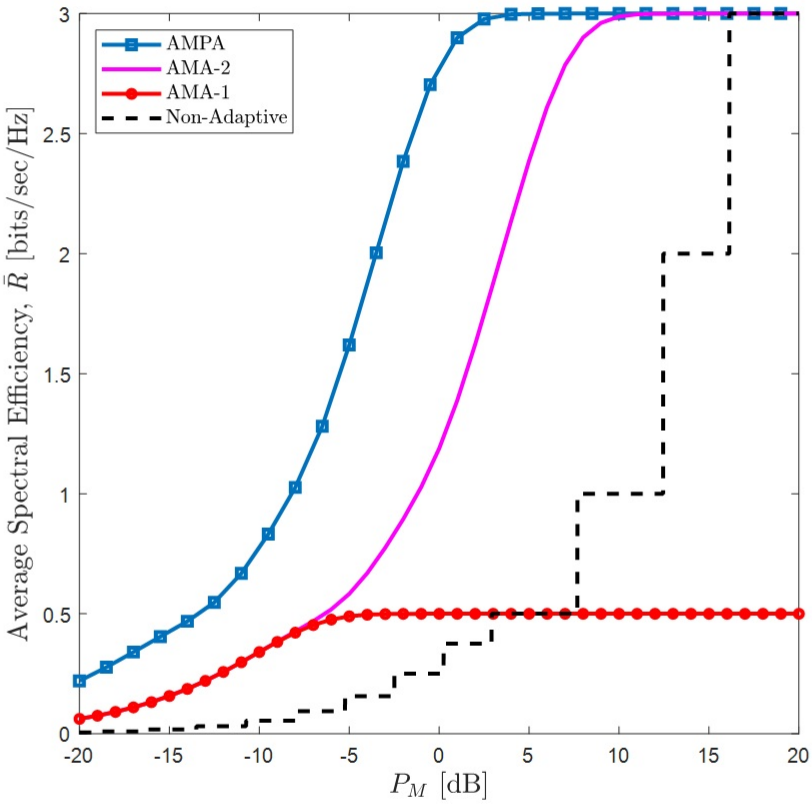

Figure 31: Average achievable spectral efficiencies over LN turbulence model for 1×4 SIMO case.

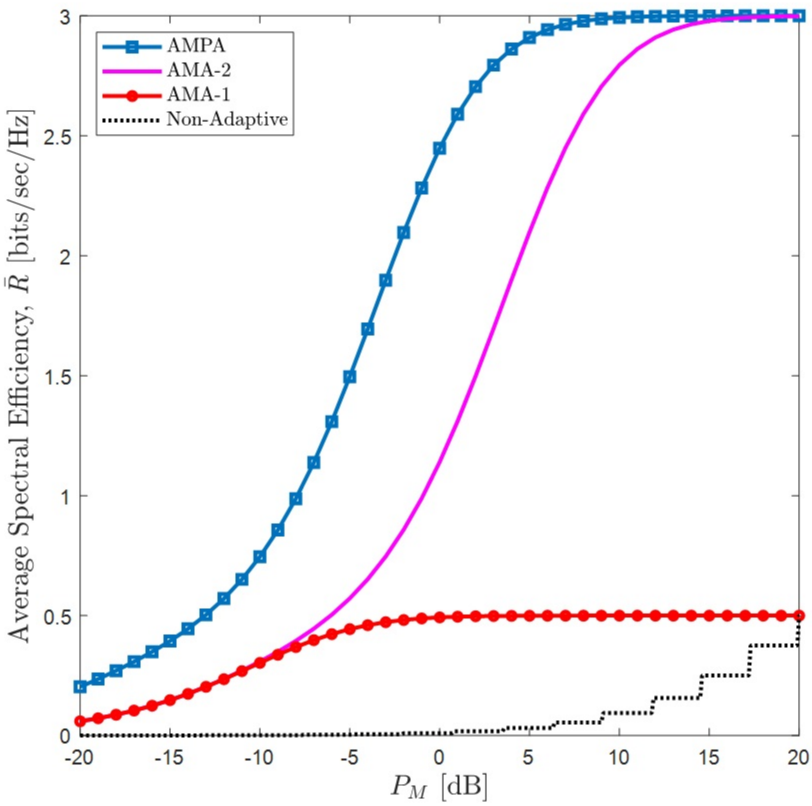

Figure 32: Average achievable spectral efficiencies over GG turbulence model for 1×4 SIMO case.

gives the flexibility to cover more transmission modes and achieves higher spectral efficiencies in comparison to AMA-1. AMPA provides further performance gains where instantaneous transmit power is adjusted according to the channel conditions. Numerical results of average achievable spectral efficiencies under different turbulence regimes demonstrate that the proposed adaptive systems are particularly beneficial in strong turbulence conditions.

CHAPTER VI

CONCLUSION

In this thesis, we have investigated the performance limitations of FSO communication systems and proposed models and methods to mitigate and overcome the system limitations. These limitations are mostly due to system losses, atmospheric conditions and turbulence induced fading. While we specify accurate models for the FSO channel, we proposed adaptive algorithms in combination to multiple aperture FSO systems to significantly mitigate the turbulence induced fading and improve it's performance via increasing the achievable data rate and limiting the outage.

In the first part of this research, we used our custom design atmospheric channel emulator for FSO system evaluations in a controlled environment and experimentally investigated the performance of FSO links. Specifically, we investigated the geometric loss, absorption loss, foggy weather conditions, different beam shapes, and atmospheric turbulence using the atmospheric chamber. The existing fog channel models were compared against the experimental results. Having observed that the existing models are not universal, a new refined model is proposed that provides a good match for 850, 1310, and 1550 nm wavelengths under consideration. Furthermore, we investigated the effect of wavelength on aperture averaging. We considered the three commonly used wavelengths of λ =850, 1310, and 1550 nm. Employing a custom-design atmospheric chamber, we estimated the PDF of atmospheric turbulence-induced fading channel coefficient for aperture sizes of D = 1, 3.6, and 8.7 mm under the same emulated conditions. At a fixed wavelength, the larger the aperture size is, the less it is affected by the turbulence. At the same aperture size, when we increase the wavelength, we have observed that 1310 and 1550 nm links are least affected by the turbulence and exhibit almost similar value of scintillation indices but significantly less than 850 nm. It has been also observed that the PDF tends to shift from GG toward LN distribution even for relatively small aperture sizes if the wavelength is sufficiently high. In summary, by increasing the aperture size and/or wavelength, the distribution shifts toward LN statistics.

Next, we have investigated Log-normal fading modek and the DMT over MIMO channels. We first have derived the asymptotical DMT for MIMO systems. Our results have shown that the asymptotical maximum diversity gain tends to infinity with $\ln(SNR)$. To have a fair comparison of gains between different cases, we have normalized the diversity gains with that of a benchmark (i.e., SISO case) and used the concept of relative asymptotical DMT. The relative asymptotical DMT curve is described by $MN(1-r)^2$ and a maximum diversity gain of MN can be obtained. Then, we have focused on finite-SNR DMT which does not yield a closed-form expression for the general MIMO case. As special cases, we have investigated MISO/SIMO systems and 2×2 MIMO system. Numerical results for MIMO systems show that at high SNR values, multiplexing gains are achievable at the price of very low diversity gains. This means that while designing coding schemes for MIMO systems over log-normal channel, one may decide to invest more on extracting diversity other than multiplexing.

Having a fundamental analysis of DMT, we proposed an adaptive MIMO FSO system where a judiciously designed switching mechanism chooses different operation modes, i.e., diversity, multiplexing or hybrid, based on channel conditions. We formulated the design of adaptive FSO system as a maximization problem of the outage capacity while satisfying a predefined target outage probability. We calculated the outage capacities for each operation mode and constructed the LUTs. In the proposed system, the received SNR is compared against the SNR thresholds available in the LUT and the optimal transmission mode is selected accordingly.

Our numerical results revealed that the proposed system has significant improvements over stand-alone diversity and multiplexing schemes and ensure an overall robust performance throughout the SNR range.

Furthermore, we have proposed variable-rate and variable-power MISO and SIMO FSO systems. The proposed three adaptive algorithms, namely AMA-1, AMA-2, AMPA, maximize the spectral efficiency under peak and average power constraints while maintaining a targeted value of outage probability. In AMA-1, the spectral efficiency is maximized by adaptively changing the PPM size. In AMA-2, both PPM and PAM are deployed, and modulation type/size is changed to maximize the spectral efficiency. In AMPA, in addition to modulation size/type, transmit power is further adapted to channel conditions. Numerical results demonstrate the superiority of proposed adaptive schemes over non-adaptive systems. It is also observed that AMA-2 based on the joint use of PPM and PAM gives the flexibility to cover more transmission modes and achieves higher spectral efficiencies in comparison to AMA-1. AMPA provides further performance gains where instantaneous transmit power is adjusted according to the channel conditions. Numerical results of average achievable spectral efficiencies under different turbulence regimes demonstrate that the proposed adaptive systems are particularly beneficial in strong turbulence conditions.

In conclusion, this work propose a promising progress to overcome the main impairments (fog attenuations and turbulence induced fading) of the FSO links in four ways: 1) by examining the channel and proposing novel models and characteristics for atmospheric attenuations trade-off 2) by taking advantage of aperture averaging and wavelength dependency 3) by investigating and proposing spatial adaptation in MIMO FSO links and 4) by employing adaptive modulation and power control scenarios and approving the promising performance of adaptive system.

CHAPTER VII

FUTURE WORK

Although the proposed channel models and adaptive schemes have demonstrated a promising performance improvement for FSO links and overcoming the impairments in both ways of increasing reliability and if possible the data rate of the system, the investigation cannot stop at this point and always there is room for improvement. In this direction, we discuss possible future works for continuation of the topic.

First of all, the DMT analysis in this thesis has been carried out under Log-normal fading channel. Log-normal fading channel accurately captures the characteristics of FSO channel model for weak turbulence regime. However, in strong turbulence regions different channel models such as Gamma-Gamma, α-μ, Nakagami-m fading models are introduced. A future work would be analyzing the DMT under these type of channel fading models.

Furthermore, the adaptive modulation and power control algorithm introduced in Chapter 5, is analyzed for MISO and SIMO system. Another future work would be analyzing and extending the performance of adaptive modulation and power proposed in chapter 5, in conjunction with spatial adaptation proposed in Chapter 4. Although the mathematical derivation would be difficult for such a work, but the derivations provided in this thesis can be a lead and insight to follow a complete adaptive scheme for MIMO FSO system with spatial adaptation in conjunction with adaptive modulation and power which gives a total flexibility to the system to completely adapt to severe channel conditions.

APPENDIX A

APPROXIMATING THE SUM OF LOG-NORMAL RANDOM VARIABLES

In this Appendix, we provide a summary of two methods used in approximating the sum of log-normal random variables with another log-normal random variable.

Fenton-Wilkinson method: This method [104] works based on matching the first and second central moments. The mean and variance of log-normal RV approximating the sum is found as the summation of the mean and variance of the RVs. In our case, we have

$$\exp(z) = \sum_{j=1}^{M} h_j^2 = \sum_{j=1}^{M} \exp(2\chi_j) \tag{146}$$

where $z \sim \mathcal{N}(\mu_z, \sigma_z^2)$. The first and second central moments are given by $E[exp(z)] = M \cdot E[\exp(2\chi_j)]$ and $\mathrm{Var}[\exp(z)] = M \cdot \mathrm{Var}[\exp(2\chi_j)]$ which yield

$$\exp\left(\mu_z + \sigma_z^2/2\right) = M \cdot \exp\left(2\mu_x + 2\sigma_x^2\right), \tag{147}$$

$$\begin{aligned} &\exp\left(2\mu_z + \sigma_z^2\right)\left(\exp\left(\sigma_z^2\right) - 1\right) \\ &= M \cdot \exp\left(4\mu_x + 4\sigma_x^2\right)\left(\exp\left(4\sigma_x^2\right) - 1\right). \end{aligned} \tag{148}$$

Solving the above two equations and applying $\mu_x = -\sigma_x^2$, we can find the mean and variance of z as

$$\sigma_z^2 = \ln\left(1 + \frac{e^{4\sigma_x^2} - 1}{M}\right), \tag{149}$$

$$\mu_z = \ln(M) - \frac{\sigma_z^2}{2}. \tag{150}$$

MGF-based approach: This method [105], works based on the MGF matching. According to the fact that the product of MGF of the RVs results in the total

MGF of the sum PDF, a closed-form expression for MGF of log-normal distribution would be required in MGF-based approach. Although a general expression is not available, the log-normal MGF can be obtained based on Gauss-Hermite integration [116] using a series expansion. The Gauss-Hermite representation of the log-normal MGF is defined as [105]

$$\hat{\Psi}(s;\mu,\sigma) \triangleq \sum_{n=1}^{K} \frac{w_n}{\sqrt{\pi}} \exp\left[-s\exp\left(\sqrt{2}\sigma a_n + \mu\right)\right] \tag{151}$$

where s is an adjustable parameter of MGF and K is the Hermite integration order. w_n and a_n in (151) represent respectively the weights and abscissas which are tabulated in [116, Tbl. 25.10] for K up to 20. Since MGF of the sum of i.i.d. RVs can be written as the product of the MGFs of individual RVs, in order to find μ_z and σ_z, we should solve the following system of two equations:

$$\hat{\Psi}_z(s_k;\mu_z,\sigma_z) = \prod_{j=1}^{M} \hat{\Psi}_{\chi_j}(s_k;\mu_{\chi_j},\sigma_{\chi_j}), \text{ for } k=1, k=2 \tag{152}$$

Replacing (151) in (152), the system of equations can be written as

$$\begin{aligned}&\sum_{n=1}^{K} \frac{w_n}{\sqrt{\pi}} \exp\left[-s_k\exp\left(\sqrt{2}\sigma_z a_n + \mu_z\right)\right]\\ &= \prod_{j=1}^{M}\sum_{n=1}^{K} \frac{w_n}{\sqrt{\pi}} \exp\left[-s_k\exp\left(\sqrt{2}\sigma_{\chi_j} a_n + \mu_{\chi_j}\right)\right] \ , k=1,2\end{aligned} \tag{153}$$

These non-linear equations can be readily solved numerically. Increasing the Hermite integration order K results in more accurate estimate of μ_z and σ_z. It has been found that $K = 12$ is sufficient to accurately determine the values of μ_z and σ_z [105]. Furthermore, optimizing s_1 and s_2 reduce the accuracy metric (mean absolute error) which is defined in the following. Let $F_{(s_1,s_2)}(.)$ and G denote respectively the log-normal CDF and the empirically observed CDF using Monte Carlo simulations. We consider n reference points as $p_1, ..., p_n$. The mean absolute error accuracy metric for CDF is defined by

$$M_{cdf} = \sum_{i=1}^{n} \frac{1}{n} \frac{\left|G(p_i) - F_{(s_1,s_2)}(p_i)\right|}{G(p_i)}. \tag{154}$$

APPENDIX B

OUTAGE PERFORMANCE CALCULATIONS

Based on [124], the channel capacity conditioned on $\mathbf{h}$ can be written as

$$C(\mathbf{h}) = \frac{1}{2}\log\left(1+\frac{\eta^2 L^2\sigma_x^2}{n_t^2\sigma_w^2}\left(\sum_{i=1}^{\kappa} h_i\right)^2\right) = \frac{1}{2}\log\left(1+\xi\bar{\rho}h_{eff}^2\right) \tag{155}$$

where $\zeta = 1$ for MISO and $\zeta = n_r^2$ for SIMO systems. The outage probability is then given by [124]

$$\begin{aligned} P_{out}(R,\bar{\rho}) &= \Pr\left\{\frac{1}{2}\log\left(1+\zeta\bar{\rho}h_{eff}^2\right) < R\right\} \\ &= \Pr\left\{h_{eff} < \left(\frac{2^{2R}-1}{\zeta\bar{\rho}}\right)^{1/2}\right\} = F_{h_{eff}}\left(\left(\frac{2^{2R}-1}{\zeta\bar{\rho}}\right)^{1/2}\right) \end{aligned} \tag{156}$$

where $F_{h_{eff}}(\cdot)$ is the CDF of h_{eff}.

LN distribution: h_{eff} in (156) is the sum of i.i.d. log-normal random variables (RVs) which can be well approximated as a single log-normal RV [125], i.e., $h_{eff} = e^u$ with variance of $\sigma_u^2 = \ln\left(1+\left(e^{\sigma_{\ln h}^2}-1\right)/\kappa\right)$ and mean $\mu_u = -\sigma_u^2/2$. Therefore, we can write (156) as

$$\begin{aligned} P_{out}(R,\bar{\rho}) &\cong \Pr\left\{u < \frac{1}{2}\ln\left(\frac{2^{2R}-1}{\bar{\rho}}\right)\right\} \\ &= Q\left(\frac{1}{2\sigma_u}\ln\left(\frac{\zeta\bar{\rho}}{2^{2R}-1}\right) - \frac{\sigma_u}{2}\right) \end{aligned} \tag{157}$$

GG distribution: We write the outage probability expression in (156) in term of the sum of i.i.d. Gamma-Gamma RVs as

$$P_{out}(R,\bar{\rho}) = \Pr\left\{\sum_{i=1}^{\kappa} h_i < \kappa\left(\frac{2^{2R}-1}{\zeta\bar{\rho}}\right)^{1/2}\right\} \tag{158}$$

While no exact distribution is available for the sum of GG random variables, we follow the methodology in [126], [127] to approximate $\Omega = \sum_{i=1}^{\kappa} h_i$ with $\alpha-\mu$ distribution. The corresponding CDF is given by [128] $F_\Omega(\omega) = \Gamma(\nu, \nu\omega^\tau/\hat{\omega}^\tau)/\Gamma(\nu)$ where $\Gamma(z,x) = \int_0^x e^{-t}t^{z-1}dt$ is the lower incomplete Gamma function, ν and τ are two positive parameters and $\hat{\omega} = \left(E\left[\omega^{\tau}\right]\right)^{1/\tau}$ is a scale parameter. Using moment-based parameter estimators [128] (Eqs. 5,15,16), we can find values of unknown parameters ν, τ and $\hat{\omega}$. Specifically, we need to solve the following system of equations:

$$\frac{\Gamma^2\left(\nu + 1/\tau\right)}{\Gamma\left(\nu\right)\Gamma\left(\nu + 2/\tau\right) - \Gamma^2\left(\nu + 1/\tau\right)} = \frac{E^2\left[\Omega\right]}{E\left[\Omega^2\right] - E^2\left[\Omega\right]} \tag{159}$$

$$\frac{\Gamma^2\left(\nu + 2/\tau\right)}{\Gamma\left(\nu\right)\Gamma\left(\nu + 4/\tau\right) - \Gamma^2\left(\nu + 2/\tau\right)} = \frac{E^2\left[\Omega^2\right]}{E\left[\Omega^4\right] - E^2\left[\Omega^2\right]} \tag{160}$$

$$\hat{\omega} = \frac{\nu^{1/\tau}\Gamma\left(\nu\right)E\left[\Omega\right]}{\Gamma\left(\nu + 1/\tau\right)} \tag{161}$$

For the solution of above system of equations, the first, the second, and the fourth moments of Ω are required. Note that the mean of Ω is simply obtained as $E\left[\Omega\right] = \kappa$. In general, by using multinomial expansion theorem, the j^{th} moment of Ω can be computed by

$$\begin{aligned} E\left[\Omega^j\right] = &\sum_{n_1=0}^{j}\sum_{n_2=0}^{n_1}\cdots\sum_{n_{\kappa-1}=0}^{n_{\kappa-2}} \\ &\binom{j}{n_1}\binom{n_1}{n_2}\cdots\binom{n_{\kappa-2}}{n_{\kappa-1}} E\left[h_1^{j-n_1}\right]E\left[h_2^{n_1-n_2}\right]\cdots E\left[h_\kappa^{n_{\kappa-1}}\right] \end{aligned} \tag{162}$$

In (162), the j^{th} moment of h_i can be obtained using [129] (Eq. 6.561–16) as:

$$E\left[h_i^j\right] = \frac{\Gamma\left(\alpha + j\right)\Gamma\left(\beta + j\right)}{\left(\alpha\beta\right)^j\Gamma\left(\alpha\right)\Gamma\left(\beta\right)} \tag{163}$$

Eventually, the outage probability of (158) can be written using the CDF of Ω as

$$P_{out}\left(R,\bar{\rho}\right) = F_{\Omega}\left(\kappa\left(\frac{2^{2R}-1}{\zeta\bar{\rho}}\right)^{1/2}\right) = \frac{\Gamma\left(\nu, \nu\kappa\left(\frac{2^{2R}-1}{\zeta\bar{\rho}}\right)^{\tau/2}/\hat{\omega}^{\tau}\right)}{\Gamma\left(\nu\right)} \tag{164}$$

Note that the outage probability expression of (164) is not applicable to the SISO case (i.e., $n_t = 1$, $n_r = 1$). For the SISO case, instead, the direct derivation should be made. For this purpose, the CDF of h can be derived with the aid of [130] (Eq. 26) as:

$$F_h\left(h\right) = \frac{\left(\alpha\beta h\right)^{\frac{\alpha+\beta}{2}}}{\Gamma\left(\alpha\right)\Gamma\left(\beta\right)} G_{1,3}^{2,1}\left[\alpha\beta h \,\middle|\, \begin{matrix} 1 - \frac{\alpha+\beta}{2} \\ \frac{\alpha-\beta}{2}, \frac{\beta-\alpha}{2}, -\frac{\alpha+\beta}{2} \end{matrix}\right] \tag{165}$$

where $G_{p,q}^{m,n}[x|\begin{smallmatrix} a_1, ..., a_p \\ b_1, ..., b_q \end{smallmatrix}]$ is Meijer's G-function [130] (Eq. 9.301). Using (165), the outage probability of SISO FSO link can be written in closed-form as

$$\begin{aligned} P_{out}\left(R, \bar{\rho}\right) = & \frac{1}{\Gamma\left(\alpha\right)\Gamma\left(\beta\right)}\left(\alpha\beta\left(\frac{2^{2R}-1}{\bar{\rho}}\right)^{1/2}\right)^{\frac{\alpha+\beta}{2}} \times \\ & G_{1,3}^{2,1}\left[\alpha\beta\left(\frac{2^{2R}-1}{\bar{\rho}}\right)^{1/2}\middle|\begin{matrix} 1-\frac{\alpha+\beta}{2} \\ \frac{\alpha-\beta}{2}, \frac{\beta-\alpha}{2}, -\frac{\alpha+\beta}{2} \end{matrix}\right] \end{aligned} \tag{166}$$

APPENDIX C

CALCULATION OF M_{PPM}^{MAX}

AMA-1/AMA-2: $M_{PPM}^{\max}$ dictates the maximum modulation size that can be selected, and outage occurs for the case of $P_r\left(h_{eff}\right) \;\; P_{log_2\left(M_{PPM}^{\max}\right)}$. Mathematically speaking, we have

$$\begin{aligned} P_{out}\left(R\left(h_{eff}\right),\bar{\rho}\right) &= \Pr\left\{P_r\left(h_{eff}\right) \;\; P_{log_2\left(M_{PPM}^{\max}\right)}\right\} \\ &= \Pr\left\{h_{eff} < \left(\frac{\left[M_{PPM}^{\max}\right]^{2/M_{PPM}^{\max}}-1}{\zeta\bar{\rho}}\right)^{1/2}\right\} \end{aligned} \tag{167}$$

Using (157) for LN distribution we have

$$Q\left(\frac{1}{2\sigma_u}\ln\left(\frac{\zeta\bar{\rho}}{\left[M_{PPM}^{\max}\right]^{2/M_{PPM}^{\max}}-1}\right)-\frac{\sigma_u}{2}\right)<\varepsilon \tag{168}$$

On the other hand, using (164) for GG distribution we have

$$\Gamma\left(\nu,\nu\kappa\left(\frac{\left[M_{PPM}^{\max}\right]^{2/M_{PPM}^{\max}}-1}{\zeta\bar{\rho}}\right)^{\tau/2}/\hat{\omega}^{\tau}\right)/\Gamma\left(\nu\right)<\varepsilon \tag{169}$$

AMPA: In case of AMPA, the outage occurs when $h_{eff} < th_{M_{PPM}^{\max}}$ and this can be expressed as

$$\begin{aligned} P_{out}\left(R\left(h_{eff}\right),\bar{\rho}\right) &= \Pr\left\{h_{eff} < th_{M_{PPM}^{\max}}\right\} \\ &= \Pr\left\{h_{eff} < \frac{\sigma_w}{\sqrt{\zeta}P_{pt,\max}\eta L}\left[\frac{\left(\left[M_{PPM}^{\max}\right]^{2/M_{PPM}^{\max}}-1\right)}{\left(M_{PPM}^{\max}-1\right)}\right]^{1/2}\right\} \end{aligned} \tag{170}$$

Using (157) for LN distribution, we obtain

$$Q\left(\frac{1}{2\sigma_u}\ln\left(\frac{\sqrt{\zeta}P_{pt,\max}^2\eta^2L^2\left(M_{PPM}^{\max}-1\right)}{\sigma_w^2\left(\left[M_{PPM}^{\max}\right]^{\frac{2}{M_{PPM}^{\max}}}-1\right)}\right)-\frac{\sigma_u}{2}\right)<\varepsilon \tag{171}$$

On the other hand, using (164) for GG distribution, we obtain

$$\Gamma\left(\nu,\frac{\nu\kappa\sigma_w}{\sqrt{\zeta}P_{pt,\max}\eta L}\left[\frac{\left(\left[M_{PPM}^{\max}\right]^{\frac{2}{M_{PPM}^{\max}}}-1\right)}{\left(M_{PPM}^{\max}-1\right)}\right]^{\frac{\tau}{2}}/\hat{\omega}^{\tau}\right)/\Gamma\left(\nu\right)<\varepsilon \tag{172}$$

APPENDIX D

CALCULATION OF P_{OT}

It can be noted from (127) and (128) that the calculation of P_{ot} requires the channel statistics of h_{eff}. In the following, we present the derivations for both LN and GG distributions.

LN distribution: In this case, $h_{eff} = (1/\kappa)\sum_{i=1}^{\kappa} h_i$, $\kappa \in \{n_t, n_r\}$ (c.f. Section 5.2) is the sum of i.i.d. LN RVs which can be well approximated as a single log-normal RV, i.e., $h_{eff} = e^u$ with mean μ_u and variance of σ_u^2. For weak turbulence conditions ($\sigma_x < 4$ dB), we can safely use Fenton-Wilkinson's approach [125]. The variance and mean of h_{eff} can be found as $\sigma_u^2 = \ln\left(1 + \left(e^{\sigma^2_{\ln h}} - 1\right)/n_t\right)$ and $\mu_u = -\sigma_u^2/2$. Using LN approximation for h_{eff} and replacing it in (127) and applying change of variable $u = \ln(h_{eff})$, we can simplify it as

$$\begin{aligned}
P_{ot}^{PPM}(M) &= P_{pt,\max} th_M^{PPM} \int_{th_M^{PPM}}^{th_{M/2}^{PPM}} \frac{e^{-u}}{\sqrt{2\pi\sigma_u^2}} \exp\left(\frac{-(u-\mu_u)^2}{2\sigma_u^2}\right) du \\
&= P_{pt,\max} th_M^{PPM} e^{\sigma_u^2} \int_{th_M^{PPM}}^{th_{M/2}^{PPM}} \frac{1}{\sqrt{2\pi\sigma_u^2}} \exp\left(\frac{-(u+1.5\sigma_u^2)^2}{2\sigma_u^2}\right) du \\
&= P_{pt,\max} th_M^{PPM} e^{\sigma_u^2} \times \\
&\quad \left[Q\left(\frac{\ln\left(th_M^{PPM}\right) + 1.5\sigma_u^2}{\sigma_u}\right) - Q\left(\frac{\ln\left(th_{M/2}^{PPM}\right) + 1.5\sigma_u^2}{\sigma_u}\right)\right]
\end{aligned} \tag{173}$$

where $M \leq M_{PPM}^{\max}$. For PAM scheme, $P_{ot}^{PAM}(M)$ can be derived in a similar manner and it is given by

$$\begin{aligned}
P_{ot}^{PAM}(M) &= \frac{P_{pt,\max} th_M^{PAM}}{2} \exp\left(\sigma_u^2\right) \times \\
&\left[Q\left(\frac{\ln\left(th_M^{PAM}\right) + 1.5\sigma_u^2}{\sigma_u}\right) - Q\left(\frac{\ln\left(th_{2M}^{PAM}\right) + 1.5\sigma_u^2}{\sigma_u}\right)\right]
\end{aligned} \tag{174}$$

where $M \leq M_{PAM}^{\max}$. We consider $th^{PPM}_{M^{\max}_{PPM}} = 0$ and $th^{PAM}_{2M^{\max}_{PAM}} \to \infty$ to cover the whole integral region in (127). It can be easily seen that the switching threshold between PPM and PAM schemes is equal to th_2^{PAM}. Therefore, we consider $th_1^{PPM} = th_2^{PAM}$ for continuity of the integral region. Then, we can write the average power of the system based on (126) as

$$\begin{aligned} P_{ot} = &\sum_{M=M_{PPM}^{\max}}^{2} P_{pt,\max} th_M^{PPM} \exp\left(\sigma_u^2\right) \times \\ &\left[Q\left(\frac{\ln\left(th_M^{PPM}\right) + 1.5\sigma_u^2}{\sigma_u}\right) - Q\left(\frac{\ln\left(th_{M/2}^{PPM}\right) + 1.5\sigma_u^2}{\sigma_u}\right)\right] \\ &+ \sum_{M=2}^{M_{PAM}^{\max}} \frac{P_{pt,\max} th_M^{PAM}}{2} \exp\left(\sigma_u^2\right) \times \\ &\left[Q\left(\frac{\ln\left(th_M^{PAM}\right) + 1.5\sigma_u^2}{\sigma_u}\right) - Q\left(\frac{\ln\left(th_{2M}^{PAM}\right) + 1.5\sigma_u^2}{\sigma_u}\right)\right] \end{aligned} \quad (175)$$

which should satisfy $P_{ot} \leq P_{ot,\max}$.

GG distribution: In this case, $h_{eff} = (1/\kappa)\sum_{i=1}^{\kappa} h_i$, $\kappa \in \{n_t, n_r\}$ (c.f. Section 5.2) is the sum of i.i.d. GG RVs. Based on (126), the integrals of P_{ot} can be written as

$$\begin{aligned} P_{ot} = &\sum_{M=M_{PPM}^{\max}}^{2} \left[P_{pt,\max} th_M^{PPM} \int_{th_M^{PPM}}^{th_{M/2}^{PPM}} \frac{1}{h_{eff}} f_{h_{eff}}\left(h_{eff}\right) dh_{eff} \right] \\ &+ \sum_{M=2}^{M_{PAM}^{\max}} \left[\frac{P_{pt,\max} th_M^{PAM}}{2} \int_{th_{M/2}^{PAM}}^{th_M^{PAM}} \frac{1}{h_{eff}} f_{h_{eff}}\left(h_{eff}\right) dh_{eff} \right] \leq P_{ot,\max} \end{aligned} \quad (176)$$

Unfortunately, there is no closed form expression for (176). However, these integrals can be efficiently calculated through numerical methods.

REFERENCES

[1] M. A. Khalighi and M. Uysal, "Survey on free space optical communication: A communication theory perspective," *IEEE Communications Surveys & Tutorials*, vol. 16, no. 4, pp. 2231–2258, 2014.

[2] H. Kaushal and G. Kaddoum, "Optical communication in space: challenges and mitigation techniques," *IEEE Communications Surveys & Tutorials*, vol. 19, no. 1, pp. 57–96, 2016.

[3] M. Uysal *et al.*, *Optical wireless communications: an emerging technology.* Springer, 2016.

[4] L. C. Andrews and R. L. Phillips, *Laser beam propagation through random media.* SPIE, 2005.

[5] N. A. M. Nor, Z. Ghassemlooy, S. Zvanovec, and M.-A. Khalighi, "Performance analysis of all-optical amplify-and-forward fso relaying over atmospheric turbulence," in *IEEE Student Conference on Research and Development (SCOReD)*, pp. 289–293, IEEE, 2015.

[6] P. Chvojka, J. Bohata, J. Libich, S. Zvanovec, and J. Perez, "Laboratory and outdoor availability and spatial coherence tests of wireless optical links," in *2nd International Workshop on Optical Wireless Communications (IWOW)*, pp. 109–112, IEEE, 2013.

[7] J. Perez, Z. Ghassemlooy, S. Rajbhandari, M. Ijaz, and H. Le Minh, "Ethernet fso communications link performance study under a controlled fog environment," *IEEE Communications Letters*, vol. 16, no. 3, pp. 408–410, 2012.

[8] M. A. Esmail, H. Fathallah, and M.-S. Alouini, "An experimental study of fso link performance in desert environment," *IEEE Communications Letters*, vol. 20, no. 9, pp. 1888–1891, 2016.

[9] J. Libich *et al.*, "Combined effect of turbulence and aerosol on free-space optical links," *Applied optics*, vol. 56, no. 2, pp. 336–341, 2017.

[10] M. Ijaz, Z. Ghassemlooy, H. Le Minh, S. Rajbhandari, J. Perez, and A. Gholami, "Bit error rate measurement of free space optical communication links under laboratory-controlled fog conditions," in *16th European Conference on Networks and Optical Communications*, pp. 52–55, IEEE, 2011.

[11] M. Ijaz *et al.*, "Analysis of fog and smoke attenuation in a free space optical communication link under controlled laboratory conditions," in *International Workshop on Optical Wireless Communications (IWOW)*, pp. 1–3, IEEE, 2012.

[12] M. Ijaz *et al.*, "Modeling of fog and smoke attenuation in free space optical communications link under controlled laboratory conditions," *Journal of Lightwave Technology*, vol. 31, no. 11, pp. 1720–1726, 2013.

[13] J. H. Churnside, "Aperture averaging of optical scintillations in the turbulent atmosphere," *Applied Optics*, vol. 30, no. 15, pp. 1982–1994, 1991.

[14] H. Yuksel, C. C. Davis, and L. Wasiczko, "Aperture averaging experiment for optimizing receiver design and analyzing turbulence on free space optical communication links," in *Conference on Lasers and Electro-Optics*, pp. 743–745, Optical Society of America, 2005.

[15] R. Barrios, F. Dios, J. Recolons, and A. Rodriguez, "Aperture averaging in a laser gaussian beam: simulations and experiments," in *Free-Space Laser Communications X*, vol. 7814, p. 78140C, International Society for Optics and Photonics, 2010.

[16] N. Mehta, H. Kaushal, V. Jain, and S. Kar, "Experimental study on aperture averaging in free space optical communication link," in *National Conference on Communications (NCC)*, pp. 1–3, IEEE, 2013.

[17] F. S. Vetelino *et al.*, "Characterizing the propagation path in moderate to strong optical turbulence," *Applied Optics*, vol. 45, no. 15, pp. 3534–3543, 2006.

[18] F. S. Vetelino, C. Young, L. Andrews, and J. Recolons, "Aperture averaging effects on the probability density of irradiance fluctuations in moderate-to-strong turbulence," *Applied Optics*, vol. 46, no. 11, pp. 2099–2108, 2007.

[19] D. T. Wayne *et al.*, "Comparing the log-normal and gamma-gamma model to experimental probability density functions of aperture averaging data," in *Free-Space Laser Communications X*, vol. 7814, p. 78140K, International Society for Optics and Photonics, 2010.

[20] V. Tarokh, N. Seshadri, and A. R. Calderbank, "Space-time codes for high data rate wireless communication: performance analysis and code construction," *IEEE Trans. Inf. Theory*, vol. 44, pp. 744–765, Mar. 1998.

[21] S. M. Alamouti, "A simple transmit diversity technique for wireless communications," *IEEE J. Sel. Areas Commun.*, vol. 16, pp. 1451–1458, Oct. 1998.

[22] V. Tarokh, H. J. Jafarkhani, and A. R. Calderbank, "Space-time block codes from orthogonal designs," *IEEE Trans. Inf. Theory*, vol. 45, pp. 1456–1467, July 1999.

[23] L. Zheng and D. N. C. Tse, "Diversity and multiplexing: A fundamental tradeoff in multuple-antenna channels," *IEEE Trans. Inf. Theory*, vol. 49, pp. 1073–1096, May 2003.

[24] R. Narasimhan, "Finite-snr diversity-multiplexing tradeoff for correlated rayleigh and rician mimo channels," *IEEE Trans. Inf. Theory*, vol. 52, pp. 3965–3979, Sept. 2006.

[25] D. Tse, P. Viswanath, and L. Zheng, “Diversity-multiplexing tradeoff in multiple-access channels,” *IEEE Trans. Inf. Theory*, vol. 50, pp. 1859–1874, Sept. 2004.

[26] T. Kim and M. Skoglund, “Diversity-multiplexing tradeoff in mimo channels with partial csit,” *IEEE Trans. Inf. Theory*, vol. 53, pp. 2743–2759, Aug. 2007.

[27] M. Yuksel and E. Erkip, “Multiple-antenna cooperative wireless systems: A diversity-multiplexing tradeoff perspective,” *IEEE Trans. Inf. Theory*, vol. 53, pp. 3371–3393, Oct. 2007.

[28] E. Stauffer *et al.*, “Finite-snr diversity-multiplexing tradeoffs in fading relay channels,” *IEEE J. Sel. Areas Commun.*, vol. 25, pp. 245–257, Feb. 2007.

[29] L. Zhao, W. Mo, Y. Ma, and Z. Wang, “Diversity and multiplexing tradeoff in general fading channels,” *IEEE Trans. Inf. Theory*, vol. 53, pp. 1549–1557, Apr. 2007.

[30] W. Y. Shin, S. Y. Chung, and Y. H. Lee, “Diversity-multiplexing tradeoff and outage performance for rician mimo channels,” *IEEE Trans. Inf. Theory*, vol. 54, pp. 1186–1196, Mar. 2008.

[31] L. Grokop and D. Tse, “Diversity-multiplexing tradeoff in isi channels,” *IEEE Trans. Inf. Theory*, vol. 55, pp. 109–135, Jan. 2009.

[32] D. Gunduz, M. Khojastepour, A. Goldsmith, and H. Poor, “Multi-hop mimo relay networks: diversity-multiplexing trade-off analysis,” *IEEE Trans. Wireless Commun.*, vol. 9, pp. 1738–1747, May 2010.

[33] A. E. Falou *et al.*, “Finite-snr diversity-multiplexing tradeoff for rayleigh mimo channels,” *IEEE Commun. Lett.*, vol. 17, pp. 753–756, April 2013.

[34] F. Lotse, J. E. Berg, and R. Bownds, “Indoor propagation measurement at 900 mhz,” in *in Proc. IEEE Veh. Technol. Conf.*, (Denver, CO), pp. 629–632, May 1992.

[35] H. Hashemi, “The indoor radio propagation channel,” *Proc. IEEE*, vol. 81, pp. 943–967, July 1993.

[36] S. Y. Seidel, K. Takamizawa, and T. S. Rappaport, “Application of second-order statistics for an indoor radio channel model,” in *in Proc. IEEE Veh. Technol. Conf.*, (San Fransisco, CA), pp. 888–892, May 1989.

[37] X. Zhu and J. M. Kahn, “Free-space optical communication through atmospheric turbulence channels,” *IEEE Trans. Commun.*, vol. 50, pp. 1293–1300, Aug. 2002.

[38] E. Lee and V. Chan, “Part 1: optical communication over the clear turbulent atmospheric channel using diversity,” *IEEE J. Sel. Areas Commun.*, vol. 22, no. 9, pp. 1896–1906, 2004.

[39] S. M. Navidpour, M. Uysal, and M. Kavehrad, "Ber performance of free-space optical transmission with spatial diversity," *IEEE Trans. Wireless Commun.*, vol. 6, pp. 2813–2819, Aug. 2007.

[40] F. Heliot, X. Chu, R. Hoshyar, and R. Tafazolli, "A tight closed-form approximation of the log-normal fading channel capacity," *IEEE Trans. Wireless Commun.*, vol. 8, pp. 2842–2847, June 2009.

[41] A. Laourine, A. Stephenne, and S. Affes, "Estimating the ergodic capacity of log-normal channels," *IEEE Commun. Lett.*, vol. 11, pp. 568–570, July 2007.

[42] A. Laourine, A. Stephenne, and S. Affes, "On the capacity of log-normal fading channels," *IEEE Trans. Commun.*, vol. 57, pp. 1603–1607, June 2009.

[43] D. Skraparlis, V. Sakarellos, A. Panagopoulos, and J. Kanellopoulos, "New results on the statistics and the capacity of dual-branch mrc and egc diversity in correlated lognormal channels," *IEEE Commun. Lett.*, vol. 15, pp. 617–619, June 2011.

[44] G. Pan, E. Ekici, and Q. Feng, "Capacity analysis of log-normal channels under various adaptive transmission schemes," *IEEE Commun. Lett.*, vol. 16, pp. 346–348, Mar. 2012.

[45] D. Skraparlis, M. Sandell, V. Sakarellos, A. Panagopoulos, and J. Kanellopoulos, "On the effect of correlation on the performance of dual diversity receivers in lognormal fading," *IEEE Commun. Lett.*, vol. 14, pp. 1038–1040, Nov. 2010.

[46] C. Abou-Rjeily and M. Bkassiny, "On the achievable diversity orders over non-severely faded lognormal channels," *IEEE Commun. Lett.*, vol. 14, pp. 695–697, Aug. 2010.

[47] M. S. Alouini and M. K. Simon, "Dual diversity over correlated lognormal fading channels," *IEEE Trans. Commun.*, vol. 50, pp. 1946–1959, Dec. 2002.

[48] T. Piboongungon and V. A. Aalo, "Outage probability of l-branch selection combining in correlated lognormal fading channels," *Electron. Lett.*, vol. 40, p. 263, July 2004.

[49] M. Safari and M. Uysal, "Cooperative diversity over log-normal fading channels: performance analysis and optimization," *IEEE Trans. Wireless Commun.*, vol. 7, pp. 1963–1972, May 2008.

[50] M. Renzo, F. Graziosi, and F. Santucci, "A comprehensive framework for performance analysis of cooperative multi-hop wireless systems over log-normal fading channels," *IEEE Trans. Commun.*, vol. 58, pp. 531–544, Feb. 2010.

[51] G. Pan, E. Ekici, and Q. Feng, "Performance analysis of multi-branch multi-hop wireless relay systems over log-normal channels," *IEEE Trans. Wireless Commun.*, vol. 13, pp. 223–233, Jan. 2014.

[52] B. K. Levitt, "Variable rate optical communication through the turbulent atmosphere," *Technical Report 483, Massachusetts Institute of Technology, Research Laboratory of Electronics*, Aug 1971.

[53] J. Li and M. Uysal, "Achievable information rate for outdoor free space optical communication with intensity modulation and direct detection," in *Proc. IEEE Global Commun. Conf.*, pp. 827–831, Nov. 2003.

[54] M. Gubergrits, R. Goot, U. Mahlab, and S. Arnon, "Adaptive power control for satellite to ground laser communication," *Int. J. Satellite Commun. Netw.*, vol. 25, pp. 323–348, Aug. 2007.

[55] J. A. Anguita, M. A. Neifeld, B. Hildner, and B. Vasic, "Rateless coding on experimental temporally correlated fso channels," *IEEE J. Lightw. Technol.*, vol. 28, pp. 990–1002, APr. 2010.

[56] I. B. Djordjevic, "Adaptive modulation and coding for free-space optical channels," *IEEE/OSA J. Optical Commun. Netw.*, vol. 2, pp. 221– 229, May 2010.

[57] O. Barsimantov and N. N. Nikulin, "Adaptive optimization of a free space laser communication system under dynamic link attenuation," *IEEE/OSA J. Optical Commun. Netw.*, vol. 3, pp. 219–222, Mar. 2011.

[58] M. Karimi and M. Uysal, "Novel adaptive transmission algorithms for free-space optical links," *IEEE Trans. Commun.*, vol. 60, pp. 3808–3815, Dec. 2012.

[59] W. G. Cowley, K. D. Nguyen, and D. Giggenbach, "Adaptive symbol-rate free-space-optical communications," in *Australian Communications Theory Workshop (AusCTW)*, (Adelaide, SA), pp. 122–127, 2013.

[60] M. S. Salah, W. G. Cowley, and K. D. Nguyen, "Adaptive transmission schemes for free-space optical channel," in *8th International Conference on Signal Processing and Communication Systems (ICSPCS)*, (Gold Coast, QLD), pp. 1–7, 2014.

[61] L. Liu, M. Safari, and S. Hranilovic, "Rate-adaptive fso communication via rate-compatible punctured ldpc codes," in *IEEE International Conference on Communications (ICC)*, (Budapest), pp. 3948–3952, 2013.

[62] N. B. Hassan and M. D. Matinfar, "On the implemetation aspects of adaptive power control algorithms in free-space optical communications," in *Iran Workshop on Communication and Information Theory (IWCIT)*, (Tehran), pp. 1–5, 2014.

[63] V. V. Mai and A. T. Pham, "Cross-layer designs and analysis of adaptive-rate transmission and arq for free-space optical communications," *IEEE Photonics Journal*, vol. 8, pp. 1–15, Feb. 2016.

[64] H. Nouri and M. Uysal, "Adaptive free space optical communication system with multiple apertures," in *24th Signal Processing and Communication Application Conference (SIU)*, (Zonguldak), pp. 937–940, 2016.

[65] N. D. Chatzidiamantis, A. S. Lioumpas, G. K. Karagiannidis, and S. Arnon, "Adaptive subcarrier psk intensity modulation in free space optical systems," *IEEE Trans. Commun.*, vol. 59, pp. 1368–1377, May 2011.

[66] I. Z. Hassan, M. J. Hossain, and J. Cheng, "Performance of mimo adaptive subcarrier qam intensity modulation in gamma-gamma turbulence," in *13th Canadian Workshop on Information Theory*, (Toronto, ON), pp. 195–199, 2013.

[67] A. Garg, M. R. Bhatnagar, O. Berder, and B. Vrigneau, "Imperfect-quantized-feedback-based beamforming for an fso miso system over gamma-gamma fading with pointing errors," *IEEE/OSA Journal of Optical Communications and Networking*, vol. 9, pp. 1005–1018, Nov. 2017.

[68] M. R. Bhatnagar, "A one bit feedback based beamforming scheme for fso miso system over gamma-gamma fading," *IEEE Trans. Commun.*, vol. 63, pp. 1306–1318, Apr. 2015.

[69] R. W. Heath, Jr., and A. Paulraj, "Switching between spatial multiplexing and transmit diversity based on constellation distance," *IEEE Trans. Commun.*, vol. 53, pp. 962–968, June 2005.

[70] C. B. Chae *et al.*, "Adaptive spatial modulation for mimo-ofdm," in *Proc. IEEE WCNC*, vol. 1, pp. 87–92, Mar. 2004.

[71] M. R. McKay *et al.*, "Multiplexing/beamforming switching for coded-mimo in spatially correlated rayleigh channels," *IEEE Trans. Vehic. Tech.*, vol. 56, pp. 2555–67, Sept. 2007.

[72] C. B. Chae *et al.*, "Adaptive mimo transmission techniques for broadband wireless communication systems [topics in wireless communications]," *IEEE Communications Magazine*, vol. 48, pp. 112–118, May 2010.

[73] L. Andrews and R. Phillips, *Laser Beam Propagation through Random Media, 2nd edition.* SPIE Press, 2005.

[74] E. J. Lee and V. W. S. Chan, "Part 1: optical communication over the clear turbulent atmospheric channel using diversity," *IEEE Journal on Selected Areas in Communications*, vol. 22, pp. 1896–1906, Nov. 2004.

[75] A. Goldsmith, *Wireless communications.* Cambridge university press, 2005.

[76] A. J. Goldsmith and P. P. Varaiya, "Capacity of fading channels with channel side information," *IEEE Transactions on Information Theory*, vol. 43, no. 6, pp. 1986–1992, 1997.

[77] G. Caire, G. Taricco, and E. Biglieri, "Optimum power control over fading channels," *IEEE Transactions on Information Theory*, vol. 45, no. 5, pp. 1468–1489, 1999.

[78] G. Caire and K. R. Kumar, "Information theoretic foundations of adaptive coded modulation," *Proceedings of the IEEE*, vol. 95, no. 12, pp. 2274–2298, 2007.

[79] B. K. Levitt, "Variable-rate optical communication through the turbulent atmosphere," *Technical Report 483*, 1971.

[80] J. A. Anguita, M. A. Neifeld, B. Hildner, and B. Vasic, "Rateless coding on experimental temporally correlated fso channels," *Journal of Lightwave Technology*, vol. 28, no. 7, pp. 990–1002, 2010.

[81] I. B. Djordjevic, "Adaptive modulation and coding for free-space optical channels," *Journal of Optical Communications and Networking*, vol. 2, no. 5, pp. 221–229, 2010.

[82] O. Barsimantov and V. V. Nikulin, "Adaptive optimization of a free space laser communication system under dynamic link attenuation," *Journal of Optical Communications and networking*, vol. 3, no. 3, pp. 215–222, 2011.

[83] M. Karimi and M. Uysal, "Novel adaptive transmission algorithms for free-space optical links," *IEEE Transactions on Communications*, vol. 60, no. 12, pp. 3808–3815, 2012.

[84] W. G. Cowley, K. D. Nguyen, and D. Giggenbach, "Adaptive symbol-rate free-space-optical communications," in *Australian Communications Theory Workshop (AusCTW)*, pp. 122–127, IEEE, 2013.

[85] M. S. Salah, W. G. Cowley, and K. D. Nguyen, "Adaptive transmission schemes for free-space optical channel," in *8th International Conference on Signal Processing and Communication Systems (ICSPCS)*, pp. 1–7, IEEE, 2014.

[86] L. Liu, M. Safari, and S. Hranilovic, "Rate-adaptive fso communication via rate-compatible punctured ldpc codes," in *IEEE International Conference on Communications (ICC)*, pp. 3948–3952, IEEE, 2013.

[87] V. V. Mai and A. T. Pham, "Cross-layer designs and analysis of adaptive-rate transmission and arq for free-space optical communications," *IEEE Photonics Journal*, vol. 8, no. 1, pp. 1–15, 2016.

[88] N. D. Chatzidiamantis, A. S. Lioumpas, G. K. Karagiannidis, and S. Arnon, "Adaptive subcarrier psk intensity modulation in free space optical systems," *IEEE Transactions on Communications*, vol. 59, no. 5, pp. 1368–1377, 2011.

[89] I. Z. Hassan, M. J. Hossain, and J. Cheng, "Performance of mimo adaptive subcarrier qam intensity modulation in gamma-gamma turbulence," in *13th Canadian Workshop on Information Theory*, pp. 195–199, IEEE, 2013.

[90] H. Nouri and M. Uysal, "Adaptive mimo fso communication systems with spatial mode switching," *Journal of Optical Communications and Networking*, vol. 10, no. 8, pp. 686–694, 2018.

[91] M. A. Khalighi and M. Uysal, "Survey on free space optical communication: A communication theory perspective," *IEEE Communications Surveys & Tutorials*, vol. 16, no. 4, pp. 2231–2258, 2014.

[92] X. Zhu and J. M. Kahn, "Free-space optical communication through atmospheric turbulence channels," *IEEE Transactions on communications*, vol. 50, no. 8, pp. 1293–1300, 2002.

[93] E. Biglieri, J. Proakis, and S. Shamai, "Fading channels: Information-theoretic and communications aspects," *IEEE Transactions on Information Theory*, vol. 44, no. 6, pp. 2619–2692, 1998.

[94] J. Perez *et al.*, "Ethernet fso communications link performance study under a controlled fog environment," *IEEE Communications Letters*, vol. 16, no. 3, pp. 408–410, 2012.

[95] M. Ijaz *et al.*, "Modeling of fog and smoke attenuation in free space optical communications link under controlled laboratory conditions," *Journal of Lightwave Technology*, vol. 31, no. 11, pp. 1720–1726, 2013.

[96] H. Willebrand and B. S. Ghuman, *Free space optics: enabling optical connectivity in today's networks.* SAMS publishing, 2002.

[97] A. Parent, M. Morin, and P. Lavigne, "Propagation of super-gaussian field distributions," *Optical and Quantum Electronics*, vol. 24, no. 9, pp. S1071–S1079, 1992.

[98] P. W. Kruse, L. D. McGlauchlin, and R. B. McQuistan, "Elements of infrared technology: Generation, transmission and detection," *New York: Wiley*, 1962.

[99] I. I. Kim, B. McArthur, and E. J. Korevaar, "Comparison of laser beam propagation at 785 nm and 1550 nm in fog and haze for optical wireless communications," in *Optical Wireless Communications III*, vol. 4214, pp. 26–37, International Society for Optics and Photonics, 2001.

[100] A. Papoulis, *Probability, Random Variables, and Stochastic Processes.* New York: McGraw-Hill, 1991.

[101] D. Tse and P. Viswanath, *Fundamentals of wireless communication.* Cambridge university press, 2005.

[102] S. Haddad and O. Leveque, "Diversity analysis of free-space optical networks with multihop transmissions," in *in IEEE International Conference on Communications (ICC)*, pp. 3406–3411, 10-14 June 2014.

[103] C. Abou-Rjeily, "Performance analysis of uwb systems over the ieee 802.15.3a channel model," *IEEE Trans. Commun.*, vol. 59, pp. 2377–2382, Sept. 2011.

[104] L. Fenton, "The sum of log-normal probability distributions in scatter transmission systems," *IRE Transactions on Communications Systems*, vol. 8, pp. 57–67, Mar. 1960.

[105] N. Mehta, J. Wu, A. Molisch, and J. Zhang, "Approximating a sum of random variables with a lognormal," *IEEE Trans. Wireless Commun.*, vol. 6, pp. 2690–2699, July 2007.

[106] M. Safari and M. Uysal, "Do we really need ostbcs for free-space optical communication with direct detection?," *IEEE Trans. Wireless Commun.*, vol. 7, pp. 4445–4448, Nov. 2008.

[107] H. Willebrand and B. S. Ghuman, *Free Space Optics: Enabling Optical Connectivity in Today's Networks.* Sams Publishing, 2002.

[108] I. Kim, J. Koontz, *et al.*, "Measurement of scintillation and link margin for the terra link laser communication system," in *in Proc. SPIE*, vol. 3232, pp. 100–118, Jan. 1998.

[109] D. Tse and P. Viswanath, *Fundamentals of wireless communication.* Cambridge university press, 2005.

[110] H. Willebrand and B. S. Ghuman, *Free space optics: enabling optical connectivity in today's networks.* SAMS publishing, 2002.

[111] I. I. Kim *et al.*, "Measurement of scintillation and link margin for the terralink laser communication system," in *Wireless Technologies and Systems: Millimeter-Wave and Optical*, vol. 3232, pp. 100–118, International Society for Optics and Photonics, 1998.

[112] B. Kebapci, F. Miramirkhani, H. Nouri, and M. Uysal, "A custom-design atmospheric channel emulator for the performance evaluation of free space optical communication systems," in *19th International Conference on Transparent Optical Networks (ICTON)*, pp. 1–5, IEEE, 2017.

[113] L. C. Andrews and R. L. Phillips, *Laser beam propagation through random media.* SPIE, 2005.

[114] M. Safari and M. Uysal, "Do we really need ostbcs for free-space optical communication with direct detection?," *IEEE Transactions on Wireless Communications*, vol. 7, no. 11, pp. 4445–4448, 2008.

[115] "http://www.fsona.com/product.php?sec=1250ep."

[116] M. Abramowitz and I. A. Stegun, *Handbook of Mathematical Functions: with Formulas, Graphs, and Mathematical Tables.* Dover Publications, 1965.

[117] M. Uysal, C. Capsoni, Z. Ghassemlooy, A. Boucouvalas, and E. Udvary, *Optical wireless communications: an emerging technology.* Springer, 2016.

[118] M. A. Khalighi and M. Uysal, "Survey on free space optical communication: A communication theory perspective," *IEEE Communications Surveys and Tutorials*, vol. 16, no. 4, pp. 2231–2258, 2014.

[119] H. Kaushal and G. Kaddoum, "Optical communication in space: Challenges and mitigation techniques," *IEEE Communications Surveys and Tutorials*, vol. 19, no. 1, pp. 57–96, 2017.

[120] B. Kebapci, F. Miramirkhani, H. Nouri, and M. Uysal, "A custom-design atmospheric channel emulator for the performance evaluation of free space optical communication systems," in *19th International Conference on Transparent Optical Networks (ICTON)*, (Girona, Spain), pp. 1–5, 2017.

[121] L. B. Stotts, *Free Space Optical Systems Engineering: Design and Analysis.* John Wiley & Sons, 2017.

[122] H. Kaushal and G. Kaddoum, "Optical communication in space: challenges and mitigation techniques," *IEEE Communications Surveys & Tutorials*, vol. 19, no. 1, pp. 57–96, 2016.

[123] H. Nouri and M. Uysal, "Adaptive free space optical communication system with multiple apertures," in *24th Signal Processing and Communication Application Conference (SIU)*, pp. 937–940, May 2016.

[124] D. Tse and P. Viswanath, *Fundamentals of wireless communication.* Cambridge university press, 2005.

[125] L. Fenton, "The sum of log-normal probability distributions in scatter transmission systems," *IRE Transactions on Communications Systems*, vol. 8, no. 1, pp. 57–67, 1960.

[126] K. P. Peppas, "A simple, accurate approximation to the sum of gamma–gamma variates and applications in mimo free-space optical systems," *IEEE Photonics Technology Letters*, vol. 23, no. 13, pp. 839–841, 2011.

[127] G. Yang, M.-A. Khalighi, S. Bourennane, and Z. Ghassemlooy, "Approximation to the sum of two correlated gamma-gamma variates and its applications in free-space optical communications," *IEEE Wireless Communications Letters*, vol. 1, no. 6, pp. 621–624, 2012.

[128] M. D. Yacoub, "The α-μ distribution: A physical fading model for the stacy distribution," *IEEE Transactions on Vehicular Technology*, vol. 56, no. 1, pp. 27–34, 2007.

[129] I. Gradshteyn, "Im ryzhik table of integrals," *Series, and Products, Alan Jeffrey and Daniel Zwillinger (eds.), Seventh edition*, vol. 885, 2007.

[130] V. Adamchik and O. Marichev, "The algorithm for calculating integrals of hypergeometric type functions and its realization in reduce system," in *Proceedings of the International Symposium on Symbolic and Algebraic Computation*, pp. 212–224, 1990.

VITA

Hatef Nouri received the B.Sc. (Hons.) degree in Electrical and Electronic Engineering from the University of Tehran, Tehran, Iran, in 2010, and the M.Sc. degree in Electrical and Electronic Engineering from Ozyegin University, Istanbul, Turkey, where he is currently pursuing his Ph.D. degree in Electrical and Electronic Engineering. He has been a teaching and research assistant with the Communication Theory and Technologies Research Group since 2010. He is specializing in telecommunications with a focus on the physical layer aspects of wireless communication. His research interests include information theory, cooperative communications, optical wireless communications, and underwater acoustic wireless communications. During his M.Sc., he studied the information theoretical performance analysis of underwater acoustic communication systems. He has served as a Reviewer of the IEEE Vehicular Technology Conference in 2012, the IEEE Globecom 2013, the IEEE JOURNAL ON SELECTED AREAS IN COMMUNICATIONS of the 2014 Special Issue on Optical Wireless Communication, the IEEE COMMUNICATIONS LETTERS in 2016, the IEEE BlackSeaCom 2017, the IEEE International Symposium on Information Theory (ISIT) 2017, the IEEE Transactions on Information theory in 2017, the IEEE Transactions on Communications 2017-2020, and the IEEE Transactions on Wireless Communications 2017-2020. His distinctions include the rank of 178th among 400 000 students in Iran's nationwide university entrance exam in 2006, the Faculty of Engineering Scholarship as an Exceptional Student from 2006 to 2010, and the Full Entrance Scholarship for the M.Sc. and Ph.D. degrees at Ozyegin University.